Spin-dependent scattering in CPP-GMR using Heusler alloy and the selection of the spacer material

Nakatani Tomoya
(Doctoral Program in Materials Science and Engineering)

Submitted to the Graduate School of
Pure and Applied Sciences
in Partial Fulfillment of the Requirements
for the Degree of Doctor of Philosophy in Engineering

at the
University of Tsukuba

Table of contents

Chapter 1 Background **1**
1.1 Preface: Demand of data storage with low energy consumption 1
1.2 Giant magnetoresistance (GMR) effect Giant 2
1.2.1 Brief history of GMR 2
1.2.2 Spin-dependent scattering in ferromagnetic materials 4
1.2.3 Current-in-plane giant magnetoresistance (CIP-GMR) 5
1.2.4 Current-perpendicular-to-plane giant magnetoresistance (CPP-GMR) 7
1.3 Applications of CPP-GMR 9
1.3.1 Read head for ultrahigh density magnetic recording 9
1.3.2 Spin torque oscillators for microwave generation 11
1.4 Co-based Heusler alloy 15
1.4.1 General introduction of half-metal 15
1.4.2 Crystal structure of full Heusler alloy 16
1.4.3 Thermodynamic property 17
1.4.4 Electronic structure 19
1.4.5 Application to tunnel magnetoresistance (TMR) devices 23
1.5 Current status of the CPP-GMR research 24
1.5.1 Current-confine-path nano-oxide layer (CCP-NOL) spacer 24
1.5.2 Development of ferromagnetic materials 26
1.6 Purpose of the study 29
1.7 Outline of this thesis 30
References 31

Chapter 2 Theory of CPP-GMR **37**
2.1 Spin accumulation at F/N junctions 37
2.2 Valet-Fert model 41
2.2.1 Parallel resister model without spin relaxation 41
2.2.2 General solution of diffusion equation 43
References 48

Chapter 3 Experimental description **49**
3.1 Choice of the Heusler alloy 49

3.2 Fabrication of thin films 51
3.2.1 Sputtering machine and the deposition conditions 51
3.2.2 Underlayer for CPP-GMR devices 52
3.3 Microfabrication 54
3.4 Characterization of films 56
3.5 Transport measurements 57
3.5.1 Electrical resistivity and Hall measurements 57
3.5.2 MR measurement 59
References 60

Chapter 4 Fabrication of CPP-GMR spin-valves with $Co_2(FeA_{0.5}Si_{0.5})$ and Ag 61

4.1 Introduction 61
4.2 Fabrication of Cr/Ag underlayer 62
4.3 Fabrication of CAFS film 65
4.3.1 Crystal structure 65
4.3.2 Magnetic property 69
4.3.3 Electric resistivity 71
4.3.4 Hall effect 72
4.4 Interlayer coupling in CFAS/Ag/CFAS trilayer 74
4.4.1 Sample structure and magnetization measurement 74
4.4.2 Magnetization behavior 74
4.5 Exchange biased spin-valves 78
4.5.1 Layer and device structures 78
4.5.2 Magnetization behavior 78
4.5.3 CPP–GMR property 79
4.6 Pseudo spin-valves 80
4.6.1 Necessity of pseudo spin-valves 80
4.6.2 Layer and device structures 81
4.6.3 TEM observation 81
4.6.4 Microfabrication: measurement of the pillar size 82
4.6.5 CPP–GMR property 83
4.6.6 Dependence of ΔRA on the annealing temperature 88
4.7 Effect of sense current density 91
4.7.1 Exchange biased spin-valves 92

4.7.2 Pseudo spin-valves 95
4.8 Summary of this chapter 96
References 98

Chapter 5 Analysis of spin asymmetries of CPP-GMR with CFAS/Ag/CFAS trilayer 99
5.1 Introduction 99
5.2 Experimental data: variation of ΔRA on the CFAS layer thickness 100
5.3 Estimation of the CFAS/Ag interfacial resistance 103
5.4 Analysis of the spin-dependent scattering 106
5.4.1 Valet-Fert model 106
5.4.2 Newly developed Taniguchi-Imamura model 109
5.5 Effect of the insertion of CAFS(1 nm) layers at CoFe/Ag interfaces 111
5.5.1 Sample structure 111
5.5.2 CPP-GMR property 112
5.6 Relationship between the spin asymmetries and the degree of B2 order 113
5.7 Discussion 116
5.6.1 Origin of the large interfacial scattering at the CFAS/Ag and its temperature dependence 116
5.6.2 Spin-flipping at the CFAS/Ag interface 118
5.8 Summary of this chapter 122
References 124

Chapter 6 CPP-GMR with NiAl spacer layer 127
6.1 Introduction 127
6.2 Choice of NiAl B2 intermetallic compound 129
6.3 Fabrication of the exchange biased spin-valve 131
6.3.1 Sputtering deposition of NiAl film 131
6.3.2 Layer structure of the spin-valve 132
6.3.3 Structural characterizations 132
6.3.4 Magnetization behavior 135
6.3.5 CPP-GMR property 137
6.4 Discussion 140
6.4.1 Band matching at the CAFS/NiAl interface 140
6.4.2 A way to obtain a larger CPP-GMR with the NiAl spacer layer 140

6.5 Summary of this chapter 141
References 142

Chapter 7 Summary 143

Appendix: Perspective of CPP-GMR research 147
Publications 150
Acknowledgements 152

Chapter 1 Background

1.1 Preface: Demand of data storage with low energy consumption

The amount of digital information in the world is increasing every year, has reached 2.8×10^{20} Bytes in 2007 (corresponding to 45 GBytes per a person) and will grow to 1.8×10^{21} Bytes in 2011 [1]. This corresponds to a growth rate of 50% every year. Along with the increase of information, the energy consumption for the data storage has become a big issue. For instance, the total power consumed by data centers in Japan was 5.7 billion kWh in 2007 [2], which corresponds to 650 MW and it is expected to keep growing by 13% every year. The power consumption by data centers in the United States was 7000 MW!! Note that the electric generation power of the world biggest atomic reactor is 1356 MW. Hard disk drive (HDD) is considered to be only the solution to store the huge digital information. Unless the recording density of HDD continues growing, the energy consumption for data storage will increase exponentially. Therefore, the development of the magnetic recording technology has a significant social demand.

A relatively new magnetics called Spintronics is one of the key technologies to achieve higher magnetic recording density. Current-perpendicular-to-plane giant magnetoresistance (CPP-GMR) is considered to be the next generation read head device of HDD, however, the improvement of the MR output by developing the materials is indispensable for the realization of the read heads. This doctoral thesis describes our study on the spin dependent scattering characteristics of Heusler alloy based CPP-GMR devices.

1.2 Giant magnetoresistance (GMR) effect

1.2.1 Brief history of GMR

Giant magnetoresistance (GMR) was discovered in 1988 by the group led by Albert Fert in France [3]. They fabricated a couple of epitaxial Fe/Cr multilayers and measured the resistance of the multilayers under magnetic field and the magnetization curves. As shown in Fig. 1-1, under a zero external magnetic field, the magnetization direction of the Fe layer is opposite to that of the adjacent Fe layer due to the antiferromagnetic interlayer exchange coupling (IEC) through the Cr spacer layer which was first observed in 1986 by Peter Grünberg *et al.* in Germany [4]. When external magnetic field is applied to the multilayer, the magnetization directions of the Fe layers started to rotate to parallel direction with increasing field, finally the total magnetic moment is saturated. Along with the magnetization rotation from antiparallel to parallel, a large change of the in-plane resistance of the multilayer was observed, which originated from the different electron scattering rate between the antiparallel and parallel magnetization states which is called *spin-dependent transport*. The magnetoresistance ratio (MR ratio) in the Fe/Cr multilayer reached 45% at 4.2 K and 17% at RT, where MR ratio is defined as $(R_{AP}–R_P)/R_P \times 100$ (R_{AP} and R_P are for the resistances for the anti- and parallel magnetizations.). This GMR effect is called current-in-plane (CIP) GMR to distinguish from the other GMR devices with different current flow geometry called CPP-GMR.

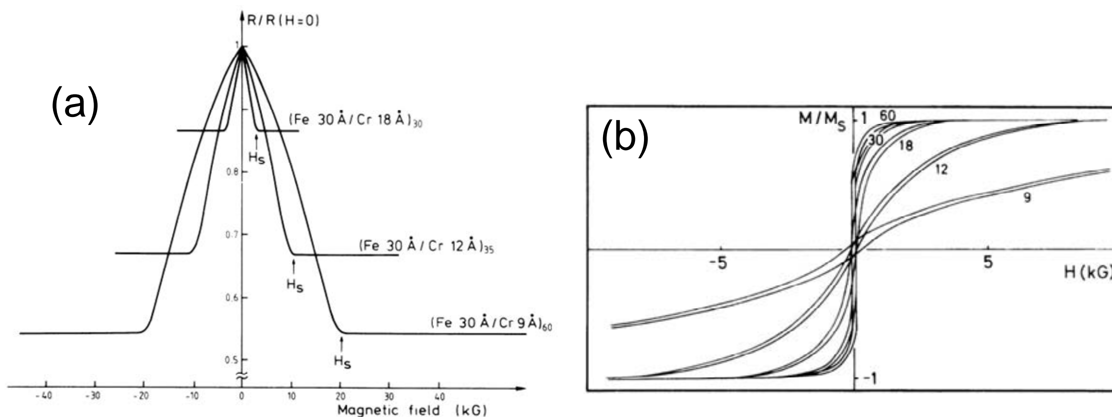

Fig. 1-1 The discovery of giant magnetoresistance. (a) In-plane resistance of Fe/Cr multilayers under external filed and (b) corresponding magnetization curves by Baibichi *et al.* [3].

The spin dependent scattering had been known from much older days. In 1930s Mott recognized the two current nature of ferromagnet, where the up and down spin electrons have different resistivities [5]. In 60s and 70s, Campbell and Fert intensively studied the two current transport in 3*d* metals and the effects by impurities [6]. However, the discovery of GMR in 1988 has been regarded as the start of spintronics because it has stimulated a lot works on the physics and materials of GMR and other spin-dependent phenomena. Another important point of GMR was that the application for magnetic sensing had been considered from the very early stage.

From the application point of view, the GMR in interlayer exchange coupled ferromagnet (F)/nonmagnet (N) systems has a big obstacle, because we need a large magnetic field to decouple the antiferromagnetic coupling in order to obtain the resistance change, while we want to sense a small magnetic flux from small recording bits. Fortunately, the necessary condition to obtain GMR is not the presence of the interlayer exchange coupling, but an antiparallel magnetization state between two or more F layers. In 1991, Dieny *et al.* (IBM) invented *spin-valve* composed of AF/F/N/F layers, where AF is an antiferromagnetic layer. The magnetization and the MR curves of their spin-valve are shown in Fig. 1-2 [7]. The magnetization of the one F layer (pinned layer) is fixed to one direction by the exchange magnetic anisotropy of the adjacent AF layer (pinning layer). The spacer layer N is sufficiently thick to weaken the coupling so that the magnetization of the other F layer (free layer) can follow the external field freely. Using the spin-valve composed of FeMn/NiFe/Cu/NiFe, they obtained the GMR output at ~ 10 Oe external fields, which is much smaller than that for the coupled F/N systems. Read heads using GMR were commercialized by Toshiba and IBM [8] independently for a recording density of 3 Gb/in^2. The GMR heads enabled us to obtain a much higher reading resolution, thus accelerated the evolution of the magnetic recording density by cooperating with the evolutions of the recoding medium and the other technologies. Fert and Grünberg were awarded the 2007 Nobel Prize in Physics for discovery of GMR and its contribution to the development of the magnetic recording technology.

Afterward, the GMR read head was replaced by tunneling magnetoresistance (TMR) devices with AlO and later MgO tunneling barriers showing higher MR outputs. The recording density of 500 Gb/in^2 has been commercialized at present [9]. Recently, GMR devices are attracting research interest again. In these devices, the current direction is perpendicular to the film plane, thereby called current-perpendicular-to-plane giant magnetoresistance (CPP-GMR). Owing to the low

device resistance and the higher MR output than CIP-GMR, CPP-GMR read heads are considered to feasible for ultrahigh density magnetic recording over 1 Tbit/in^2.

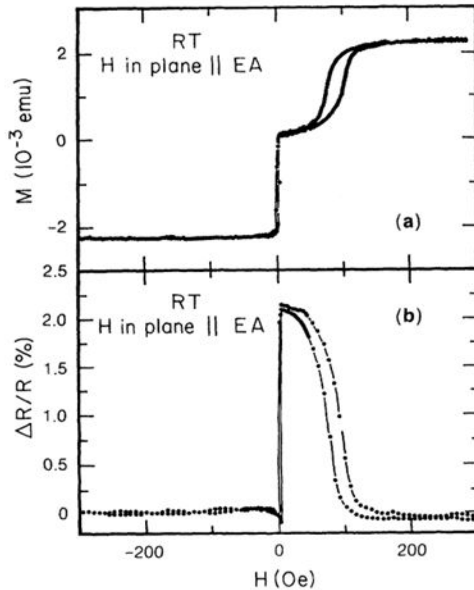

Fig. 1-2 Exchange biased spin-valve. (a) Magnetization curve of the exchange-biased spin-valves with a layer structure of FeMn/NiFe/Cu/NiFe, and (b) corresponding MR curve by Dieny et al. [7].

1.2.2 Spin-dependent scattering in ferromagnetic materials

For instance, the density of state of nickel is schematically shown in Fig. 1-3. The 3*d* band splits due to the exchange interaction, by which the electronic characters near the Fermi energy (E_F) are significantly different between the majority (up) and minority (down) spin electrons. The majority spin band near E_F is mainly composed of the *s* electrons, while the minority spin band has a large quantity of the *d* electron. According to Mott and Jones [5], the electric current is largely carried by the *s* electrons with a small effective mass, but the origin of the resistance is mainly the scattering from the *s* states to the *d* states. This is because the transition probability from one state to other state is generally proportional to the density of the final state. Thus, the resistance in transition metals is governed by the scattering from *s* to *d* with a large density of states than that from *s* to *s*. Therefore, the minority spin electron in Ni has a lager resistivity than that of the majority electron. The degree of the spin polarization of the current is defined by $\beta = (\rho_\downarrow - \rho_\uparrow)/(\rho_\uparrow + \rho_\downarrow)$, where $\rho_\uparrow$ and $\rho_\downarrow$ are the resistivities of the up and down spin electrons. This quantity is also called "bulk scattering spin asymmetry". The value of β of Ni has been reported to be $\beta = 0.14$ [10]. It should be also noted that the spin polarization defined by the total density of states is negative for Ni, whereas β is positive due to the mechanism of the spin-dependent scattering mentioned above.

In addition, Mott and Jones has pointed out that the electronic transport in ferromagnetic materials can be treated by a parallel resistance circuit composed of the up and spin channels as schematically shown in Fig. 1-4, called *two current model*. The two current model has been applied to explain the spin-dependent scattering by dilute impurities in ferromagnets by Campbell and Fert [6], and CPP-GMR by Valet and Fert [11].

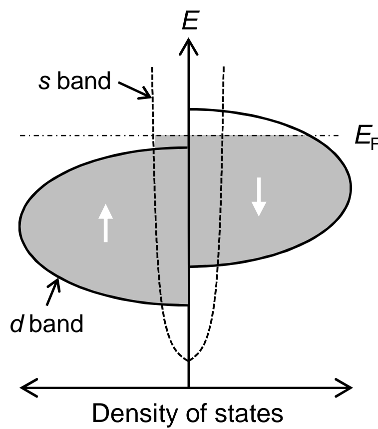

Fig. 1-3 Schematic density of state of Ni.

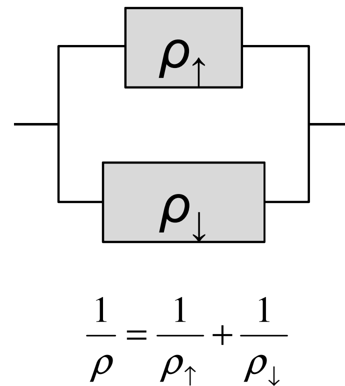

$$\frac{1}{\rho} = \frac{1}{\rho_\uparrow} + \frac{1}{\rho_\downarrow}$$

Fig. 1-4 Two current model for electric conduction in ferromagnetic materials composed of up and down spin channels

1.2.3 Current-in-plane giant magnetoresistance (CIP-GMR)

As mentioned in the previous subsection, electrons in ferromagnetic materials have difference scattering rates dependent on the spin direction, thus different resistivities $\rho_\uparrow$ and $\rho_\downarrow$. Here, assuming that there is not spin mixing between the up and down spins in the F/N multilayer, the total resistivity of the F/N multilayer in the parallel magnetization state ρ_P is, $\rho_P = (1/\rho_\uparrow+1/\rho_\downarrow)^{-1} = (\rho_\uparrow\ \rho_\downarrow)/(\rho_\uparrow+\rho_\downarrow)$. In the antiparallel magnetization state, electrons with one spin direction (up or down) are scattered as the majority and minority electrons alternately in the multilayer. Thus the resistivity of each spin channel is averaged to $\rho = (\rho_\uparrow+\rho_\downarrow)/2$, thus the total resistivity of the multilayer in the antiparallel state is $\rho_{AP} = (\rho_\uparrow+\rho_\downarrow)/4$. Therefore, the multilayer shows different resistances between the P and AP states. This is called current-in-plane giant magnetoresistance (CIP-GMR). The magnetoresistance ratio is defined by

$$\frac{\Delta\rho}{\rho_P} = \frac{(\rho_\uparrow - \rho_\downarrow)}{4\rho_\uparrow\rho_\downarrow} \tag{1.1}$$

in the optimistic definition or by

$$\frac{\Delta\rho}{\rho_{AP}} = \left(\frac{\rho_\uparrow - \rho_\downarrow}{\rho_\uparrow + \rho_\downarrow}\right)^2 = \left(\frac{\alpha - 1}{\alpha + 1}\right)^2 \quad \text{with} \quad \alpha = \frac{\rho_\downarrow}{\rho_\uparrow} \tag{1.2}$$

in the pessimistic definition. The above description is valid not only for the electron scattering in the bulk of the ferromagnetic layer but also for that at the interface between the ferromagnetic and nonmagnetic layers.

In fact, the origin of CIP-GMR is believed to be mainly the spin-dependent scattering at the F/N interface rather than that in the bulk of the F layers. The most striking experimental evidence was reported by Parkin [12]. He fabricated spin-valves with NiFe/Cu/NiFe and Co/Cu/Co sandwiches and studied the effect of insertions of very thin Co or NiFe layers at the NiFe/Cu or Co/Cu interfaces, respectively. Figure 1-5 shows a dramatic enhancement of GMR in NiFe/Cu/NiFe by the insertion of 2.5 Å Co layers at the interface. As shown in Fig. 1-6(a) the enhancement of GMR is saturated for the Co insertion of ~10 Å. On the other hand, Co insertions within the NiFe layers does not enhance GMR, but just degraded it. Similarly, thin NiFe layers were inserted at the Co/Cu inserfaces, resulting in a degradation of GMR. These results clearly indicate that the bulk scatterings of the NiFe layers and of the inserted Co layer do not contribute to GMR, and that the enhancement of GMR is due to the larger interfacial scattering at Co/Cu than that at NiFe/Cu.

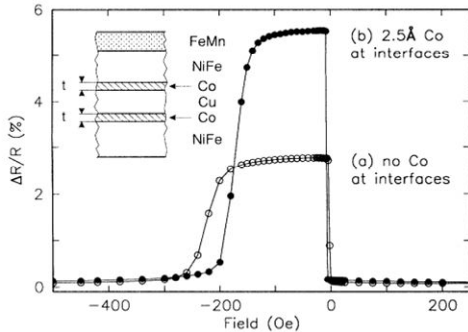

Fig. 1-5 Enhancement of CIP-GMR by inserting thin Co layer at the NiFe/Cu interfaces by Parkin [12] .

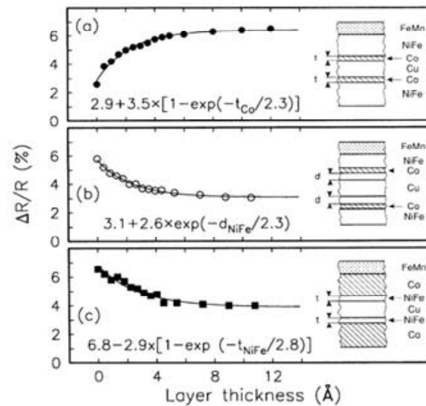

Fig. 1-6 Variations of CIP-GMR ratio as functions of thicknesses of layers of (a) Co inserted at NiFe/Cu interfaces, (b) NiFe between Co insertion and Cu spacer, and (c) Fe inserted at Co/Cu interface by Parkin [12].

1.2.4 Current-perpendicular-to-plane giant magnetoresistance (CPP-GMR)

The origin of CPP-GMR is the "spin accumulation" at the F/N interface. Since there is a spin-asymmetry of the electric resistivity in F, the current density carried by up spin electrons is more than that by down spin electrons ($j_{\uparrow}>j_{\downarrow}$) in a positively spin-polarized F ($\rho_{\uparrow}<\rho_{\downarrow}$). On the other hand, in N materials, $j_{\uparrow}=j_{\downarrow}$. Assuming that there is no spin-filp at the F/N interface, the current carried by both up and down spins has to be continued over the interface. This causes a deviation of the electronic chemical potential near the interface, this is called spin accumulation. The spin accumulation creates a voltage drop at the F/N interface dependent on the magnetization configuration of the F/N multilayer or the F/N/F trilayer, thus the resistance change can be observed between the parallel (P) and antiparallel (AP) magnetization state.

The CPP-GMR is briefly understood by a simple resistance model based on the two current model. Roughly, the product of the resistance change and the area of the current path ΔRA for the F/N/F trilayer is given by

$$\Delta RA \sim 2\frac{\beta^2}{1-\beta^2}\rho_{\mathrm{F}} + 2\frac{\gamma^2}{1-\gamma^2}AR_{\mathrm{F/N}} \qquad (1.3)$$

, where β and γ are the spin asymmetries of scattering in bulk and at interface defined by

$$\beta = \frac{\rho_{\downarrow}-\rho_{\uparrow}}{\rho_{\uparrow}+\rho_{\downarrow}}, \qquad (1.4)$$

$$\gamma = \frac{AR_{F/N\downarrow}-AR_{F/N\uparrow}}{AR_{F/N\uparrow}+AR_{F/N\downarrow}}, \qquad (1.5)$$

where ρ_{F} and $AR_{\mathrm{F/N}}$ are the resistivity of the ferromagnet and interfacial resistance-area product, respectively. This form ΔRA is similar to that of the TMR ratio (Julliere's equation). Due to the denominators of $1-\beta^2$ and $1-\gamma^2$, ΔRA can be infinite when the value of β or γ is 1. Therefore, materials with high spin polarization are expected to be effective to obtain large CPP-GMR values.

The biggest advantage of CPP-GMR is that the output of CPP-GMR is intrinsically larger than that of CIP-GMR. This may be understood as follows. In the CIP geometry, the current flows mainly in the spacer layer due to the lower resistivity than that of the magnetic layer. One the other hand, in the CPP geometry, the current flows in whole the layered films, thus the spin-dependent scattering can be utilized more efficiently. For example, if we assume the situation that the F layers are half-metals, there should be no conduction in AP magnetization state for the CPP geometry, therefore the MR ratio is infinity. One the other hand, in CIP geometry there is still finite conduction in AP state, because the current can flow in the space layer and in the F layers whose magnetization

is parallel to the up spin direction (the quantization axis). The larger MR ratio in CPP geometry than in CIP geometry has been demonstrated experimentally for Co/Ag multilayer by Pratt, Jr. *et al*. [13] and for Fe/Cr multilayer by Gijs *et al*. [14].

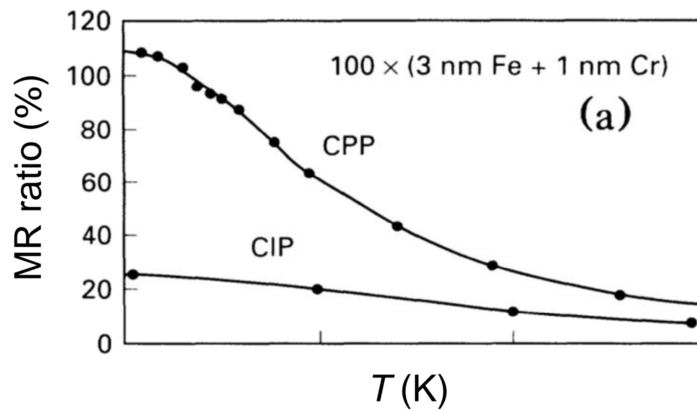

Fig. 1-7 GMR ratios in Fe/Cr multilayer at various temperatures in CIP and CPP geometries reported by Gijs *et al.* [14].

1.3 Applications of CPP-GMR

1.3.1 Read head for ultrahigh density magnetic recording

In hard dick drives (HHDs), the information is recorded as magnetization of recording bit on magnetic medium, which is composed of particles of a hard magnetic material (currently, CoCrPt alloy) surrounded and magnetically isolated by nonmagnetic matrix, called a granular structure. Reading the magnetization direction of the recording bits is carried out by a read head flying on the recording medium. Figure 1-8 briefly explains the principle of the reading by spin-valve read heads. The currently used device for the read head is the tunnel magnetoresistance with an MgO barrier [17]. The performance of read heads is given by the resolution, the signal-to-noise (S/N) ratio, and the high frequency property. Briefly, the reading resolution is given by the size of the read head, thus the read gap (shield-to-shield gap) has to be sufficiently small. The S/N ratio is determined by the magnetoresistive output voltage $\Delta V = \Delta RA \times J_{\mathrm{sense}} = \mathrm{MR\ ratio} \times V_{\mathrm{bias}}$, where ΔRA is the resistance change-device are product, J_{sense} is the sense current density and V_{bias} is the applied bias voltage to the head. The high frequency property is given by the resistance of the read head because the resistance and the capacitance of the circuit of the system form a low path filter. Moreover, the impedance matching between the head and the amplifier is also an important issue. Therefore, a read head with a thin total thickness, a large MR output, and a small device resistance is required for realizing the ultrahigh density recording.

Takagishi *et al.* of Toshiba Corp. have reported the required properties of the read heads for a 2 Tbit/in^2 recording density based on their micromagnetic simulations as shown in Fig. 1-9 [16]. The required MR ratio shows a minimum value at RA ~ 0.1 $\Omega\mu\mathrm{m}^2$. The requirement of MR ratio rapidly increased with increasing RA. The value of RA of the TMR read heads is ~0.4 $\Omega\mu\mathrm{m}^2$ even with a very thin MgO barrier of 1 nm [17]. Thus, a further reduction of RA by thinning the barrier thickness is indispensable for MgO-based TMR heads to be applied to the read heads for over 2 Tbit/in^2 recording. However, it seems to be extremely difficult for TMR heads because of the rapid reduction of TMR with the thinner barrier [17]. Achieving the low RA is easy for CPP-GMR composed of metallic layers. Childress *et al.* demonstrated the feasibility of a CPP-GMR with RA of 0.06 $\Omega\mu\mathrm{m}^2$ for read head [18]. However, the value of the MR output arise a problem for CPP-GMR. Using conventional ferromagnetic materials such as CoFe and NiFe, only ΔRA of at most 2 m$\Omega\mu\mathrm{m}^2$ with the MR ratio of several % has been obtained [18]. The small MR output is because of the small resistance of the active

part of the magnetoresistance, which is expected to be less than several mΩμm^2. Thus, the absolute value of the resistance change is small even if the intrinsic MR ratio is comparable to those of TMR. Therefore, enhancement of the MR output, namely the enhancement of Δ*RA* is the central issue to achieve the read head with CPP-GMR. The simulation by Takagishi *et al*. indicated that Δ*RA* of 15 mΩμm^2 is the minimum value for the read head of 2 Tbit/in$_2$ recording even with a large sense current density of 1×10^8 A/cm^2 [16].

The requirement of the size is critical for the resolution of the read head. The current read heads utilize the exchange biased spin-valve with a synthetic antiferromagnet structure for a sufficient pinning force, the thickness of these layers is typically ~10 nm. The shield-to-shield gap of heads for 2 Tbit/in^2 is expected to be ~20 nm [16], thus the magnetoresistive part (F/N/F trilayer for CPP-GMR) has to be thin enough to fit the narrow gap spacing. Therefore, obtaining large MR output using thin ferromagnetic layers is indispensable for CPP-GMR read head for Tbit/in^2 recording.

The effect of the spin torque induced by the current is also important [19][20]. The sense current density is assumed to be ~1×10^8 A/cm^2 for the CPP-GMR read heads to obtain a sufficient output voltage. Such a large current may induce effects by the spin torque. The spin torque will induce a precession of the magnetization, by which Δ*RA* decreases and the liner response of the sensor is distorted. The critical current density of the appearance of the spin torque is governed by the damping torque as given in the Landau-Lifshitz-Gilbert equation. Thus, materials with large damping factor are thought to be important for the read head application.

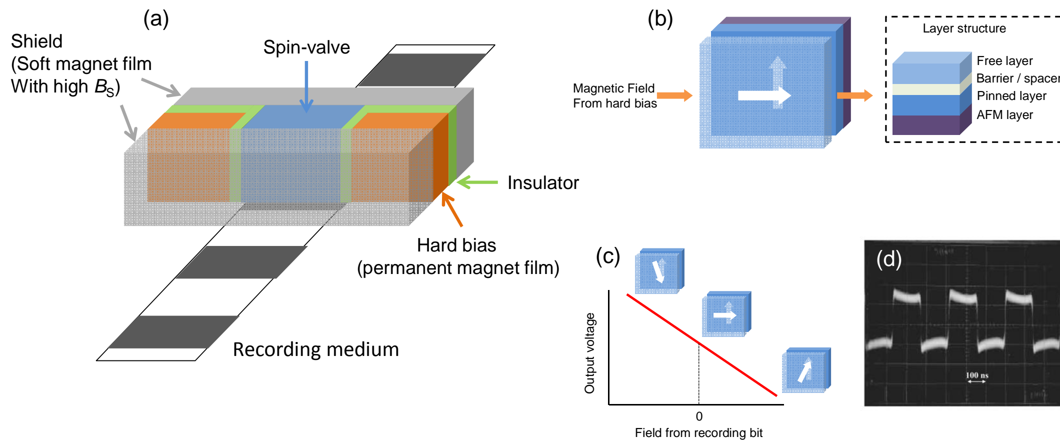

Fig. 1-8 (a) Schematic structure of spin-valve read head of hard disk drive, (b) magnetization configuration between the pinned and free layer in an absence of external magnetic field, (c) the relationship of the field from the recording bit and the output voltage, (d) wave shape of the sensor output by Childress et al. [18].

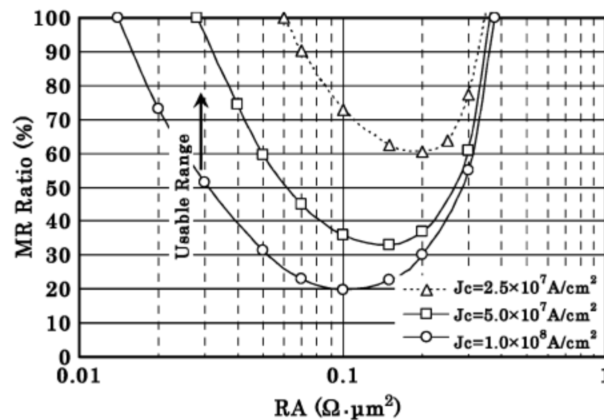

Fig. 1-9 Requirement of RA and MR ratio for the read head of 2 Tbit/in^2 with various critical sense current densities of spin transfer torque J_c. By Takagishi *et al.* [16]

1.3.2 Spin torque oscillators for microwave generation

Another application of CPP-GMR is a microwave oscillator by the spin transfer torque, called spin torque oscillator (STO). The STO was first demonstrated by a group of Cornell University with Co/Cu/Co CPP-GMR device [21]. The spin torque from one ferromagnetic layer causes a procession of the magnetization of the other ferromagnetic layer at certain values of current. The frequency of the magnetization precession is

given as $\frac{\gamma}{2\pi}H_{\mathrm{eff}}$ by the Landau–Liftshitz–Gilbert (LLG) equation, where γ is the gyromagnetic ratio (for isolated electron, $\gamma = 1.7\times10^7$ rad/sec·Oe = 2.7 GHz/kOe) and H_{eff} is the effective magnetic field. The experimental data of the oscillation frequency as a function of the external field in the Co/Cu/Co devices shows a good agreement with the Kittel's equation which gives an expression of H_{eff} as shown in Fig. 1-10. The frequency is in a range from a few to a few ten GHz.

The applications of the STO would be a chip-to-chip wireless communication in integrated circuits, radars and a microwave assisted magnetic recording (MAMR). The oscillation frequency, the oscillation power, and the band width of frequency (Q-factor) are important factors for the applications. To utilize the microwave as an electric signal like the wireless communication, a large power would be required. Thus, magnetic tunnel junction showing a large tunnel magnetoresistance ratio is thought to be the target device. One the other hand, if one utilizes the rf magnetic field generated from a magnetic layer like the MAMR application, the MR ratio is nothing important directly, but the magnetic moment of the oscillator and the oscillation mode are important to obtain a large amplitude of the microwave. A product of the saturation magnetic flux density (B_s) and the layer thickness (t) is often called magnetic thickness. The out-of-plane oscillation mode is obtainable at certain ranges of the external field and the current as shown in Fig. 1-11 by micromagnetic simulations, showing the out-of-plane oscillation mode in the large current and the high external field region. Thus, oscillating a thick magnetic layer with a large B_s at an out-of-plane mode is critical for the MAMR application. a low device resistance is required to apply a large current in the STO layers. Thus, all-metallic CPP-GMR is considered to be the promising candidate of the STO for MAMR.

MAMR is a candidate of a writing assistance for recording media with a high perpendicular magnetocrystalline anisotropy. For example, a FePt-based granular films exhibits a very high coercivity of 37 kOe with the perpendicular magnetocrystalline anisotropy of $K_u = 4\times10^7$ erg/cc, thus this film has been considered to be a future reading medium showing a very high thermal stability factor of $K_uV/k_BT \sim 300$ [22]. However, writing such a high coercive material is impossible using a conventional write head with FeCo pole (yoke). The B_s of the FeCo alloy is 2.4 T at $Fe_{70}Co_{30}$, thus the writing field available with the conventional head is theoretically up to 2.4 T (24 kOe) even with a zero head-media spacing. Thus, it is necessary to decrease the coercivity of the recording medium locally only when the magnetization is switched. The proposed

approaches are the heat assisted magnetic recording (HAMR) (also called thermal assisted recording, TAR) and the MAMR. HAMR utilizes a temperature increase of the recoding bit by an irradiation of laser or near-field light. One the other hand, MAMR utilizes a ferromagnetic resonance of the medium material, which was first proposed by Zhu *et al*. of Carnegie Mellon University [23]. Figure 1-12 shows the write head for MAMR schematically. The spin torque oscillator is inserted in the gap between the write and the return poles. When the frequency of the AC field generated from the spin torque oscillator matches the ferromagnetic resonance frequency of the recording medium material, the magnetization of the recoding medium resonates and the coercivity decreases. Then, write field is applied to switch the recording bit. Nozaki *et al*. [24] and Yoshioka *et al*. [25] demonstrated a magnetization reversal by microwave assist using Co/Pd perpendicularly magnetized film (anisotropy field H_k = 20 kOe) and a coplanar wave guide. They observed a microwave assist magnetization reversal by applying a 30 GHz ac field. The ferromagnetic resonance frequency is given by

$$f_{\mathrm{FMR}} = \frac{|\gamma|}{2\pi}\left(H_{\mathrm{k}} - 4\pi M_{\mathrm{s}}\right), \tag{1.6}$$

where M_s is the saturation magnetization. The f_{FMR} of the FePt recording medium is estimated to be several tens GHz. Thus, obtaining such a high oscillation frequency is critical for the realization of MAMR. As seen from the LLG equation, increasing the effective field leads to higher oscillation frequency. Fortunately, a large magnetic field (~ 10 kOe) is applied at the gap between the write and return poles, thus increasing the effective filed is achievable by the external filed from the poles. Very recently, Yamada *et al*. demonstrated a 25 GHz oscillation under a 8.8 kOe external field [26]. The other approach to increase the effective field is an exchange coupling by perpendicularly magnetized layer adjacent to the oscillator layer proposed by Zhu *et al*.

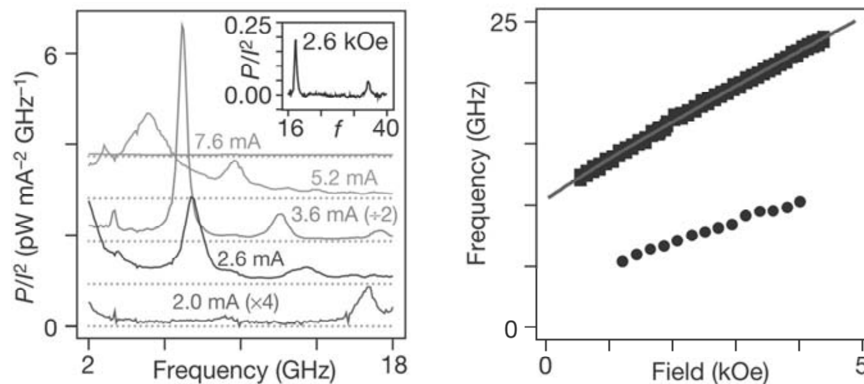

Fig. 1-10 Microwave oscillations in Co/Cu/Co nanopillar by Kiselev *et al.* [21].

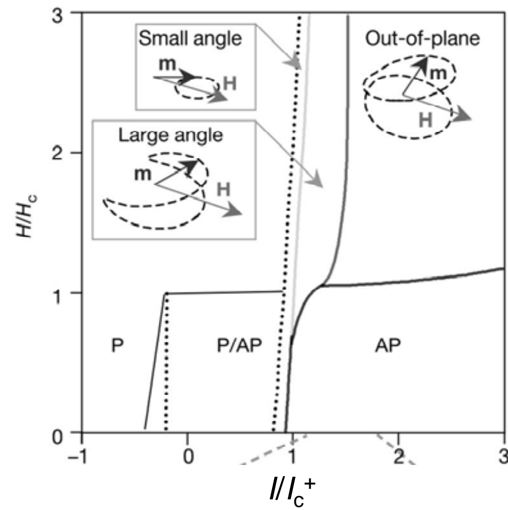

Fig. 1-11 Phase diagram of the oscillation mode in the Co/Cu/Co nanopillar for current and external field. Ref. [21].

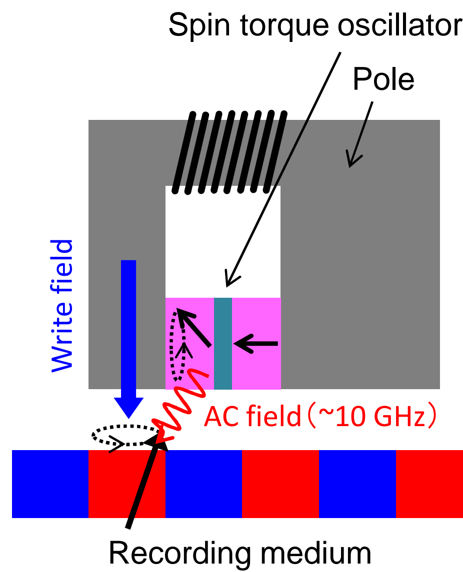

Fig. 1-12 Schematic structure of a write head for the microwave assisted magnetic recording (MAMR). A spin torque oscillator is inserted between the write and return poles. Ref. [23].

1.4 Co-based Heusler alloy

1.4.1 General introduction of half-metal

Half-metal has been discovered theoretically by de Groot *et al.* and his colleagues in 1983 [28]. They conducted a first principle calculation of the band structure of the NiMnSb half Heusler alloy and showed that it had a metallic band structure for the up spin band, whereas the down spin band had a gap near the Fermi energy as show in Fig. 1-13. Since such materials have the metallic property for only the half of the electrons with one spin direction, they are called *half-metals*. So far, (1) half Heusler alloys, (2) full Heusler alloys, (3) Perovskite or double Perovskite oxides, (4) others Fe_3O_4, CrO_2, $Co_{1-x}Fe_xS_2$ etc. have been predicted to be half-metals.

In these materials, the half-metallic properties of CrO_2, $Co_{1-x}Fe_xS_2$, $La_{0.7}Sr_{0.3}MnO_3$ and Co_2MnSi full Heusler alloy have been experimentally demonstrated at low temperature. However, the oxide half-metals have low Curie temperatures (370 K for $La_{0.7}Sr_{0.3}MnO_3$ and 398 K for CrO_2), the spin polarizations should be miserably low at room temperature. One the other hand, half and full Heusler alloys have generally high Curie temperatures (730 K for NiMnSb and 980 K for Co_2MnSi), therefore there may be a possibility to obtain the half-metallic property even at room temperature. Especially, the full Heusler alloy with the $L2_1$ ordered structure does not have any vacant site unlike the half Heusler alloy with the $C1_b$ structure, therefore they are more stable.

The half-metallic material should be an ideal material as high spin polarized current sources to realize a very large magnetoresisnce, a low current density for current induced magnetization reversal, and an efficient spin injection into semiconductor.

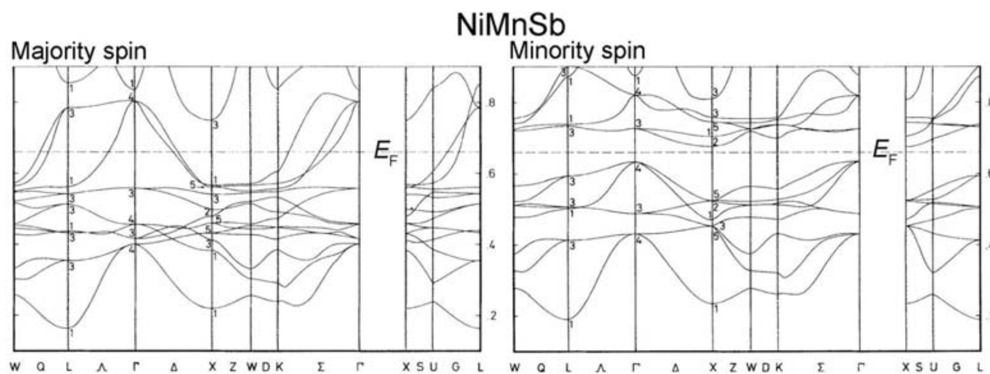

Fig. 1-13 Calculated spin-resolved band dispersions of NiMnSb by de Groot *et al.* [28].

1.4.2 Crystal structure of full Heusler alloy

In 1903, a German scientist Friedrich Heusler discovered that a Cu_2MnAl alloy was ferromagnetic despite the nonmagnetic constituents, and that the structure was the $L2_1$ ordered structure. Since then, alloys with the composition of X_2YZ and the $L2_1$ structure are called Heusler alloys, where X and Y are transition metals and Z is a main group element. The $L2_1$ structure is composed of four fcc sublattices as show in Fig. #. The atomic positions are A (0 0 0), B (1/4 1/4 1/4), C (1/2 1/2 1/2) and D (3/4 3/4 3/4). The X element occupies the A and C sites, the Y element occupies the S site, and Z element occupies the D site. The structure factors are

$L2_1$ superlattice (h, k, l all odd): $F_{L2_1} = |4(f_X - f_Z)|$

B2 superlattice (h, k, l all even, $h + k + l = 4n+2$) $F_{B2} = |4(2f_X - f_Y - f_Z)|$

Fundamental (h, k, l all even, $h + k + l = 4n$) $F_{fund} = |4(2f_X + f_Y + f_Z)|$,

where f is the atomic scattering factor and n is integer. The $L2_1$ diffraction vanishes by the mixing of the constituent elements between the X and Z sites, and the B2 diffraction vanishes by the mixing among all the elements. For an example, figure 1-15 shows the powder x-ray diffraction (XRD) patterns of Co_2FeSi and Co_2FeAl alloys. The 111 diffraction peak is observed only for the Co_2FeSi alloy, thus the structure of the Co_2FeSi is the $L2_1$ structure, whereas that of Co_2FeAl is the B2 structure. The difference of the ordering between the two alloys is due to the difference of the driving force for the $L2_1$ ordering. We can know the ordered structure from the XRD pattern and can estimate the degree of order quantitatively from the intensity. It should be noted that, however, the disordering between the X and Y elements is hard to detect by of most of the Co-based Heusler alloys because of the close atomic numbers, *i.e.* Co and Mn or Co and Fe.

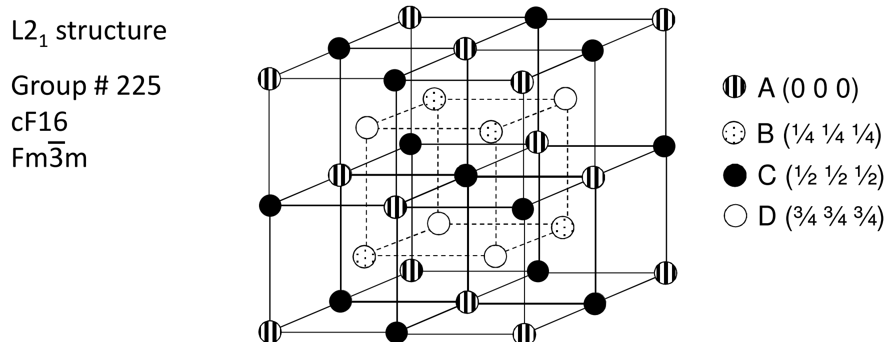

Fig. 1-14 Crystal lattice of $L2_1$ ordered structure.

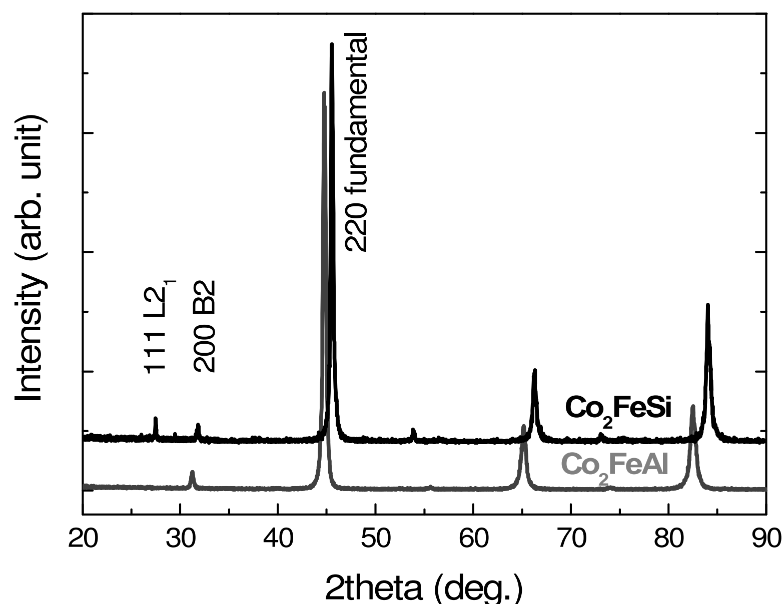

Fig. 1-15 Powder x-ray diffraction patters for L2$_1$ ordered Co_2FeSi and B2 ordered Co_2FeAl Heusler alloys. From Nakatani's master degree thesis work.

1.4.3 Thermodynamic property

Heusler alloys generally have order-disorder transformations below the melting points. The L2$_1$ structure disorders by two steps: L2$_1$→B2→A2 with increasing temperature as shown in Fig. 1-16. Webster investigated the chemical ordering of a Co_2MnAl Heusler alloy at various temperatures using a high temperature x-ray diffractometer. Figure 1-17 is the temperature variation of the 111 L2$_1$ and 200 B2 superlattice diffraction peaks of the Co_2MnAl alloy. The L2$_1$ peak disappears at around 1000 K, thus indicating the L2$_1$–B2 phase transformation. The B2 peak disappears at around 1250 K, indicating the B2–A2 phase transformation.

For the Co-based alloys, Umetsu *et al.* studied the order-disorder and magnetic transformations of the $Co_2MnAl_xSi_{1-x}$ alloys systematically [30]. The order-disorder transformation was measured by the thermal analysis using a differential scanning calorimetry (DSC) as shown Fig. 1-18(a). They found that the order-disorder (L2$_1$–B2) transformation temperature increased linearly with increasing Si content, and that of Co_2MnSi exceeded the melting point. In other words, Co_2MnSi is an intermetallic compound where the L2$_1$ ordered structure is stable up to the melting point. The order-disorder temperature is an important factor to obtain high degree of order in thin

films. Usually, as-deposited films are disordered (typically, imperfect B2 ordered), thus annealing is necessary to obtain the well-ordered structures of the Heusler alloys. The order-disorder temperature is an indication of the driving force of the chemical ordering. The Co_2MnSi alloy is regarded as one of the best alloys for TMR and CPP-GMR devices, the one of the reasons may be that the $L2_1$ ordered structure is obtained by relatively low annealing temperature (~350 °C [31]). The low annealing temperature for obtaining the $L2_1$ structure is considered to be due to the high phase stability of the $L2_1$ structure of being an intermetallic compound. Therefore, the thermodynamic property is an important point of view for the choice of the composition of the Heusler alloys.

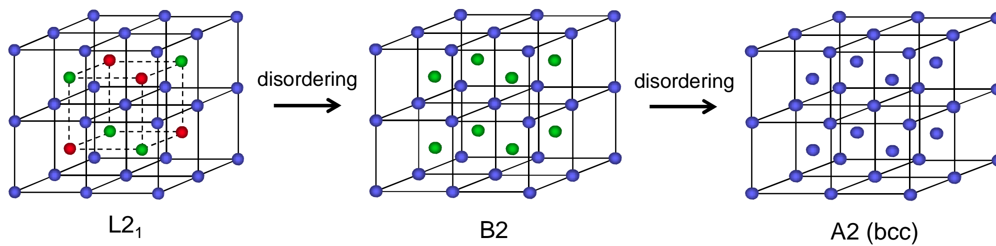

Fig. 1-16 Order-disorder transformations of the $L2_1$ structure.

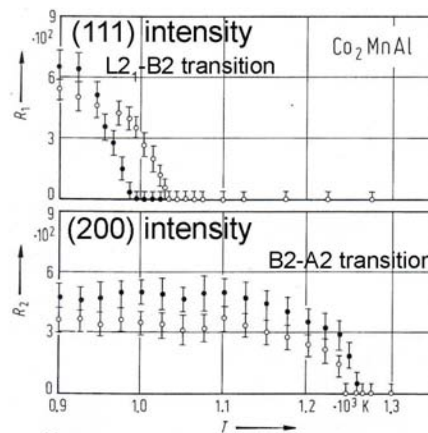

Fig. 1-17 Variations of the (111) $L2_1$ and (200) B2 super lattice diffraction intensities dependent on temperature. By Webster [29].

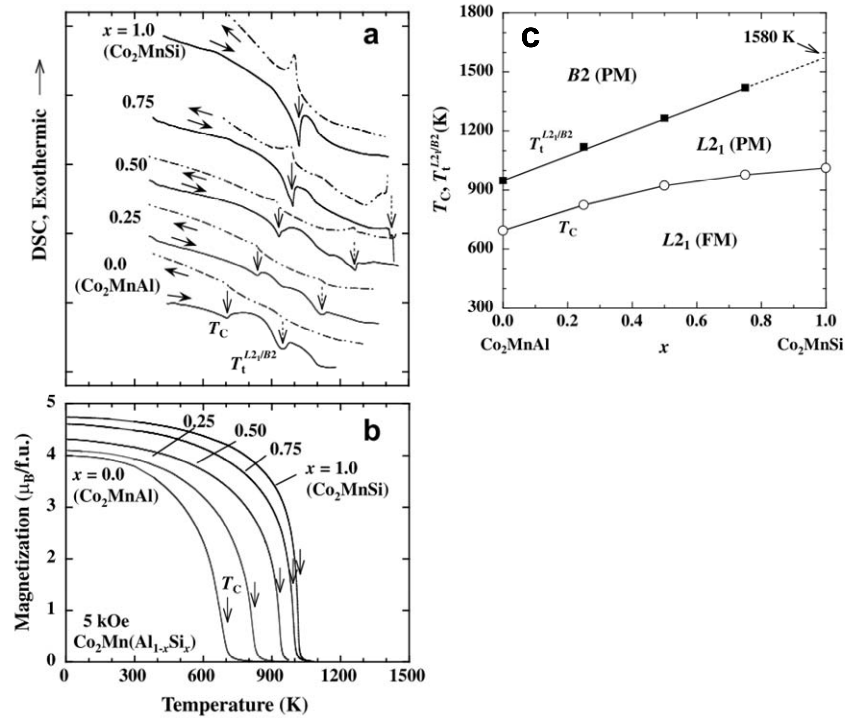

Fig. 1-18 Thermodynamic properties and the magnetic propertied of $Co_2MnAl_xSi_{1-x}$ by Umetsu *et al.* [30]. (a) Deferential scanning calorimetry (DSC) curves, (b) magnetization–temperature curves, and (c) the composition dependence of the $L2_1$–B2 transition temperature and the Curie temperature.

1.4.4 Electronic structure

Figure 1-19 shows the density of states (DOS) of (a) the total electron and (b)–(d) the electron of each constituent element of Co_2MnX (X = Si, Ge, Sn) reported by Picozzi *et al.* [32]. Si, Ge and Sn create the electronic states in energy levels deep from the Fermi ebergy. On the other hand, Co and Mn form large density states at the higher energy level, which correspond to the *d* hybrid bands. It should be noted that the width of the band gap of the total DOS is given by Co. Thus, the gap width is determined by the Co band.

The mechanism of the formation of the minority gap has been explained by Galanakis *et al.* for Co_2MnZ alloys [33]. According to them, the Co atom in the $L2_1$ structure is surrounded by two Mn and two Z atoms as the nearest neighbors, thus, the symmetry is 4-fold. One the other hand, the one Co atom is surrounded by eight Co atoms as the second nearest neighbor, thus 8-fold symmetry. Co orbital first hybridizes

with other Co orbital due to the higher symmetry, thus the d states ($d_{1,2,..,5}$) forms bonding states of $2\times e_g$ and $3\times t_{2g}$, and anti-bonding states of $3\times t_{1u}$ and $2\times e_u$, where the number indicated the degeneracy as shown in Fig. 1-20(a). Next, the five d states of Mn hybridize with the five bonding states of the Co-Co hybridization .Then, the anti-bonding states of Co-Co remains without hybridizing with Mn. As shown by the ab intio calculation of the DOS of Co_2MnGe (Fig. 1-20(b)), the energy levels of t_{1u} and e_u are just below and above the Fermi level, respectively, thus these anti-bonding states forms the edges of the band gap of the down spin band. Therefore, the width of a full Heusler alloy is determined by the strength of the hybridization of the Co-Co second nearest pair, which is weaker than those of the half-Heusler alloys where the gap width is determined by the hybridization of X-Y first nearest pair.

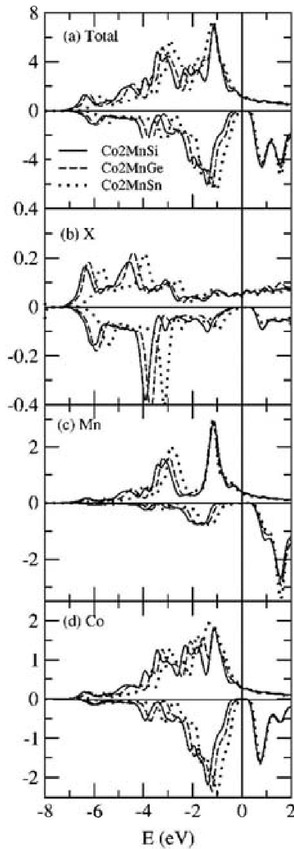

Fig. 1-19 Density of states DOS of Co_2MnX (X = Si, Ge, Sn) Heusler alloys. (a) the total DOS, and the partial DOSs composed of (b) X elements, (c) Mn, and (d) Co.
Ref. [32].

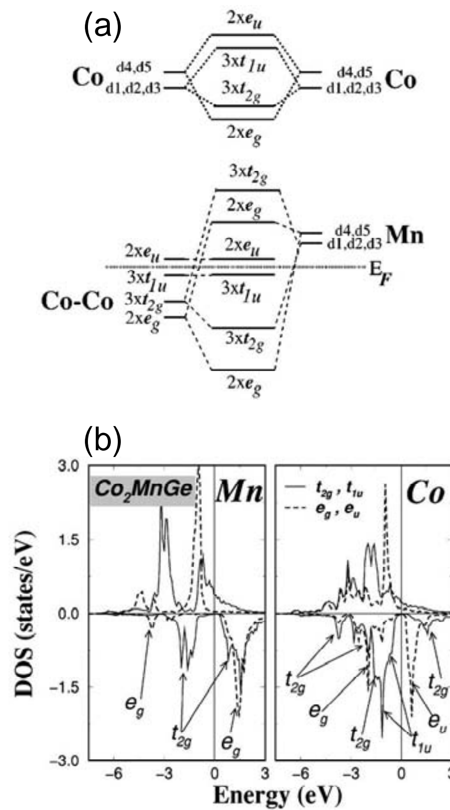

Fig. 1-20 (a) Orbitals formed by the hybridizations between Co and Co (top) and Co-Co and Mn (bottom). (b) Calculated density of states of Co_2MnGe. Ref. [33].

Although the *Z* elements (*sp* main group elements) do not contribute to the shape of the DOS near the Fermi level directly, the position of the Fermi level can be tuned by the *Z* elements. The reason is as follows. The Z elements has one *s* orbital and three *p* orbital for both spins, thus they can accommodates up to 8 electrons. However, the *Z* elements have only 3 (Al, Ga) or 4 (Si, Ge, Sn) valence electrons. Thus, the remaining 5 or 6 vacancies are occupied by the electrons which come from the *X* and *Y* elements. This means that the total number of electron that is, the position of the Fermi level can be tuned by substituting the *Z* elements with anther elements. The substitution of the *Z* element also tunes the magnetization as mentioned next.

The magnetization of itinerant ferromagnetic materials (band ferromagnets) is given by [(number of up spin electrons)–(number of down spin electrons)]$\times\mu_B$, where μ_B is the Bohr magneton. In half-metallic full Heusler alloys, the number of the *d* states derived from the Co and *Y* element is 8 and that from the *Z* element is 4 for each spin. The 12 states of the down spin electrons are located below the Fermi level, thus they are fully occupied. One the other hand, the up spin accommodates the remaining Z–12 electrons, where Z is the number of the total valence electron of the full Heusler alloy. Therefore, the magnetizations of the half-metal full Heusler alloys are integer in a unit of μ_B,

$$\begin{aligned} M &= (Z-12)-12 \\ &= Z-24\ (\mu_B). \end{aligned} \tag{1.7}$$

This proportional relationship between the electrons number and the magnetization is the so called Slater-Pauling rule. Indeed, most of the Heusler alloys follow the Slater-Pauling rule as shown in Fig 1-21. Thus, following the Slater-Pauling rule is considered as a necessary condition for Heusler alloys to be half-metals.

The electronic structure and the magnetization can be engineered by substituting the constituents with other elements. Galanakis theoretically showed that the linear change of the magnetization of quaternary Heusler alloys as a function of the composition with following the Slater-Pauling rule Eq. (1.7) [34]. This means that the quaternary Heusler alloy maintains the half-metallic property. The Slater-Pauling behavior of the magnetization of a quaternary Heusler alloy systems have been experimentally shown. Figure 1-22 shows the magnetization values of $Co_2Mn_{1-x}Fe_xSi$ alloys reported by Balke *et al*. [35]. The magnetization surely follows the Slater-Pauling rele experimentally, the half-metallicity has been predicted by their *ab initio* calculations [35].

A serious problem of the half-metallic Heusler alloys to utilize them in real devices is that the half-metallicity is easily destroyed by chemical site disordering. Picozzi *et al.* carried out *ab initio* DOS calculations of Co_2MnGe and Co_2MnSi alloys with site disordering [36]. They showed the Co-antisite and the site swapping between Co and Mn formed electronic states in the minority gap, by which the half-metallicity was destroyed. In order to suppress the degradation of the spin polarization by the site disordering, quaternary alloying is a promising strategy. This is the due to the concept to tune the position of the Fermi level by substituting the constituent of the Heusler alloy with other elements. The effect of the Fermi level tuning has been demonstrate both experimentally and theoretically for a $Co_2FeAl_xSi_{1-x}$ system [37], which will be describes in 3.1.

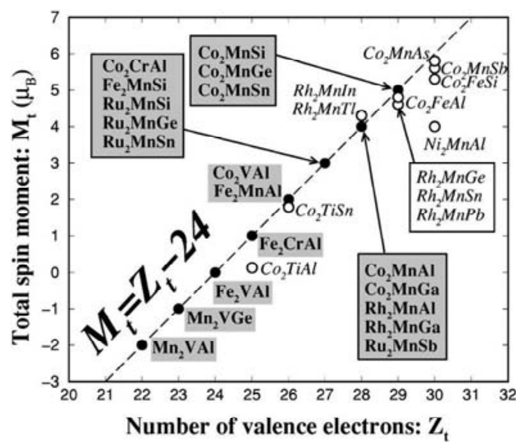

Fig. 1-21 Slater-Pauling rule of half-metallic Heusler alloys. The alloys indicated by the open circles are not half-metals theoretically. Ref. [33].

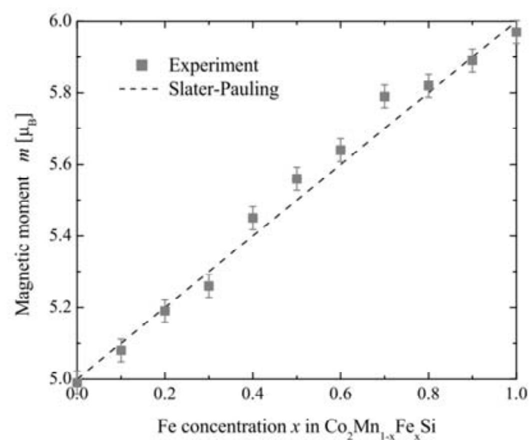

Fig. 1-22 Variation of the magnetization of $Co_2Mn_{1-x}Fe_xSi$ alloys which follows the Slater-Pauling rule. Ref. [35].

1.4.5 Application to tunnel magnetoresistance (TMR) devices

Half-metal is an ideal material for the electrodes of magnetic tunnel junctions. The Julliere's equation gives TMR ratio = $2P_1P_2/(1-P_1P_2)\times100$, thus half metallic electrodes provide huge TMR ratios. The first experimental demonstration of TMR using Heusler alloy electrodes was reported by Inomata *et al*. using poly-crystalline $Co_2Cr_{0.6}Fe_{0.4}Al$ for the bottom electrode and CoFe for the top electrode [38]. They obtained 16% at room temperature. In 2005, Sakuraba *et al*. showed a large tunnel spin polarization of a Co_2MnSi single crystal electrode at 2 K to be 0.89 [39] using an amorphous Al-O barrier and CoFe for the top electrode. They observed a clear feature of the band gap in the minority spin band [40]. By using the Co_2MnSi alloy as the top electrode, Sakuraba et al. obtained a huge TMR ratio of 590% at 2 K. The remarkable feature of the TMR devices using Heusler alloys are the large temperature dependence of the TMR ratio. The MR ratio of the Co_2MnSi/Al-O/Co_2MnSi MTJ decreased to 70% at room temperature which is comparable to those with CoFe electrodes [40]. The origin of the large temperature dependence of the TMR ratio has been discussed to be (i) the thermal excitation of the minority spin state, (ii) the magnon excitation by the minority interfacial state [42], and (iii) the reduction of the exchange energy of Co at the interface with the barrier [43]. However, the large temperature dependence of the TMR ratio has not been overcome sufficiently.

1.5 Current status of the CPP-GMR research

As mentioned above, the CPP-GMR output, Δ*RA* (resistance change-area product) obtained with conventional ferromagnetic materials (*e.g.* CoFe or NiFe) is only 1–2 mΩμm^2. This is insufficient for the applications like read reads for the magnetic recording density above 1 Tbit/in^2. Currently, much effort is being devoted to enhance the CPP-GMR output mainly by two ways; (1) with a new spacer layer structure with confined current paths, and (2) with new ferromagnetic material showing a large spin-dependent scattering. This section will review the current researches and the progresses of CPP-GMR devices.

1.5.1 Current-confine-path nano-oxide-layer (CCP-NOL) spacer

The concept of the CPP-MR device with a current-confined-path (CCP) nano-oxide-layer (NOL) (or called current-screen-layer) is to enhance the resistance of the active part for the magnetoresistance, *i.e.* pinned layer/spacer layer/ free layer. Since the resistance of the active part of the metallic CPP-GMR trilayer, the absolute value of the resistance change is small. The hint of the usage of the CCP-NOL for CPP-GMR was a specular spin-valve for CIP-GMR, which composed of a dual spin-valve structure with NOLs in the synthetic antiferromagnetic layers [44]. In such devices, electrons transporting in the film plane are reflected by the NOLs. The specular reflection at the NOLs effectively concentrates the current within the active part, thus enhances the CIP-GMR.

A similar approach was attempted to CPP-GMR, a thin oxide layer, but with nano-scale metallic paths was applied to the spacer. Fukuzawa *et al.* first reported an MR ratio of 5.4% and *RA* of 0.5 Ωμm^2, which corresponds to Δ*RA* of 27 mΩμm^2 [45]. They fabricated the CCP-NOL by oxidizing AlCu film into the Al_2O_3 insulator and the partially oxidized Cu metallic path. FeCo alloy was used for the ferromagnetic layer. Based on the two current model, they discussed that the confinement of the spacer layer enhanced the resistance change and pointed out that reducing the resistivity of the CuO_x should enhance the MR ratio further as shown in Fig. 1-23 [46]. Thus, the purification of the Cu metallic path is a key to obtain a larger MR ratio. Recently, they applied a hydrogen ion treatment to deoxidize the CuO_x and reported 27% MR ratio with *RA* of 2.9 Ωμm^2 and 25% with 0.5 Ωμm^2 [46]. In addition, they pointed out that a further purification of the Cu metallic path would realize MR ratio 50% with *RA* of 0.5 Ωμm^2 [46]. The size of the metallic path has been reported to be 5-10 nm by atom probe analysis [47] The CCP-CPP-GMR has been studied in different places other than

Toshiba. Hitachi reported an MR ratio of 17% with *RA* = 0.2 Ωμm^2 [48]. The materials used for their devices have not been published. Seagate reported an MR ratio of ~15% with *RA* = 0.1 Ωμm^2 using CoFe magnetic layers and a Cu-Al_2O_3 CCP-NOL [49]. It is surprising that such an improvement of MR has been achieved even only by developing the spacer layer with using the normal ferromagnetic layer. Thus, further enhancements of the MR properties are expected by applying advanced ferromagnetic materials with a high spin asymmetry of scattering.

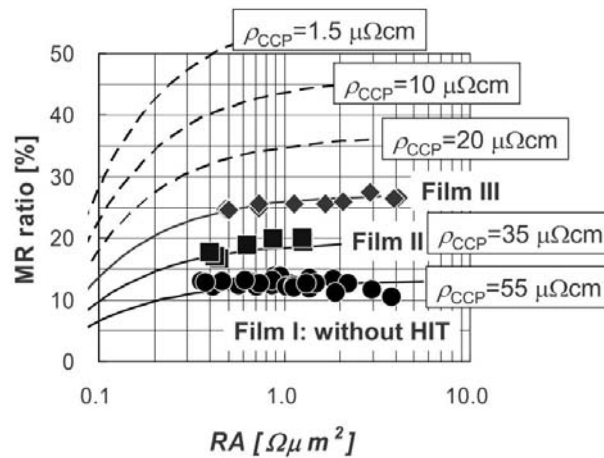

Fig. 1-23 MR ratio and *RA* of CoFe/Cu-AlO/CoFe CCP-GMR devices for various resistivities of the Cu metallic path layer. Yuasa *et al*. [46].

In order to achieve CCP-CPP-GMR devices feasible for read heads, there may be two issues to be solved. First, the reduction of the *RA* down to 0.1 Ωμm^2 with keeping the high MR ratio is importance. Although the current achievements of the devices with CCP-NOL are excellent for the GMR devices, the values of *RA* and the MR ratio are not competitive with the TMR devices with MgO barriers showing 50% with *RA*=0.4 Ωμm^2 [50]. Second, the achievement of the very small size and the homogeneous distribution of the metallic paths is crucial for the industrial production of the read heads whose size will be ~20 nm for the 2Tbpsi recording [16].

1.5.2 Development of ferromagnetic materials

Enhancing the spin dependent scattering improves the CPP-GMR output, namely enhances the resistance change-area product (ΔRA) and the MR ratio. As Eq. (1.3) indicates, ΔRA is determined by the two terms, *i.e.* the spin polarization term (β and γ) and the resistance term (ρ_F and $AR_{F/N}$). Thus, there are mainly two strategies to enhance CPP-GMR output. The one is to utilize highly spin polarized materials which should provide high spin-dependent scattering. The other way is to increase the resistivity of the ferromagnetic materials.

Utilization of the Co-based Heusler alloys is an effective approach to enhance CPP-GMR. This is because the theoretically predicted high spin polarization is expected to give a large spin asymmetry of electron scattering in the bulk of the ferromagnetic layers or at the interface with the spacer layers. The first report of the CPP-GMR device with a (potentially) high spin polarized material seems to be for NiMnSb/Cu/NiMnSb by Caballero *et al*. [51]. They obtained CPP-GMR ratio up to 10% at 4.2 K, which was higher than those with the conventional ferromagnetic materials. Hoshiya and Hoshino reported the effects of insertions of Fe_3O_4 or Co_2MnGe layers in the CoFe film of the CoFe/Cu/CoFe spin-valves. They obtained an enhancement of ΔRA up to ~ 2 m$\Omega\mu m^2$ [52]. Yakushiji *et al*. prepared CPP-GMR pseudo spin-valves with $Co_2MnSi/Cr/Co_2MnSi$ and obained a large ΔRA of 19 m$\Omega\mu m^2$ and the MR ratio of 2.4% at room temperature [53]. However, the value of ΔRA is thought to be overestimated due to the current crowding effect, because they fabricated the device on Cr(10 nm) whose lead resistance should be too high to be used for a lead electrode of CPP-GMR devices. Childress *et al*. fabricated real read head using Heusler alloy (composition not published). The read head showed ΔRA of 2.3 m$\Omega\mu m^2$ and the MR ratio of 5.5% and the feasibility for ~400 Gbit/in^2 recording density was demonstrated [54]. So far, a lot of papers on CPP-GMR with Co_2MnSi [53][55],[58]–[61][64][65], Co_2MGe [62], $Co_2Fe(Al_{0.5}Si_{0.5})$ [57],[63],[64], some unpublished compositions [54][56] and newly developed alloy compositions based on the alloy search by the PCAR method, *e.g.* $Co_2(Cr,Fe)Si$ [66] and $Co_2Mn(Ga,Sn)$ [66] have been reported. The highest CPP-GMR value has been reported using an epitaxial $Co_2MnSi/Ag/Co_2MnSi$ device to be ΔRA = 11 m$\Omega\mu m^2$ at room temperature [65]. They used 10 nm Co_2MnSi layers for the devices, by which the bulk spin-dependent scattering in the Co_2MnSi layer effectively enhances ΔRA. With layer structure for practical read heads, ΔRA of 4 m$\Omega\mu m^2$ with $Co_2MnGe/Rh_2CuSn/Co_2MnGe$ has been reported using 3.6 nm thick Co_2MnGe layers [62]. They demonstrated the reading feasibility for a recoding density of 670 Gbit/in^2.

Heusler alloys are not only the materials showing large spin polarizations. An artificially fabricated superlattice film has been reported to possess a high spin polarization. Mano *et al*. fabricated CPP-GMR spin-valves with monoatomically alternated Fe/Co(001) films, which correspond to the B2-ordered FeCo alloy [68]. They obtained ΔRA of 2.6 m$\Omega\mu$m^2 at room temperature using 5 nm thick single crystalline Fe/Co superlattice. They estimated the bulk scattering spin asymmetry of the Fe/Co superlattice to be β = 0.81, which is significantly higher than that of $Fe_{50}Co_{50}$ chemically disordered alloy of β = 0.62 [70].

The other strategy to enhance CPP-GMR output is to increase the resistivity of the magnetic layers. Materials with both high resistivity and high spin asymmetry are ideal; however, both high resistivity and high bulk scattering may be difficult to obtain simultaneously. This can be understood as follows. The resistivity of ferromagnetic is given by a total resistance of the parallel resistance circuit composed of the majority (up) and the minority (down) spin channels, thus dominated by the resistivity of the majority channel with the lower resistivity. Thus, the high resistivity of a magnetic material indicates that the scattering rate of the majority spin electrons is high. On the other hand, a high bulk scattering spin asymmetry is given by a situation that the down spin electron is more scattered than the up spin electrons. Therefore, the two physical factors of the resistivity and the spin asymmetry may tend to trade off. In addition, high resistivity materials are expected to have short spin diffusion lengths [69].

Despite general tendency as mentioned above, alloying Al or Ge into $Co_{50}Fe_{50}$ has been demonstrated to maintain the spin asymmetry of the bulk scattering, while it increases the resistivity, which effectively enhance ΔRA [72][73][74]. Especially, the $Co_{50}Fe_{50}$–Ge has a higher β of 0.71 despite the resistivity 5 times higher than that of $Co_{50}Fe_{50}$, by which a relatively high ΔRA of 2.6 m$\Omega\mu$m^2 has been obtained with the layer structure capable of a real read head. Studies of the electronic structure are awaited on the correlation between the alloying elements and the effect on the scattering spin-dependence. The resistivities and the bulk scattering spin asymmetries of CoFe based alloys are summarized in Table 1-1

Although enhancements of CPP-GMR output have been achieved for some extent by improving the magnetic materials, the value of ΔRA is still insufficient to be applied to the read heads for over Tbit/in^2 recording as simulated by Takagishi *et al*. (Fig. 1-9) [16]. Therefore, a further development of materials or some breakthrough is necessary to open the door of the ultrahigh density magnetic recording.

Material	ρ (μΩcm)	β	Reference
$Co_{50}Fe_{50}$	12	0.62	[70]
$Co_{90}Fe_{10}$	13	0.55	[70]
CoFe+Cu lamination	12	0.77	[70]
CoFeB	30	0.59	[71]
$Co_{50}Fe_{50}$–Al	91	0.54	[72]
CoFe–Al	130	0.49	[73]
$Co_{50}Fe_{50}$–Ge	63	0.71	[74]

Table 1-1 Resistivity, bulk scattering spin asymmetry β and ΔRA for various CoFe based alloys.

1.6 Purpose of the study

As introduced in this chapter, the realization of large CPP-GMR outputs is significant because it enables us to obtain read heads for ultrahigh density magnetic recording and microwave oscillators. Thus, developments of the materials based on the understanding of the spin-dependent transport in CPP-GMR devices are indispensable. So far, the utilization of the Heusler alloys has been demonstrated to be effective for enhancing CPP-GMR output, however, the spin-dependent transport is little known. In other words, the origin of the large CPP-GMR output with the Heusler alloys is not clear.

The purposes of this study are as follows:

(1) To obtain large CPP-GMR outputs using Heusler alloy magnetic layers.
(2) To clarify the spin-dependent scattering of the CPP-GMR with $Co_2Fe(Al_{0.5}Si_{0.5})$ Heusler alloy (CFAS) magnetic layers and a Ag spacer layer.
(3) To study the effect of the spacer layer for CPP-GMR devices with Heusler alloys, and to find a spacer layer material with a good band matching with Heusler alloys.

For these purposes, we have chosen the epitaxial structure deposited on a MgO single crystalline substrate for the devices. Although the epitaxial devices grown on the MgO substrate are far from real commercial devices, the high CPP-GMR has been little demonstrated for devices with poly crystalline films grown on non-single crystalline substrates, and the fabrication process has not been established. Thus, the well-established epitaxial devices grown on the MgO substrate is suitable for the fundamental experiments for the thesis works.

1.7 Outline of this thesis

This thesis contains seven chapters.

Chapter 1 describes the back ground of the research, the introduction of CPP-GMR and the applications, and the purpose of the research.

Chapter 2 reviews the theory of CPP-GMR briefly.

Chapter 3 describes the experimental methos and the procedures used in this work.

Chapter 4 describes experimental results of the fabrication and the characterization of $Co_2Fe(Al_{0.5}Si_{0.5})$ Heusler alloy (CFAS) films and the applications to exchange biased spin-valves and pseudo spin-valve with Ag spacer layers.

Chapter 5 is devoted to analyze the spin-dependent for the bulk and interfacial scattering in the CFAS/Ag/CFAS pseudo spin-valves.

Chapter 6 describes a work of CPP-GMR devices with a new spacer layer material NiAl B2 intermetallic compound in a view of the band matching.

Chapter 7 summarizes the results and discusses the perspectives of future works for further improvements CPP-GMR devices.

In Appendix, the future view of the CPP-GMR research toward technologies for ultrahigh magnetic recording is reviewed.

References

[1] Y. Shiroishi, K. Fukuda, I. Tagawa, H. Iwasaki, S. Tekenoiri, H. Tanaka, H. Mutoh, and N. Yoshikawa, IEEE. Trans. Magn. **45**, 3816 (2009).

[2] http://www.computerworld.jp/topics/datac/106849.html

[3] M. N. Baibichi, J. M. Broto, A. Fert, F. Nguyen Van Dau, F. Petroff, P. Eitenne, G. Creuzet, A. Friederich, and J. Chazelas, Phys. Rev. Lett. **61**, 2472 (1988).

[4] P. Grünberg, R. Schreiber, Y. Pang, M.B. Brodsky, H. Sowers, Phys. Rev. Lett. **57** (1986) 2442.

[5] N. F. Mott and H. Jones, *The Theory of the Properties of Metals and Alloys*, The Oxford University Press, (1936).

[6] I. A. Campbell, A. Fert, and A. R. Pomeroy, Phil. Mag. **15**, 977 (1967). A. Fert, and I. A. Campbell, Phys. Rev. Lett. **21**, 1190 (1968). A. Fert, and I. A. Campbell, J. Phys. F: Metal. Phys. **6**, 849 (1976).

[7] B. Dieny, V. S. Speriosu, S. S. P. Parkin, B. A. Gurney, D. R. Wilhoit, and D. Mauri, Phys. Rev. B **43**, 1297(R) (1991).

[8] D. E. Heim, R. E. Fontana, Jr., C. Tsang, V. S. Speriosu, B. A. Gurney, and M. L. Williams, IEEE. Trans. Magn. **30**, 316 (1994). C. Tsang, R. E. Fontana, T. Lin, D. E. Heim, V. S. Speriosu, B. A. Gurney, and M. L. Williams, IEEE. Trans. Magn. **30**, 3801 (1994).

[9] As review, Y. Ishiroishi, Magnetics Jpn. **5**, 312 (2010) (in Japanese).

[10] C. E. Moreau, I. C. Moraru, N. O. Birge, W. P. Pratt, Jr., Appl. Phys. Lett. **91**, 012101 (2007).

[11] T. Valet, and A. Fert, Phys. Rev. B **48**, 7099 (1993).

[12] S. S. P. Parkin, Phys. Rev. Lett. **71**, 1641 (1993).

[13] W. P. Pratt, Jr., S. –F. Lee, J. M. Slaughter, R. Loloee, P. A. Schroeder, and J. Bass, Phys. Rev. Lett. **66**, 3060 (1991).

[14] M. A. M. Gijs, S. K. J. Lencziwski, J. B. Glesbers, Phys. Rev. Lett. **70**, 3343 (1993).

[15] M. Takagishi, K. Koi, M. Yoshikawa, T. Funayama, H. Iwasaki, M. Sahashi, IEEE Trans. Magn. **38**, 2277 (2002).

[16] M. Takagishi, K. Yamada, H. Iwasaki, H. N. Fuke, and S. Hashimoto, IEEE Trans. Magn. **46**, 2086 (2010).

[17] Y. Nagamine, H. Maehara, K. Tsunekawa, D. D. D Djayaprawira, N. Watanabe, S. Yuasa, and K. Ando. Appl. Phys. Lett. **89**, 162507 (2006).

[18] J. R. Childress, M. J. Carey, M. -C. Cyrille, K. Carey, N. Smith, J. A. Katine, T. D. Boone, A. A. G. Driskill-Smith, S. Maat, K. Mackay, and C. H. Tsang, IEEE Trans. Magn. **42**, 2444 (2006).
[19] M. Covington, M. AlHajDarwish, Y. Ding, N. J. Gokemeijer, and M. A. Seigler, Phys. Rev. B **69**, 184406 (2004).
[20] J. –G. Zhu, N. Kim, Y. Zhou, Y. Zheng, J. Chang, J, Chang, K. Ju, X. Zhu, and R. M. White, IEEE Trans. Magn. **40**, 2323 (2004).
[21] S. I. Kiselev, J. C. Sankey, I. N. Krivorotov, N. C. Emley, R. J. Schoelkopf, R. A. Buhrman, and D. C. Ralph, Nature (London), **425**, 380 (2003).
[22] L. Zhang, A. Perumal, Y. K. Takahashi, K. Hono, B. C. Stipe, J. –Y. Juang, and M. Grobis, AF-01, 55th Annual Conference on Magnetism and Magnetic Materials, (2010), and J. Appl. Phys. (in press)
[23] J. –G. Zhu, X. Zhu, and Y. Tang, IEEE Trans. Magn. **44**, 125 (2008).
[24] Y. Nozaki, N. Narita, T. Tanaka, and K. Matsuyama, Appl. Phys. Lett. **95**, 082505 (2009).
[25] T. Yoshioka, T. Nozaki, T. Seki, M. Shiraishi, T. Shinjo, Y. Suzuki, and Y. Uehara, Appl. Phys. Express **3**, 013002 (2010).
[26] K. Yamada, M. Takagishi, K. Koi, and H. Iwasaki, DF-08, 55th Annual Conference on Magnetism and Magnetic Materials, (2010).
[27] J. –G. Zhu, and Y. Wang, IEEE Trans. Magn. **46**, 751 (2010).
[28] R. A. de Groot, F. M. Mueller, P. G. van Engen, abd K. H. J. Buschow, Phys. Rev. Lett. **50**, 2024 (1983).
[29] P. J. Webster, J. Phys. Chem. Solids **32**, 1221 (1971).
[30] R. Y. Umestu, K, Kobayashi, A. Fujita, R. Kainuma, and K. Ishida, Scripta Mater. **58**, 723 (2008).
[31] H. Kijima, T. Ishikawa, T. Marukame, H. Koyama, K. Matsuda, T. Uemura, and M. Yamamoto, IEEE Trans. Magn. **42**, 2688 (2006).
[32] S. Picozzi, A. Continenza, A. J. Freeman, Phys. Rev. B **66**, 094421 (2002).
[33] I. Galanakis, P. H. Dederichs, N. Papanikolaou, Phys. Rev. B 99, 174429 (2002).
[34] I. Galanakis, J. Phys.: Condens. Matter **16**, 3089 (2004).
[35] B. Balke, G. H. Fecher, H. C. Kandpal, C. Felser, K. Kobayashi, E. Ikenaga, J.–J. Kim, and S. Ueda, Phys. Rev. B **74**, 104405 (2006).
[36] S. Picozzi, A. Continenza, A. J. Freeman, Phys. Rev. B **69**, 094423 (2004).
[37] N. Tezuka, N. Ikeda, A. Miyazaki, S. Sugimoto, M. Kikuchi, and K. Inomata, Appl. Phys. Lett. **89**, 112514 (2006). N. Tezuka, N. Ikeda, S. Sugimoto, and K. Inomata,

Appl. Phys. Lett. **89**, 252508 (2006). G. H. Fecher, and C. Felser, J. Phys. D: Appl. Phys. **40** 1582 (2007). T. M. Nakatani, A. Rajanikanth, Z. Gercsi, Y. K. Takahashi, K. Inomata, and K. Hono, J. Appl. Phys. **102**, 033916 (2007). R. Shan, H. Sukegawa, W. H. Wang, M. Kodzuka, T. Furubayashi, T. Ohkubo, S. Mitani, K. Inomata, and K. Hono, Phys. Rev. Lett. **102**, 246601 (2009). and other papers from their groups.

[38] K. Inomata, S. Okamura, R. Goto, and N. Tezuka, Jpn. J. Appl. Phys. **42**, L419 (2003).

[39] Y. Sakuraba, J. Nakata, M. Oogane, H. Kubota, Y. Ando, A. Sakuma, and T. Miyazaki, Jpn. J. Appl. Phys. **44**, L1100 (2005).

[40] Y. Sakuraba, M. Hattori, M. Oogane, Y. Ando, H. Kato, A. Sakuma, T. Miyazaki, and H. Kubota, Appl. Phys. Lett. **88**, 192508 (2006).

[41] Y. Sakuraba, T. Miyakoshi, M. Oogane, Y. Ando, A. Sakuma, T. Miyazaki, and H. Kubota, Appl. Phys. Lett. **89**, 052508 (2006).

[42] T. Ishikawa, N. Itabashi, T. Taira, K.-i Matsuda, T. Uemura, and M. Yamamoto, Appl. Phys. Lett. **94**, 092503 (2009).

[43] A. Sakuma, Y. Toga, and H. Tsuchiura. J. Appl. Phys. **105**, 07C910 (2009).

[44] N. Hasegawa, Koike, K. Ikarashi, M. Ishizone, M. Kawamura, Y. Nakazawa, A. Takahashi, H. Tomita, H. Iwasaki, and M. Sahashi, J. Appl. Phys. **91**, 8774 (2002).

[45] H. Fukuzawa, H. Yuasa, S. Hashimoto, K. Koi, H. Iwasaki, M. Takagishi, Y. Tanaka, M. Sahashi, IEEE Trans. Magn. **40**, 2236 (2004).

[46] H. Yuasa, M. Hara, S. Murakami, Y. Fuji, H. Fukuzawa, K. Zhang, M. Li, E. Schreck, P. Wang, M. Chen, Appl. Phys. Lett. **97**, 112501 (2010).

[47] H. Yuasa, M. Hara, H. Fukuzawa, Appl. Phys. Lett. **92**, 262509 (2008).

[48] H. Katada, K. Nakamoto, H. Hoshiya, K. Hoshino, N. Yoshida, M. Shiimoto, Y. Sato, H. Takazawa, K. Yasui, M. Hatatani, K. Watanabe, Y. Ikeda, K. Meguro, J. Magn. Magn, Mater. **320**, 2975 (2008).

[49] X. Peng, P. Kolbo, K. Nikolaev, S. Chen, Z. Wang, T. Boonstra, P. Anderson, S. Kalderon, P. Czoschke, A. Morrone, D. Dimtrov, S. Xue, Y. Chen, J. Magn. Magn, Mater. **321**, 1889 (2009).

[50] Y. Nagamine, H. Maehara, K. Tsunekawa, D. D. Djayaprawira, N. Watanabe, S. Yuasa, and K. Ando, Appl. Phys. Lett. **89**, 162507 (2006).

[51] J. A. Caballero, A. C. Reilly, Y. Hao, J. Bass, W. P. Pratt, Jr., F. Petroff, J. R. Childress, J. Magn. Magn. Mater. **198-199**, 55 (1999).

[52] H. Hoshiya, K. Hoshino, J. Appl. Phys. **95**, 6774 (2004).

[53] K. Yakushiji, K. Saito, S. Mitani, K. Takanashi, Y. K. Takahashi, K. Hono, Appl. Phys. Lett. **88**, 222504 (2006).
[54] J. R. Childress, M. J. Carey, S. Maat, N. Smith, R. E. Fontana, D. Druist, K. Carey, J. A. Katine, N. Robertson, T. D. Boone, M. Alex, J. Moore, and C. H. Tsang, T. D. Boone, M. Alex, J. Moore, and C. H. Tsang, IEEE Tran. Magn. **44**, 90 (2008).
[55] L. J. Singh, C. W. Leung, C. Bell, J. L. Prieto, Z. H. Barber, J. Appl. Phys. **100** (2006) 013910.
[56] K. Nikolaev, P. Anderson, P. Kolbo, D. Dimitrov, S. Xue, X. Peng, T. Pokhil, H. Cho, Y. Chen, J. Appl. Phys. **103**, 17F553 (2008).
[57] T. Furubayashi, K. Kodama, H. Sukegawa, Y. K. Takahashi, K. Inomata, and K. Hono, Appl. Phys. Lett. **93**, 122507 (2008).
[58] T. Mizuno, Y. Tsuchiya, T. Machita, S. Hara, D. Miyauchi, K. Shimazawa, T. Chou, K. Noguchi, and K. Tagami, IEEE Tran. Magn. **44**, 3584 (2008).
[59] Y. Sakuraba, T. Iwase, K. Saito, S. Mitani, and K. Takanashi, Appl. Phys. Lett. **94**, 012511 (2009).
[60] K. Kodama, T. Furubayashi, H. Sukegawa, T. M. Nakatani, K. Inomata, K. Hono, J. Appl. Phys. **105**, 07E905 (2009).
[61] T. Iwase, Y. Sakuraba, S. Bosu, K. Saito, S. Mitani, and K. Takanashi, Appl. Phys. Express **2**, 063003 (2009).
[62] K. Nikolaev, P. Kolbo, T. Pokhil, X. Peng, Y. Chen, T. Ambrose, O. Mryasov, Appl. Phys. Lett. **94**, 222501 (2009).
[63] T. M. Nakatani, T. Furubayashi, S. Kasai, H. Sukegawa, Y. K. Takahashi, S. Mitani, and K. Hono, Appl. Phys. Lett. **96**, 212501 (2010).
[64] T. Furubayashi, K. Kodama, T. M. Nakatani, H. Sukegawa, Y. K. Takahashi, K. Inomata, K. Hono, J. Appl. Phys. **107**, 113917 (2010).
[65] Y. Sakuraba, K. Izumi, T. Iwase, S. Bosu, K. Saito, K. Takanashi, Y. Miura, K. Futatsukawa, K. Abe, M. Shirai, Phys. Rev. B **82**, 094444 (2010).
[66] N. Hase, B. S. D. Ch. S. Varaprasad, T. M. Nakatani, H. Sukegawa, S. Kasai, Y. K. Takahashi, T. Furubayashi, K. Hono, J. Appl. Phys. **108**, 093916 (2010).
[67] H. S. Goripati, T. Furubayashi, S. V. Karthik, T.M. Nakatani, Y. K. Takahashi, K. Hono, J. Appl. Phys. (2011) in press.
[68] T. Mano, I. C. Chu, K. Miyake, M. Doi, S. Kuwano, T. Shima, and M. Sahashi, IEEE Trans. Magn. **45**, 3460 (2009).
[69] J. Bass, and W. P. Pratt, Jr., J. Phys.: Condens. Matter **19**, 183201 (2007).
[70] H. Yuasa, M. Yoshikawa, Y. Kamiguchi, K. Koi, H. Iwasaki, M. Takagishi, and M.

Sahashi, J. Appl. Phys. **92**, 2646 (2002).
[71] H. Oshima, K. Nagasaka, Y. Seyama, Y. Shimizu, S. Eguchi, and A. Tanaka, J. Appl. Phys. **91**, 8105 (2002)
[72] S. Maat, M. J. Carey, and J. R. Childress, J. Appl. Phys. **101**, 093905 (2007). *ibid.* **102**, 049902 (2007).
[73] A. Jogo, K. Nagasaka, T. Ibusuki, Y. Shimizu, A. Tanaka, and H. Oshima, J. Magn. Magn. Mater. **309**, 80 (2007).
[74] S. Maat, M. J. Carey, and J. R. Childress, Appl. Phys. Lett. **93**, 143505 (2008).

Chapter 2 Theory of CPP-GMR

2.1 Spin accumulation at F/N junction

Let us consider a heterostructures between a ferromagnetic layer (F) and a nonmagnetic layer (N). At a position in the F layer which is sufficiently far from the F/N interface, the current is spin-polarized with the own spin polarization. One the other hand, in the bulk of the N layer far from the interface, the non-spin polarized current is the equilibrium state. Therefore, there has to be an adjustment of the spin polarization around the interface, which induces deviations of the electrochemical potentials (ECP) between the up spin and the down spin from the equilibria. This is called *spin accumulation*. The spin accumulation relaxes with the distance from the F/N interface. The characteristic length of the spin relaxation is the spin diffusion length of the material. The distribution of the ECP by the spin accumulation is described by the diffusion equation [1][2].

The electric current densities carried by the up and down spin electrons are given by the Ohm's equation. In one dimension,

$$\mathbf{j}_s = -\frac{\sigma_s}{e}\nabla\mu_s, \tag{2.1}$$

where the subscript s represents the spin direction, e is the electronic charge, σ is the conductivity, and μ is the electrochemical potential.

The current has to satisfy the continuity equations for the charge and spin currents. *i.e.*

$$\nabla\cdot(\mathbf{j}_\uparrow + \mathbf{j}_\downarrow) = 0, \tag{2.2}$$

$$\nabla\cdot(\mathbf{j}_\uparrow - \mathbf{j}_\downarrow) = -e\frac{\delta n_\uparrow}{\tau_{\uparrow\downarrow}} + e\frac{\delta n_\downarrow}{\tau_{\downarrow\uparrow}}, \tag{2.3}$$

where δn_s is the deviation of the carrier density of the spin s from the equilibrium, and $\tau_{ss'}$ is the spin flip relaxation time from one spin s to the other spin s'. In the steady state,

$\tau_{ss'}$ satisfies $N_{\uparrow} / \tau_{\uparrow\downarrow} = N_{\downarrow} / \tau_{\downarrow\uparrow}$, where N_s is the density of state of the spin s. Thus (2.3) indicates a creation of the spin current by spin flip from the up state to the down sate. Equations (2.1)–(2.3) give basic equations for the ECP,

$$\nabla^2(\sigma_{\uparrow}\mu_{\uparrow} + \sigma_{\downarrow}\mu_{\downarrow}) = 0 \tag{2.4}$$

$$\nabla^2(\mu_{\uparrow} - \mu_{\downarrow}) = \frac{1}{\ell_{\mathrm{sf}}^2}(\mu_{\uparrow} - \mu_{\downarrow}), \tag{2.5}$$

where ℓ_{sf} is the spin diffusion length $\ell_{\mathrm{sf}} = \sqrt{D\tau_{\mathrm{sf}}}$ with the spin relaxation time and the diffusion constant D:

$$\frac{1}{\tau_{\mathrm{sf}}} = \frac{1}{2}\left(\frac{1}{\tau_{\uparrow\downarrow}} + \frac{1}{\tau_{\downarrow\uparrow}}\right), \tag{2.6}$$

$$D = \frac{D_{\uparrow}D_{\uparrow}(N_{\uparrow} + N_{\downarrow})}{N_{\uparrow}D_{\uparrow} + N_{\downarrow}D_{\uparrow}} \tag{2.7}$$

In one dimension system, the general solution of μ_s by Eqs. (2.4), (2.5) is given by [3]

$$\mu_s(x) = Ax + B + C\exp(x/\ell_{\mathrm{sf}}) + D\exp(-x/\ell_{\mathrm{sf}}). \tag{2.8}$$

The first two terms the steady state μ_0 under the applied bias voltage, and the last two terms represent the distribution of the spin accumulation $\Delta\mu_s$. The constants A, B, C and D are given by the boundary conditions for the charge currents and the ECPs for each spin. For example, in the case that there is neither a spin flipping nor an interfacial resistant at the F/M interface, both the charge current and electrochemical potential have to be continuous at the F/N interface. Figure 2-1 shows the distribution of the ECPs in this boundary condition. Although $\mu_s(x)$ is continuous at $x = 0$ for both spins, a discontinuity of μ_0 is formed at the interface, corresponding to a boundary resistance by the spin accumulation given by

$$\Delta R = \frac{\beta^2 \ell_{\mathrm{sf}}^{\mathrm{F}} \ell_{\mathrm{sf}}^{\mathrm{N}}}{A(\ell_{\mathrm{sf}}^{\mathrm{N}}\sigma_{\mathrm{F}} + (1-\beta^2)\ell_{\mathrm{sf}}^{\mathrm{F}}\sigma_{\mathrm{N}})} = \beta^2 \frac{r_{\mathrm{F}} r_{\mathrm{N}}}{r_{\mathrm{F}} + r_{\mathrm{N}}}, \tag{2.9}$$

where A is the area of the FM/NM junction, r_{F} and r_{N} are called *spin resistances* defined by

$$r_{\mathrm{F}} = \frac{\ell_{\mathrm{sf}}^{\mathrm{F}}}{A(1-\beta^2)\sigma_{\mathrm{F}}}, \quad r_{\mathrm{F}} = \frac{\ell_{\mathrm{sf}}^{\mathrm{N}}}{A\sigma_{\mathrm{N}}}. \tag{2.10}$$

Note that the boundary resistance by the spin accumulation (or called *spin-coupled*

interface resistance in the Valet and Fert's paper [3]) is different from the interfacial resistance between two materials derived from band structure mismatching or of the lattice mismatching. The boundary resistance is purely a product of the spin accumulation. The distribution of the ECPs with the interfacial spin-dependent resistance is shown in Fig. 2-2. Here, the boundary condition at the F/N interface is $\mu_s(x=-0)-\mu_s(x=+0)=R^s_{\mathrm{F/N}}$, where $R^s_{\mathrm{F/N}}$ is the interfacial resistance for the spin *s*. Due to these boundary conditions, the ECPs are no longer continuous at the F/N interface. When $AR^{\uparrow}_{\mathrm{F/N}} \neq AR^{\downarrow}_{\mathrm{F/N}}$, the interfacial scattering has a spin asymmetry. The interfacial scattering spin symmetry γ is defined by

$$\gamma = \frac{R^{\downarrow}_{\mathrm{F/N}} - R^{\uparrow}_{\mathrm{F/N}}}{R^{\uparrow}_{\mathrm{F/N}} + R^{\downarrow}_{\mathrm{F/N}}}, \tag{2.11}$$

As seen from Fig. 2-2, the spin asymmetry of the interfacial resistance makes the boundary resistance by the spin accumulation ΔR larger than that without the interfacial resistance (Fig. 2-1).

In F/N/F trilayer, the boundary resistance ΔR at each F/N interface is weakened each other in the parallel magnetization configuration between the two F layers. On the other hand, they are enhanced in the antiparallel magnetization configuration. Therefore, a change in the resistance of F/N/F trilayer between the parallel and antiparallel magnetization states is observed. This is the current-perpendicular-to-plane giant magnetoresistance (CPP-GMR).

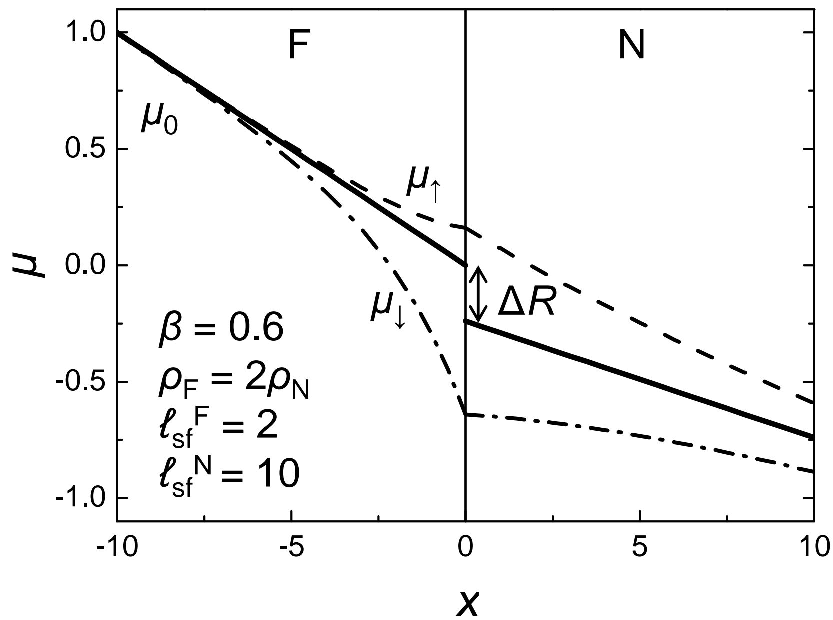

Fig. 2-1 Distribution of the electrochemical potential μ of the up and down spins at an F/N interface. There is no interfacial resistance. μ and position x are in arbitrary unit. The spin diffusion length of the F layer is 1/5 of that in the N layer.

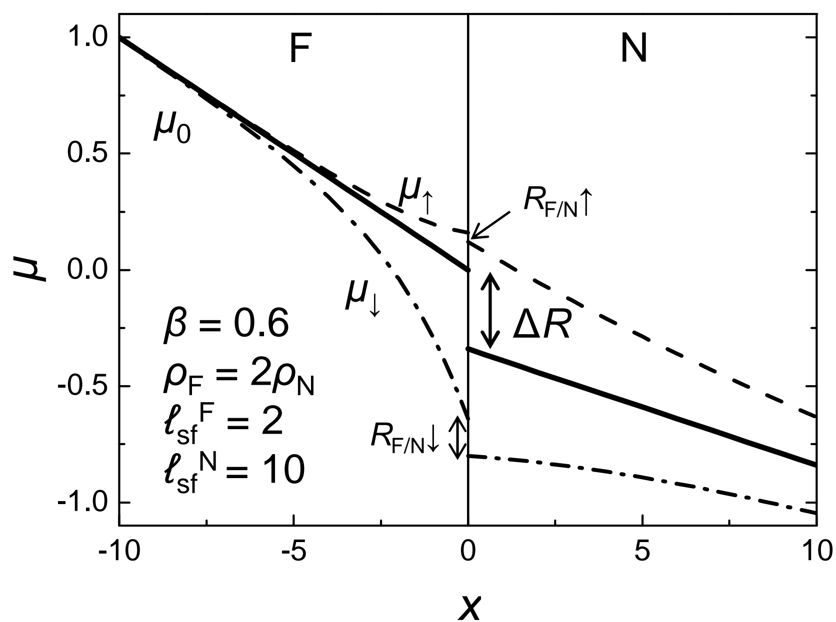

Fig. 2-2 Distribution of the electrochemical potential μ with a spin-dependent interfacial resistance.

2.2 Valet-Fert model

2.2.1 Parallel resister model without spin relaxation

First, we define $\rho_\uparrow$, $\rho_\downarrow$ and $AR_{\mathrm{F/N}}{}^\uparrow$, $AR_{\mathrm{F/N}}{}^\downarrow$ as the resistivities and the F/N interfacial resistance-area products of the up and down spins, respectively. Then, the resistivity we can measure ρ is the total resistance of the parallel circuit composed of the up and down spin channels. Thus,

$$\rho = \left(\frac{1}{\rho_\uparrow} + \frac{1}{\rho_\downarrow}\right) = \frac{\rho_\uparrow \rho_\downarrow}{\rho_\uparrow + \rho_\downarrow}. \quad (2.12)$$

The interfacial resistance is also given by the similar expression with $AR_{\mathrm{F/N}}{}^\uparrow$ and $AR_{\mathrm{F/N}}{}^\downarrow$. Next, we define the spin asymmetries of scattering in the bulk and at the interface, respectively.

$$\beta = \frac{\sigma_\uparrow - \sigma_\downarrow}{\sigma_\uparrow + \sigma_\downarrow} = \frac{\rho_\downarrow - \rho_\uparrow}{\rho_\uparrow + \rho_\downarrow} \quad (2.13)$$

$$\gamma = \frac{AR_{\mathrm{F/N}}{}^\downarrow - AR_{\mathrm{F/N}}{}^\uparrow}{AR_{\mathrm{F/N}}{}^\uparrow + AR_{\mathrm{F/N}}{}^\downarrow}, \quad (2.14)$$

where σ is the conductively ($\sigma = 1/\rho$)It is convenient to define the expanded resistivity ρ^* and interfacial resistance $AR_{\mathrm{F/N}}{}^*$ by

$$\rho^* = \rho/(1-\beta^2) \quad , \quad (2.15)$$

$$AR^*_{\mathrm{F/N}} = AR_{\mathrm{F/N}} / (1-\gamma^2) \quad . \quad (2.16)$$

Then, the resistivity of the interfacial resistance of each spin are represented as

$$\rho_{\uparrow(\downarrow)} = 2\rho^*[1-(+)\beta], \quad (2.17)$$

$$AR_{\mathrm{F/N}}{}^{\uparrow(\downarrow)} = 2AR^*_{\mathrm{F/N}}[1-(+)\gamma]. \quad (2.18)$$

For nonmagnetic materials, $\rho_{\mathrm{N}\uparrow} = \rho_{\mathrm{N}\downarrow}$, thus $\beta = 0$ and $\rho_{\mathrm{N}}{}^* = \rho_{\mathrm{N}}$. For ferromagnetic materials, generally $\rho_{\mathrm{F}\uparrow} < \rho_{\mathrm{F}\downarrow}$, thus $\beta > 0$. The notations of the extended resistivity ρ^* and interfacial resistance $AR_{\mathrm{F/N}}{}^*$ are convenient to consider the two current circuit.

We assume that there is no spin relaxation through the F/N multilayer of our interest, so that the electric transport can be treated as the parallel resister circuit composed of the up and down spin channels as Fig. 2-3. For F/N/F trilayer, the expression of ΔRA can be obtained by solving the total resistances of the circuits as,

$$\Delta RA = \frac{4(\beta\rho_{\mathrm{F}}{}^{*}t_{\mathrm{F}} + \gamma AR^{*}{}_{\mathrm{F/N}})^2}{2\rho_{\mathrm{F}}{}^{*}t_{\mathrm{F}} + \rho_{\mathrm{N}}t_{\mathrm{N}} + 2AR^{*}{}_{\mathrm{F/N}}} \tag{2.19}$$

More roughly, ΔRA is given by as follows.

$$\begin{aligned}\Delta RA &\sim 2\beta^2\rho_{\mathrm{F}}^{*}t_{\mathrm{F}} + 2\gamma^2 AR_{\mathrm{F/N}}^{*} \\ &= 2\frac{\beta^2}{1-\beta^2}\rho_{\mathrm{F}}t_{\mathrm{F}} + 2\frac{\gamma^2}{1-\gamma^2}AR_{\mathrm{F/N}}\end{aligned} \tag{2.20}$$

This is similar to the Julliere's equation for tunnel magnetoresistance of TMR = $P_1P_2/(1- P_1P_2)$, where P1 and P2 are the spin polarizations of the electrode 1 and 2, respectively. However, the physical factor contributing to CPP-GMR is not only the spin polarization terms (β and γ), but also the resistance terms (ρ_{F} and $AR_{\mathrm{F/N}}$) Therefore, the F materials with large β and high ρ_{F} or the F/N interfaces with large γ and $AR_{\mathrm{F/N}}$ are the keys to obtain large CPP-GMR outputs.

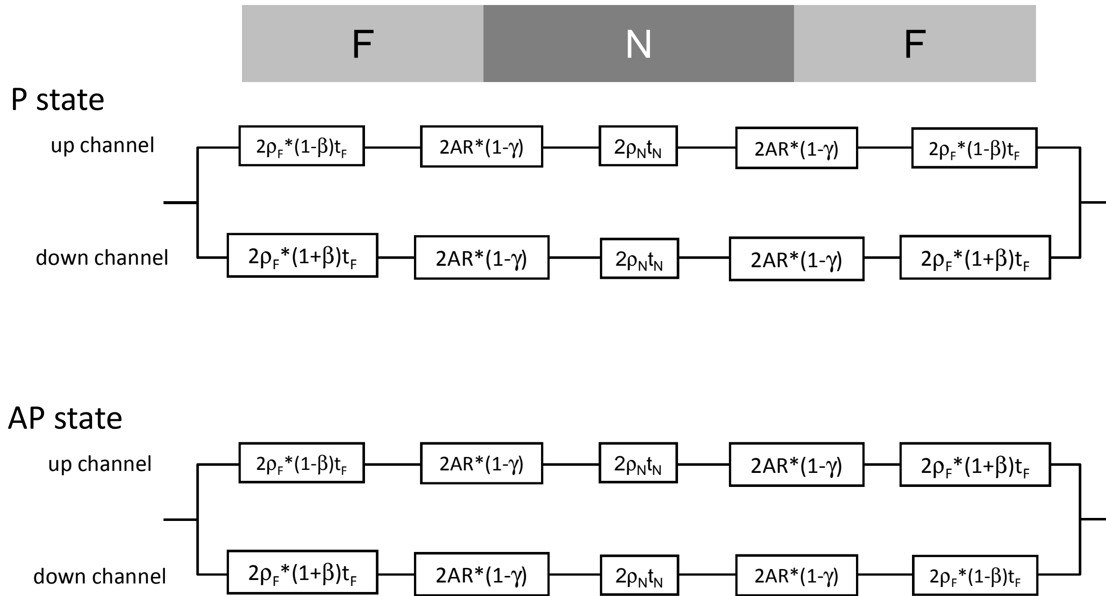

Fig. 2-3 Parallel resistance circuits by the two current model for F/N/F trilayer.

2.2.2 General equation of Δ*RA*

Valet and Fert rigorously solved the diffusion equation under the periodic boundary condition of F/N multilayer with the period of *M*. The *RA* of the parallel magnetization state (P) and antiparallel magnetization state (AP) are given by

$$RA^{\mathrm{P,AP}} = M\,(RA_0 + 2RA_{\mathrm{SI}}^{\mathrm{P,AP}})$$

$$\text{with } RA_0 = \rho_{\mathrm{F}} t_{\mathrm{F}} + \rho_{\mathrm{N}} t_{\mathrm{N}} + 2AR_{\mathrm{F/N}}, \qquad (2.21)$$

where $RA_{\mathrm{SI}}^{\mathrm{P}}$ and $RA_{\mathrm{SI}}^{\mathrm{AP}}$ are the boundary resistances formed by the spin accumulation in the P and AP state (spin-coupled interface resistance in the Valet–Fert paper [3]). These are given by

$$RA_{\mathrm{SI}}^{\mathrm{P}} = \frac{\dfrac{(\beta-\gamma)^2}{\rho_{\mathrm{N}}\ell_{\mathrm{sf}}^{\mathrm{N}}}\coth\left(\dfrac{t_{\mathrm{N}}}{2\ell_{\mathrm{sf}}^{\mathrm{N}}}\right)+\dfrac{\gamma^2}{\rho_{\mathrm{F}}^{*}\ell_{\mathrm{sf}}^{\mathrm{F}}}\coth\left(\dfrac{t_{\mathrm{F}}}{2\ell_{\mathrm{sf}}^{\mathrm{F}}}\right)+\dfrac{\beta^2}{AR_{\mathrm{F/N}}^{*}}}{\dfrac{1}{\rho_{\mathrm{N}}\ell_{\mathrm{sf}}^{\mathrm{N}}}\coth\left(\dfrac{t_{\mathrm{N}}}{2\ell_{\mathrm{sf}}^{\mathrm{N}}}\right)\dfrac{1}{\rho_{\mathrm{F}}^{*}\ell_{\mathrm{sf}}^{\mathrm{F}}}\coth\left(\dfrac{t_{\mathrm{F}}}{2\ell_{\mathrm{sf}}^{\mathrm{F}}}\right)+\dfrac{1}{AR_{\mathrm{F/N}}^{*}}\left[\dfrac{1}{\rho_{\mathrm{N}}\ell_{\mathrm{sf}}^{\mathrm{N}}}\coth\left(\dfrac{t_{\mathrm{N}}}{2\ell_{\mathrm{sf}}^{\mathrm{N}}}\right)+\dfrac{1}{\rho_{\mathrm{F}}^{*}\ell_{\mathrm{sf}}^{\mathrm{F}}}\coth\left(\dfrac{t_{\mathrm{F}}}{2\ell_{\mathrm{sf}}^{\mathrm{F}}}\right)\right]}, \qquad (2.22)$$

$$RA_{\mathrm{SI}}^{\mathrm{AP}} = \frac{\dfrac{(\beta-\gamma)^2}{\rho_{\mathrm{N}}\ell_{\mathrm{sf}}^{\mathrm{N}}}\tanh\left(\dfrac{t_{\mathrm{N}}}{2\ell_{\mathrm{sf}}^{\mathrm{N}}}\right)+\dfrac{\gamma^2}{\rho_{\mathrm{F}}^{*}\ell_{\mathrm{sf}}^{\mathrm{F}}}\coth\left(\dfrac{t_{\mathrm{F}}}{2\ell_{\mathrm{sf}}^{\mathrm{F}}}\right)+\dfrac{\beta^2}{AR_{\mathrm{F/N}}^{*}}}{\dfrac{1}{\rho_{\mathrm{N}}\ell_{\mathrm{sf}}^{\mathrm{N}}}\tanh\left(\dfrac{t_{\mathrm{N}}}{2\ell_{\mathrm{sf}}^{\mathrm{N}}}\right)\dfrac{1}{\rho_{\mathrm{F}}^{*}\ell_{\mathrm{sf}}^{\mathrm{F}}}\coth\left(\dfrac{t_{\mathrm{F}}}{2\ell_{\mathrm{sf}}^{\mathrm{F}}}\right)+\dfrac{1}{AR_{\mathrm{F/N}}^{*}}\left[\dfrac{1}{\rho_{\mathrm{N}}\ell_{\mathrm{sf}}^{\mathrm{N}}}\tanh\left(\dfrac{t_{\mathrm{N}}}{2\ell_{\mathrm{sf}}^{\mathrm{N}}}\right)+\dfrac{1}{\rho_{\mathrm{F}}^{*}\ell_{\mathrm{sf}}^{\mathrm{F}}}\coth\left(\dfrac{t_{\mathrm{F}}}{2\ell_{\mathrm{sf}}^{\mathrm{F}}}\right)\right]}. \qquad (2.23)$$

Therefore,

$$\Delta RA = 2M\left(RA_{\mathrm{SI}}^{\mathrm{AP}} - RA_{\mathrm{SI}}^{\mathrm{P}}\right) \quad . \qquad (2.24)$$

In Figs. 2-4 and 2-5, $RA_{\mathrm{SI}}^{\mathrm{P}}$ and $RA_{\mathrm{SI}}^{\mathrm{AP}}$ plotted as a function of t_{F} for various values of β and γ, respectively. The values of is much smaller that of $RA_{\mathrm{SI}}^{\mathrm{AP}}$. This is because the spin accumulations at the F/N interfaces are weakened in the P state, whereas they are enhanced in the AP state.

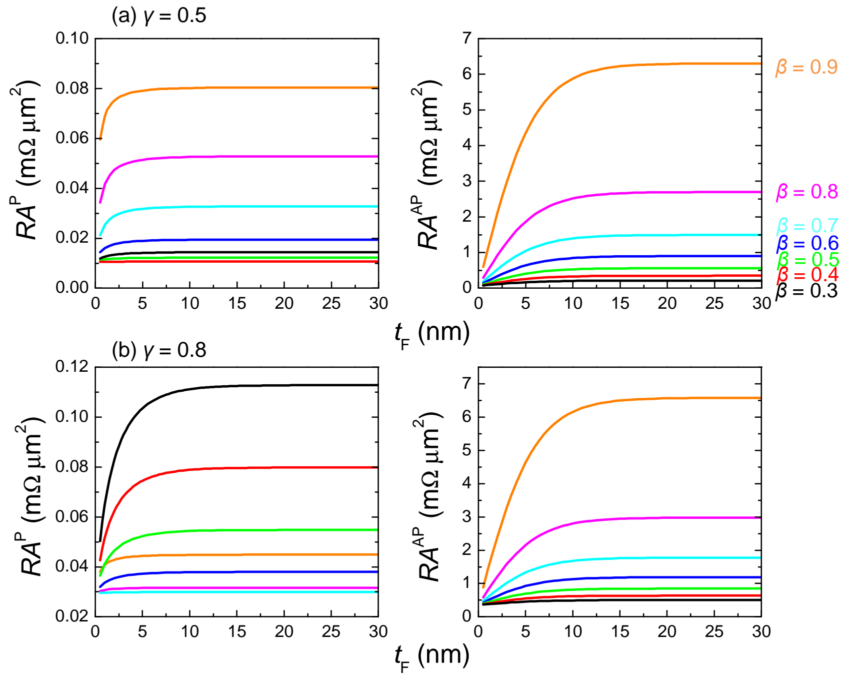

Fig. 2-4 RA_{SI} of parallel (P) and antiparallel (AP) states for various values of the bulk scattering spin asymmetry β with constant interfacial scattering spin asymmetry of (a) $\gamma = 0.5$ and (b) $\gamma = 0.8$. For all, ℓ_{sf}^{N} = 200 nm and ℓ_{sf}^{F} = 3 nm.

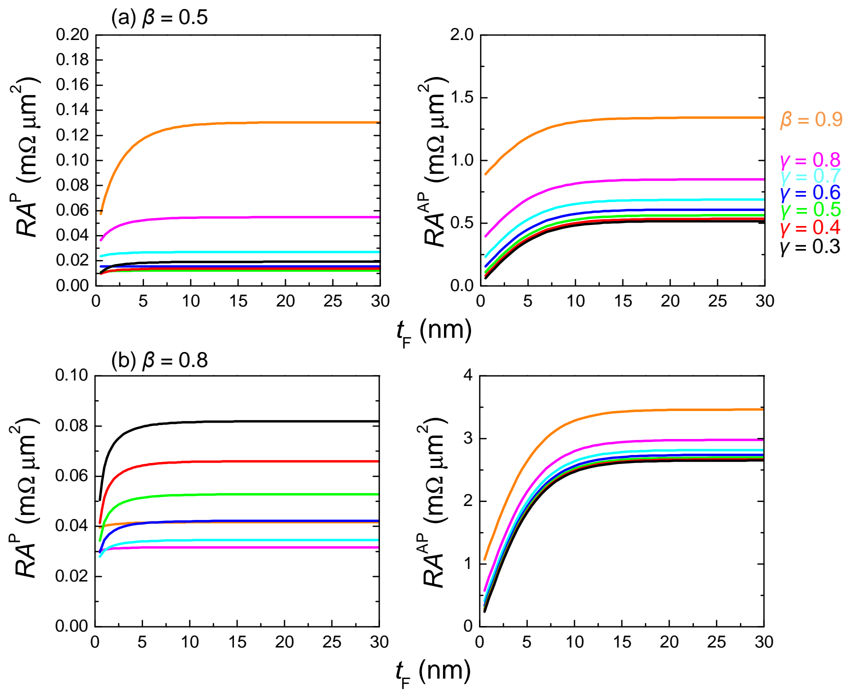

Fig. 2-5 RA_{SI} of parallel (P) and antiparallel (AP) states for various values of the interfacial scattering spin asymmetry γ with constant bulk scattering spin asymmetry of (a) $\beta = 0.5$ and (b) $\beta = 0.8$. For all, ℓ_{sf}^{N} = 200 nm and ℓ_{sf}^{F} = 3 nm.

Pseudo spin-valve is composed of an F/N/F trilayer connected with nonmagnetic lead electrode as schematically shown in Fig. 2-6. Here, the period of F/N bilayer M is 2, thus Eq. (2.23) becomes

$$\Delta RA = 4\left(RA_{\rm SI}^{\rm AP} - RA_{\rm SI}^{\rm P}\right). \qquad (2.25)$$

The coefficient 4 is derived from the four F/N interface: the two interfaces are with the spacer layer and the other two are with the lead electrodes.

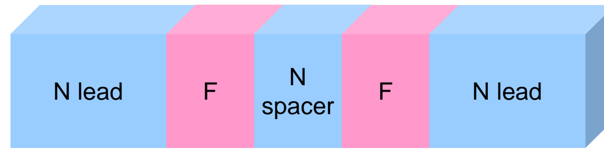

Fig. 2-6 Schematic N-lead/F/N spacer/F/N-lead five layer system (pseudo spin-valve).

When the spin diffusion length of the material of the spacer layer is much longer than the layer thickness ($\ell_{\rm sf}^{\rm N} \gg t_{\rm N}$), (2.12) and (2.13) can be reduced to

$$RA_{\rm SI}^{\rm P} = \frac{\dfrac{2(\beta-\gamma)^2}{\rho_{\rm N} t_{\rm N}} + \dfrac{\gamma^2}{\rho_{\rm F}^* \ell_{\rm sf}^{\rm F}} \coth\left(\dfrac{t_{\rm F}}{2\ell_{\rm sf}^{\rm F}}\right) + \dfrac{\beta^2}{AR_{\rm F/N}^*}}{\dfrac{2}{\rho_N t_N}\dfrac{1}{\rho_F \ell_{sf}^F}\coth\left(\dfrac{t_{\rm F}}{2\ell_{\rm sf}^{\rm F}}\right) + \dfrac{1}{AR_{\rm F/N}^*}\left[\dfrac{2}{\rho_{\rm N} t_{\rm N}} + \dfrac{1}{\rho_{\rm F}\ell_{\rm sf}^{\rm F}}\coth\left(\dfrac{t_{\rm F}}{2\ell_{\rm sf}^{\rm F}}\right)\right]}, \qquad (2.26)$$

$$RA_{\rm SI}^{\rm AP} = \frac{\dfrac{\gamma^2}{\rho_{\rm F}^* \ell_{\rm sf}^{\rm F}} \coth\left(\dfrac{t_{\rm F}}{2\ell_{\rm sf}^{\rm F}}\right) + \dfrac{\beta^2}{AR_{\rm F/N}^*}}{\dfrac{1}{AR_{\rm F/N}^*}\dfrac{1}{\rho_{\rm F}^* \ell_{\rm sf}^{\rm F}}\coth\left(\dfrac{t_{\rm F}}{2\ell_{\rm sf}^{\rm F}}\right)}, \qquad (2.27)$$

because, $\coth(x) \approx 1/x$ and $\tanh(x) \approx x$ when $x = \dfrac{t_{\rm N}}{2\ell_{\rm sf}^{\rm N}} \ll 1$.

In Fig. 2-7, ΔRA as a function of $t_{\rm F}$ for pseudo spin-valve ($M = 2$) are plotted by the general equation (Eqs. (2.22) and (2.23)) and by the approximated equation for $\ell_{\rm sf}^{\rm N} \gg t_{\rm N}$ (Eqs. (2.26) and (2.27)) for the different $\ell_{\rm sf}^{\rm N}$. Here, the other physical parameters are fixed to $\beta = 0.8$, $\gamma = 0.8$, $t_{\rm N} = 5$ nm, $\rho_{\rm N} = 2$ μΩcm, $\rho_{\rm F} = 50$ μΩcm, and $AR_{\rm F/N} = 0.25$ mΩμm^2. For $\ell_{\rm sf}^{\rm N} = 50$ nm ($\ell_{\rm sf}^{\rm N} = 10 t_{\rm N}$), the deviation between the general

and the approximated equations is significantly large. Thus, using the approximated equation will lead to an underestimation of the bulk spin asymmetry because the spin relaxation in the spacer layer is not considered. On the other hand, for $\ell_{\mathrm{sf}}^{\mathrm{N}}$ = 200 nm ($\ell_{\mathrm{sf}}^{\mathrm{N}} = 40t_{\mathrm{N}}$), the approximated equation gives almost the same value of ΔRA as that obtained by the general equation. The spin diffusion lengths of Ag and Cu have been reported to be hundreds nm even at room temperature. Thus, the approximated equation for $\ell_{\mathrm{sf}}^{\mathrm{N}} \gg t_{\mathrm{N}}$ should give sufficiently accurate interpretations of the scattering spin asymmetries for the CPP-GMR devices with the Ag or Cu spacer layers.

Note that the equation of ΔRA for spin-valves obtained by approximating that $\ell_{\mathrm{sf}}^{\mathrm{N}} \gg t_{\mathrm{N}}$ and $\ell_{\mathrm{sf}}^{\mathrm{F}} \gg t_{\mathrm{F}}$ in the general equation ((2.21), (2.22), and (2.24)) is different from Eq. (2.18) obtained by solving the parallel resistance circuit, but

$$\Delta RA = \frac{4(\beta\rho_{\mathrm{F}}^{*}t_{\mathrm{F}} + 2\gamma AR^{*}_{\mathrm{F/N}})^2}{2\rho_{\mathrm{F}}^{*}t_{\mathrm{F}} + \rho_{\mathrm{N}}t_{\mathrm{N}} + 4AR^{*}_{\mathrm{F/N}}}. \qquad (2.28)$$

$$\approx 2\beta^2\rho_{\mathrm{F}}^{*}t + 4\gamma^2 AR^{*}_{\mathrm{F/N}}$$

The coefficients are different. This is because the general questions of the Valet-Fert model are obtained under the boundary condition of the periodic M multilayers. The spin accumulation at the two interfaces between the FM layers and the N leads also contribute to the CPP-GMR. Equations (2.24) and (2.27) are plotted in Fig. 2-8 for $\ell_{\mathrm{sf}}^{\mathrm{F}} = 5$ nm.

[Note] Taniguchi and Imamura recently developed an equation of ΔRA by solving the diffusion equation for a N-lead/F/N/F/N-lead five-layer system (same as pseudo spin-valves) without assuming the periodic boundary condition [5]. They found that the spin accumulations at the interfaces with the spacer layer are more significant than those at the interfaces with the lead electrodes. Thus, the equation by Valet and Fert gives underestimated values for the bulk and interfacial scattering asymmetries because the contributions of the spin accumulations are regarded to be same for all of the interfaces in the model. The fitting by the Taniguchi–Imamura model is described in 5.4.2.

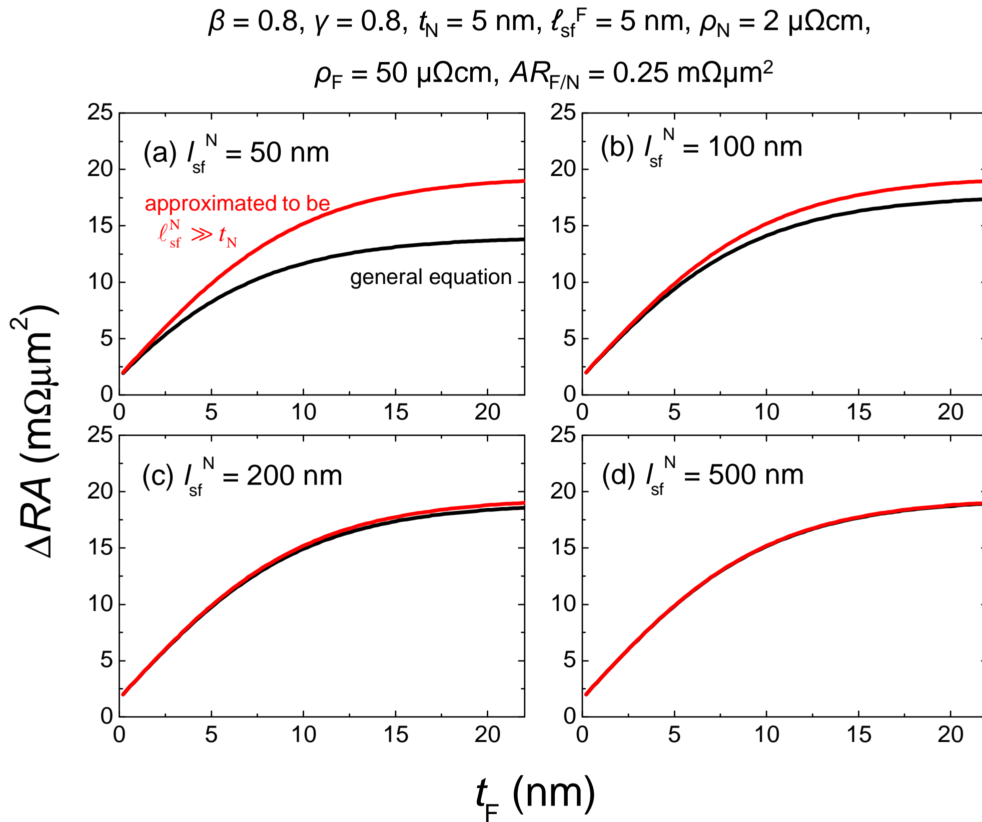

Fig. 2-7 Plots of ΔRA–t_F by the most general equation (Eq.2.23, 2.24, 2.25) for the spin diffusion lengths of the nonmagnetic layer of 50, 100, 200, and 500 nm (red) and by the approximated equation as $\ell_{sf}^{N} >> t_N$ (Eq. 2.25–2.26) (black). The deviation of the plots by the two equations is sufficiently small for $\ell_{sf}^{N} > 40 t_N$.

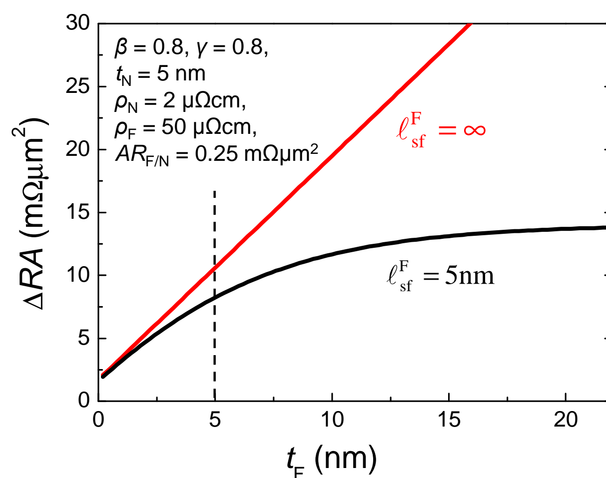

Fig. 2-8 Plots by the general equation including the spin diffusion length of the ferromagnetic layer for ℓ_{sf}^{F} = 5 nm (black) and the equation for $\ell_{sf}^{F} = \infty$ (Eq. 2.28). The dotted line indicates the spin diffusion length.

References

[1] P. C. van Son, H. van Kempen, and P. Wyder, Phys. Rev. Lett. **58**, 2271 (1987).

[2] (as reviews) S. Takahashi, and S. Maekawa, Sci. Technol. Adv. Mater. **9**, 014105 (2008). H. Imamura, Kinzoku **77**, 982 (2007) (in Japanese).

[3] T. Valet, and A. Fert, Phys. Rev. B **48**, 7099 (1993).

[4] J. Bass, and W. P. Pratt, Jr., J. Phys.: Condens. Matter **19**, 183201 (2007).

[5] T. Taniguchi, H. Imamura. T. M. Nakatani, and K. Hono, Appl. Phys. Lett. **98**, 042503 (2011).

Chapter 3　Experimental descriptions

3.1　Choice of the Heusler alloy composition

For the purpose of this thesis, the Heusler alloy composition was selected to a $Co_2Fe(Al_{0.5}Si_{0.5})$ (hereafter, abbreviated as CFAS), which is one of the well-established Heusler alloy compositions. The CFAS alloy was first reported by Tezuka *et al*. in 2006 for an electrode of a magnetic tunnel junction (MTJ) [1]. They reported a tunnel magnetoresistance (TMR) ratio 76% at room temperature using B2 ordered CFAS films for the bottom electrode and AlO_x amorphous barrier. Interestingly, this TMR ratio was higher than those with $L2_1$ ordered Co_2FeSi or Co_2FeAl electrodes [2]. Afterward, they fabricated fully epitaxial MTJs with the CAFS film for both bottom and top electrodes and MgO single crystalline barrier, and obtained much large TMR ratios of up to 220% at room temperature [3][4]. Fecher and Felser reported the electronic structures of the $Co_2Fe(Al_xSi_{1-x})$ alloys by *ab intio* calculations as shown in Fig. 3-1 [5]. They showed that the Fermi level of the central composition of this system, *i.e.* $Co_2Fe(Al_{0.5}Si_{0.5})$ lay at the center of the minority band gap (Fig. 3-1(c)), whereas those of the terminal alloys were near the edges of the minority gap (at the conduction side for Co_2FeSi and at the valence side for Co_2FeAl). This is due to the tuning of the number of the valence electron by the substitution of Al with Si. They mentioned that the half-metallicity of the alloy with the Fermi level near the valence or conduction edge may be unstable against temperature increase or disordering of the chemical ordering. On the other hand, if the Fermi level lies at the center of the gap, the half-metallic property may be robust against both temperature increase and disordering. The concept of obtaining a preferential position of the Fermi level by substituting the constituent of the Heusler alloy with a forth element is called *Fermi level tuning*. Nakatani *et al*. experimentally studied the spin polarizations of the bulk $Co_2Fe(Al_xSi_{1-x})$ alloys by means of the point contact Andreev reflection (PCAR) spectroscopy. They showed that the central composition of the system, *i.e.* $Co_2Fe(Al_{0.5}Si_{0.5})$ alloy had the

highest spin polarization of P ~0.60 by PCAR, whereas those of the terminal compositions of Co_2FeSi and Co_2FeAl were ~0.57 and ~0.56, respectively [6]. The effect of the Fermi level tuning has also been suggested in the transport property of the MTJs [7]. Furubayashi *et al.* first applied the CFAS alloy to a CPP-GMR device with Ag spacer layer and obtained a relatively high CPP-GMR output [9]. Currently, the CFAS alloy is regarded as one of the best materials to obtain high CPP-GMR outputs as well as Co_2MnSi or Co_2MnGe alloys.

The aim of this thesis is (i) to clarify the spin-dependent scattering in CPP-GMR with a Heusler alloy, and (ii) to select a suitable spacer layer material to combine with Heusler magnetic layers. Therefore, we selected the well-established CFAS alloy for the material of the magnetic layers of the CPP-GMR devices.

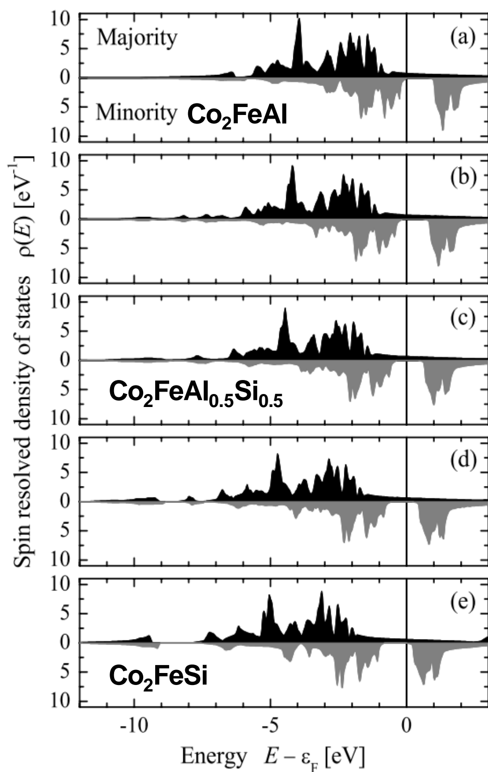

Fig. 3-1 Calculated density of states of $Co_2Fe(Al_{1-x}Si_x)$ alloys. (a) x = 0, (b) x = 0.25, (c) x = 0.5, (d) x = 0.75, and (e) x = 1 by Fecher and Felser [5].

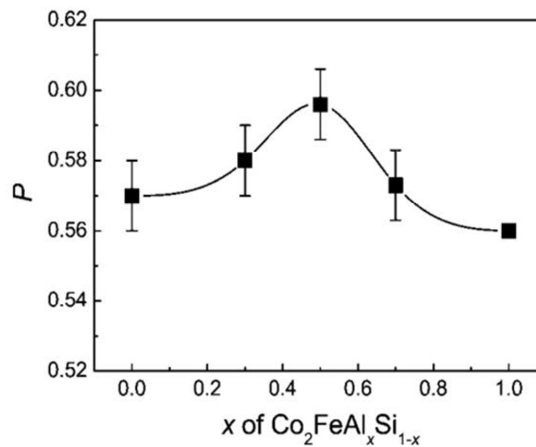

Fig. 3-2 Spin polarizations of $Co_2Fe(Al_xSi_{1-x})$ alloys measured by the point contact Andreev reflection method at 4.2 K by Nakatani et al. [6]

3.2 Fabrication of thin films

3.2.1 Sputtering machine and the deposition conditions

All the films were fabricated by a standard magnetron sputtering system manufactured by Eiko Engineering Co.,Ltd, Japan. The sputtering machine equips ten 3-inchs targets with one sputtering cathode and dc and rf power supplies. The target-substrate distance is variable from 70 mm to 150 mm. The base pressure reaches 5×10^{-8} Pa. The sputtering gas is high purity Ar and the atmosphere pressure was typically higher than 3 mTorr for magnetic targets and higher than 5–8 mTorr for nonmagnetic targets with the dc power. The Ar pressure can be reduced further with the rf power. The deposition conditions of the metals and alloys used in this work are summarized in Table 3-1.

A MgO(001) single crystalline substrate (purchased from Furuuchi Chemical Corp., Japan) was used to fabricate fully epitaxial CPP-GMR devices. The cleaning and treatment of the MgO substrates was done as follows. This is based on the established procedure as describe in Ref. [8].

1. Cut substrate with a diamond pen.
2. Ultrasonic clean with deionized water for 1 min to remove particles.
3. Ultrasonic clean with acetone for 5 min.
4. Change the acetone to new one and ultrasonic clean for another 10 min.
5. Ultrasonic clean with deionized water for 3 min.
6. Rinse with isopropanol (IPA).
7. Blow with dry N_2 gas.
8. Pre-heat at 600 °C for 60 min in the sputtering chamber (thermal cleaning).

Material	Power	Ar gas pressure (mTorr)	Deposition rate (Å/sec)
Cr	DC10 W	8.0	0.5
Ag	RF30 W	5.0	0.9
$Co_2FeAl_{0.5}Si_{0.5}$	DC10 W	3.0	0.4
$Co_{50}Fe_{50}$	DC10 W	3.0	0.35
$Ir_{22}Mn_{78}$	DC10 W	7.0	0.7
Ru	DC10 W	7.0	0.33
NiAl	DC10 W	4.0	0.35

Table 3-1 Sputtering conditions. The target–substrate distance is fixed to 100 mm.

3.2.2 Underlayer for CPP-GMR devices

Characterization of the CPP-GMR properties is done by measuring the resistance of devices microfabricated into submicron or 100 nm size pillars. Since all of the films of CPP-GMR devices are metals, the resistance-area product (*RA*) of the CPP-GMR stack perpendicular to the plane is typically a few tens m$\Omega\mu m^2$. Thus, the resistance of the microfabricated pillar is several Ω at the most, therefore the effect of the resistance of the lead electrodes is not negligible. If the resistance of the pillar is not significantly higher than that of the lead electrodes, the current tends to flow along the side wall of the pillar, thus the current distribution is inhomogeneous in the pillar. This is called current crowding, which leads to an overestimation of the values of *RA* and ΔRA. Therefore, a thick underlayer composed of a low resistive material is indispensable to decrease the lead resistance. In our group, Cr/Ag underlayer has been established for epitaxial CPP-GMR devices on a MgO(001) substrate [9]. The Cr (10 nm) layer is for a seed layer for a better epitaxial growth of the film on it, and the Ag (100–200 nm) act as the lead electrode for the CPP-GMR device.

In order to confirm the current distribution in the pillars, simulations were carried out. Due to the restriction of the simulation method we used, it was not possible to vary the thickness of the lead electrode. Instead, the resistivity of the lead electrodes was

varied to 0.1, 1.0, and 10 μΩcm for a fixed thickness of 20 nm, corresponding to 400 nm, 40 nm and 4 nm thick Ag layers with ρ = 2 μΩcm. Pillars with the size of 80 nm×160 nm were simulated. As shown in Fig. 3-3(c), the current distribution in the pillar of Ag(5 nm)/Heusler(10 nm)/Ag(5 nm) with the lead electrode of 10 μΩcm is inhomogeneous. The current is concentrated at the side wall of the pillar. By reducing the resistivity of the leads to 1 μΩcm (effectively Ag 40 nm leads), the current distribution in the pillar becomes almost homogeneous. For 0.1μΩcm (effectively Ag 400 nm leads), the current distribution is perfectly homogeneous in the pillar.

In this work, we deposit a 100 nm thick Ag underlayer as the lead electrode of CPP-GMR devices. These simulations may guarantee the homogeneous current distribution in the CPP-GMR pillars deposited on the 100 nm thick Ag underlayer. In addition, although the current distribution in the pillar is homogeneous, there is a curvature of the current at the corner between the pillar and the lead electrode. This may cause a parasitic resistance apart from the resistance of the pillar.

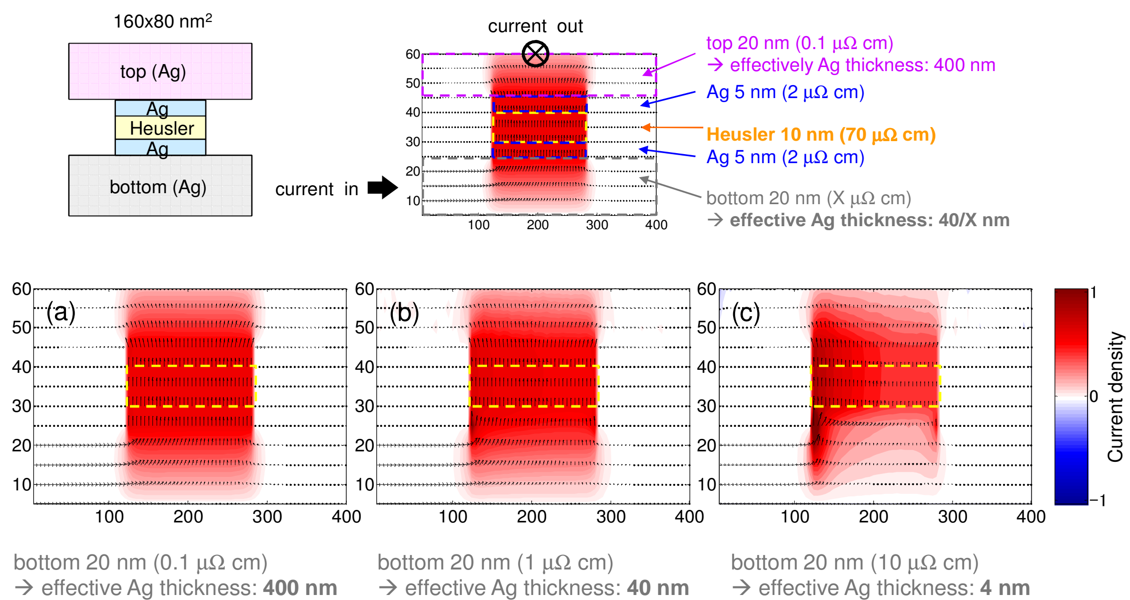

Fig. 3-3 Simulated current distribution in Ag lead(20 nm)/Ag(5 nm)/Heusler(10 nm)/Ag(5 nm)/Ag lead(20 nm) pillar. The pillar size is 160 nm×80 nm rectangle. The resistivity of the Ag lead was varied to (a) 0.1, (b) 1.0, and (c) 10 μΩcm with keeping the thickness ot 20 nm. This corresponds to change the thickness of the Ag lead to 400, 40, and 4 nm, respectively.
By courtesy of Masamitsu Hayashi.

3.3 Microfabrication

Microfabrication was carried out by a combination of photo and electron beam lithographies and Ar ion etching. The photo lithography was used for the pattering of the bottom lead electrode and the formation of the deposition mask of the top lead electrode. The electron beam lithography was applied only to the fabrication of the CPP-GMR pillars. The microfabrication procedure which is schematically described in Fig. 3-4 takes about 10 hours in total. The resists and the conditions are following.

Photo lithography

Resist: AZ 1500 positive resist (AZ Electronic Materials)

Condition (1) Spin coating at 5000 rpm for 30 sec

(2) Pre-baking at 100 °C for 1 min

(3) Exposure at ~10 mW/cm^2 (mercury lanp) for 8 sec

(4) Development with TMAH* 2.38% for 20 sec

(5) Rinse with deionized water

(6) Post-baking at 120 °C for 60 sec

(7) To Ar ion etching

* TMAH (Tetra-methyl-ammonium-hydroxide) is a developer for positive resist.

EB lithography

Resist: ma-N2403 negative resist (micro resist technology)

Condition

(1) Spin coating of the promoter HMDS* at 5000 rpm for 60 sec

(2) Pre-baking at 90 °C for 5 min

(3) Spin coating of the resist at 5000 rpm for 60 sec

(4) Pre-baking at 90 °C for 2 min

(5) Spin coating of the conductive solution (Espacer, Showa Denko) at 5000 rpm for 60 sec

(6) Electron beam exposure

(7) Development with a TMAH based developer for ~80 sec

(8) Rinse with deionized water

(9) To Ar ion etching

* HMDS (Hexamethyldisilazane) promotes the adhesion of the resist.

At the end of the microfabrication process, Ta(2 nm)/Cu(250 nm)/Ta(10 nm) layers were deposited as a lead electrode. The first Ta(2 nm) layer is for a better adhesion of the Cu layer, and the Ta(10 nm) layer is for capping. After the photolithography of the electrode pattern, the samples were Ar ion etched for 10–20 sec (this etches the Ru capping by a few nm), subsequently the Ta/Cu/Ta electrode was sputter–deposied. The etching is to clean the contact between Ru and the electrode. Otherwise, the devices contained a large parasitic resistance, which is probably due to some contamination formed during the microfabrication process like a residual resist.

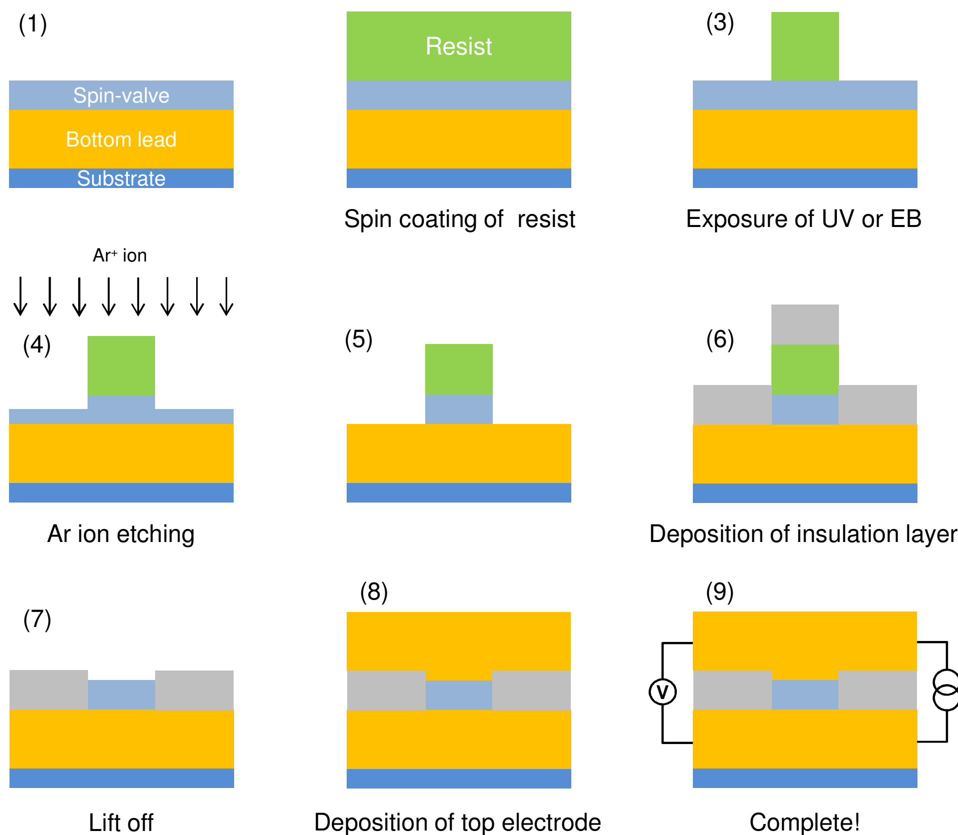

Fig. 3-4 Microfabrication procedures of CPP-GMR device.

3.4 Characterizations of film

X-ray diffraction

Crystalline structure was characterized by x-ray diffraction (XRD) by a 4-axis diffractmeter (Rigaku Corp., SmartLab). The scanning geometries used in this study were θ-2θ and ϕ scans.

Transmission electron microscopy

Transmission electron microscopy was employed for the microstructure characterizations. The used TEM was Tecnai F30 (FEI Company). The cross-sectional specimens were made by a standard procedure as follows.

(1) Cut the substrate into strips with a size of ~1 mm×5 mm.
(2) Paste two strips of the sample of film to film with epoxy glue.
(3) Mechanically polish with emery papers down to ~50 μm thick.
(4) Fix the specimen on molybdenum mesh (3 mm diameter).
(5) Ar ion etching by Gatan Precision Ion Polishing System (PIPS) with liquid N_2 cold stage. The acceleration voltage is initially at 4–5 kV until a hole forms at the center of the specimen (this takes typically 10 hrs for MgO substrate, and 4 hrs for Si substrate), then finish at 1 kV for 30 min.

The usage of the liquid N_2 cold stage is not always necessary to make cross-sectional specimens, but it was critical for films with Ag underlayers. When the films are polished at room temperature, the surface of the specimen is covered with some contamination. The contamination is considered to be surface-diffused or re-deposited Ag. The Ar ion etching with the cold stage released us from the contamination of the specimen.

Magnetic property measurement

Magnetic property was measured by a vibrating sample magnetoremer (VSM) (LakeShore Cryotronics, Inc).

3.5 Transport measurement

3.5.1 Electrical resistivity and Hall measurements

The resistivity and the Hall effect of the CFAS and Ag films were measured by a 4-probe method using pattered films into Hall bars by a photolithography as shown in Fig. 3-5. A physical property measurement system (PPMS) (Quantum Design) was used for the Hall measurement to obtain the high field up to 9 Tesla.

The resistivity of the film was obtained by the following equation.

$$\rho = R\frac{wt}{L}, \qquad (3.1)$$

where R is the measured resistance, w is the width of the pattered line, t is the film thickness and L is the sample length.

In a classical description, the Hall effect is derived from the Lorentz force of the electrons driven by the bias voltage. Obtaining the Hall coefficient gives us important information on the electronic transport of the material, *i.e.* the carrier type, the carrier density, and the relaxation time of scattering. The Hall coefficient R_H and the Hall resistivity are defined by

$$R_H = E_y / J_x B_z, \qquad (3.2)$$

$$\rho_H = E_y / J_x = R_H / B_z, \qquad (3.3)$$

where J_x, E_y and B_z are the current density, the Hall field and the magnetic flux density as shown in Fig. #. Using the Hall voltage V_y , the current I_x the width w and the thickness t of the sample, $E_y = V_y/w$ and $J_x = I_x/wt$, thus

$$R_H = V_y t / I_x B_z \qquad (3.4)$$

$$\rho_H = V_y t / I_x. \qquad (3.5)$$

The unit of R_H is [m^3/A·s] (because [T] = [Wb/m^2] = [V·s/ m^2]). Due to the definition of R_H, the sign of R_H corresponds to that of the carrier (negative for electron and positive for hole). The carrier density n and the mean free path ℓ can be estimated by the Drude's free electron mode as follows. For the carrier density,

$$R_H = -1/ne, \qquad (3.6)$$

where e is the absolute value of the elementary electric charge e = 1.6×10^{-19} [C]. Next, the mean free path is defined by

$$\ell = v_{\mathrm{F}}\tau , \tag{3.7}$$

where v_{F} is the Fermi velocity and τ is the relaxation time of scattering given by the free electron model

$$v_{\mathrm{F}} = \frac{\hbar}{m}(3\pi^2 n)^{1/3} \tag{3.8}$$

$$\rho = \frac{m}{ne^2\tau}, \tag{3.9}$$

where m is the electron mass (m = 9.1×10^{-31} kg). Therefore, the mean free path is given by

$$\ell = \frac{\hbar^2(3\pi^2 n)^{1/3}}{ne^2\rho}. \tag{3.10}$$

It is convenient to use the representations given by Achcroft and Mermin [13] of

$$\tau = \left(\frac{0.22}{\rho}\right)\left(\frac{r_s}{a_0}\right)^3 \times 10^{-14}\,\mathrm{sec}, \tag{3.11}$$

$$\ell = \frac{(r_s / a_0)^2}{\rho} \times 92\,\text{Å}. \tag{3.12}$$

Here, r_s is the radius whose volume is equal to the volume per conduction electron, $r_s = \left(3/(4\pi n)\right)^{1/3}$, a_0 is the Bohr radius, $a_0 = \hbar/(me^2) = 0.529\times10^{-8}\,\mathrm{cm}$, and ρ in μΩcm.

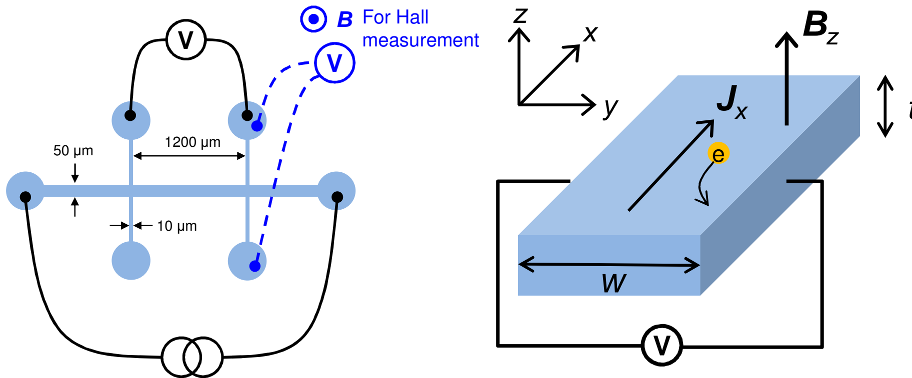

Fig. 3-5 (left) Sample for the resistivity and Hall measurements. (right) Schematic description of the Hall effect.

3.5.2 MR measurement

The CPP-GMR property was measured by a dc 4-pbobe method with a constant sense current typically 0.1–1.0 mA with a setup schematically described in Fig. 3-6. The low temperature measurement was carried out with a helium compressor refrigerator which reaches down to around 15 K. The temperature control was done by manually adjusting the heater power. The thermoelectric power generated between the sample temperature and room temperature was subtracted by reversing the current polarity (delta mode).

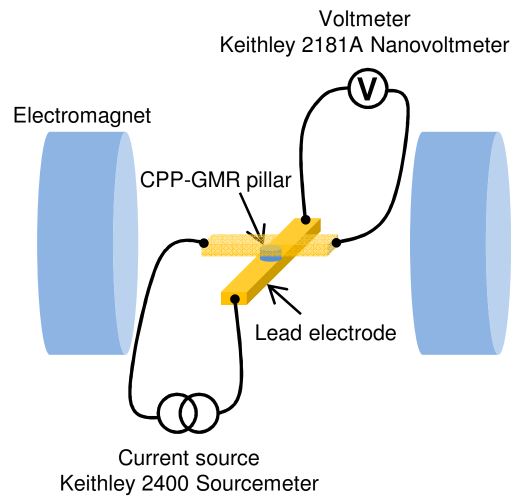

Fig. 3-6 Setup for the MR measurement.

References

[1] N. Tezuka, N. Ikeda, A. Miyazaki, S. Sugimoto, M. Kikuchi, and K. Inomata, Appl. Phys. Lett. **89**, 112514 (2006).

[2] N. Tezuka, S. Okamura, A. Miyazaki, M. Kikuchi, and K. Inomata, J. Appl. Phys. **99**, 08T314 (2006).

[3] N. Tezuka, N. Ikeda, S. Sugimoto, and K. Inomata, Appl. Phys. Lett. **89**, 252508 (2006).

[4] N. Tezuka, N. Ikeda, S. Sugimoto, and K. Inomata, Jpn. J. Appl. Phys. **46**, L454 (2007).

[5] G. H. Fecher, and C. Felser, J. Phys. D: Appl. Phys. **40** 1582 (2007).

[6] T. M. Nakatani, A. Rajanikanth, Z. Gercsi, Y. K. Takahashi, K. Inomata, and K. Hono, J. Appl. Phys. **102**, 033916 (2007).

[7] R. Shan, H. Sukegawa, W. H. Wang, M. Kodzuka, T. Furubayashi, T. Ohkubo, S. Mitani, K. Inomata, and K. Hono, Phys. Rev. Lett. **102**, 246601 (2009).

[8] 桜庭裕弥　博士論文　東北大学. (Ph. D thesis, Y. Sakuraba, Tohoku University).

[9] T. Furubayashi, K. Kodama, H. Sukegawa, Y. K. Takahashi, K. Inomata, and K. Hono, Appl. Phys. Lett. **93**, 122507 (2008).

[10] T. Mizuno, Y. Tsuchiya, T. Machita, S. Hara, D. Miyauchi, K. Shimazawa, T. Chou, K. Noguchi, and K. Tagami, IEEE Tran. Magn. **44**, 3584 (2008).

[11] Y. Sakuraba, T. Iwase, K. Saito, S. Mitani, and K. Takanashi, Appl. Phys. Lett. **94**, 012511 (2009).

[12] K. Nikolaev, P. Kolbo, T. Pokhil, X. Peng, Y. Chen, T. Ambrose, O. Mryasov, Appl. Phys. Lett. **94**, 222501 (2009).

[13] N. W. Ashcroft, and N. D. Mermin, *Solid State Physics*, Chap. 1, Books/Cole, 1976.

Chapter 4 Fabrication of CPP-GMR spin-valves with $Co_2Fe(Al_{0.5}Si_{0.5})$ Heusler alloy layer and Ag spacer layer

4.1 Introduction

This chapter describes

(1) Fabrication of Cr/Ag underlayer for a lead electrode for CPP-GMR devices.

(2) Fabrication of the CFAS films and the characterizations of the crystal structure, the magnetic property, and the electric resistivity.

(3) Interlayer coupling in CFAS/Ag/CFAS trilayers.

(4) Fabrication of the exchange biased spin-valve with CFAS magnetic layers and a Ag spacer layer.

(5) Fabrication of pseudo spin-valve with CFAS magnetic layers and a Ag spacer layer.

(6) Evaluation of the critical sense current density of the appearance of the spin torque effect.

The exchange biased spin-valve was employed at the early stage of this work to due to the convenience to obtain the antiparallel magnetization configuration between the two ferromagnetic layers. However, the devices with various thicknesses of the magnetic layer have to be measured to investigate the spin-dependent scattering characteristics. In exchange spin-valves, varying the thickness of the pinned layer in a wide range (*e.g.* up to ~20 nm) is difficult due to the insufficient pinning force for thick ferromagnetic layers. Therefore, we shifted to pseudo spin-valves without the pinning layer to study the spin-dependent scattering characteristics which will be described in Chapter 5.

4.2 Fabrication of Cr/Ag underlayer

There are two roles for the underlayer of CPP-GMR devices; (i) a buffer layer for the growth of the films on it, and (ii) a lead electrode the transport property of the layers on it in the CPP geometry. For (i), the underlayer has to have a good wetness (adhesion) with the substrate, a formability of the flat surface, and a small lattice misfit with the Heusler alloy to deposit on. On the other hand, for (ii), the resistivity of the under has to be low and the thickness has to be sufficiently thick to avoid the current crowding as shown in 3.2.2. To satisfy these criteria, the Cr/Ag underlayer was chosen. Although Cr is often used as a buffer layer for Heusler alloy films because Cr grows flatly and has the small lattice misfit with Heusler alloys, the resistivity of Cr of 13 μΩcm is not low enough for using as the lead electrode. Thus, Ag was used for the lead electrode due to the low resistivity of 1.6 μΩcm [1]. Ag is also a good buffer layer for Heusler alloys or CoFe alloy with the B2 structure. For the epitaxial relationship of Ag(001)[100]//Heusler(001)[110] (45° rotation in plane),the lattice misfit is 1.7% with the $Co_2Fe(Al_{0.5}Si_{0.5})$ alloy (a = 5.68 Å), for example. However, it is generally said that Ag is a material with a poor wetness with other metals, therefore the establishment of the fabrication condition and the treatment of the Ag layer is required. In TMR devices, the flatness between the ferromagnetic electrodes and the tunnel barrier is thought to be very importance since rough interfaces may cause pin holes. Although it is not very clear whether the interfacial roughness influences on CPP-GMR properties as well as TMR, flat interface is thought to be preferential.

Figure 4-1 shows the average roughness (R_a) and the peak-to-valley height (p-v) of the MgO(001)//Cr(10 nm)/Ag(100 nm)/CFAS(20 nm) films for various annealing temperatures after deposing the CFAS layer. All the layers were deposited at room temperature. No annealing was done after depositing the Ag underlayer. The surface flatness of the CFAS film was measured by AFM. The surface flatness of the as-deposited CFAS film was R_a = 0.24 nm and p-v = 2.3 nm, and it improved with higher annealing temperature after the deposition of the CFAS layer, reached R_a = 0.12 nm and p-v = 1.56 nm for T_{an} = 500 °C. The improvement is presumably due to the atomic diffusion on the surface of the CFAS film, the interface between the Ag underlayer and the CFAS layer may be rough. Thus, there is still a room to improve surface flatness of the CFAS film by improving the fabrication process of the Ag underlayer.

Figure 4-2 shows the variation of the flatness of the CFAS film deposited on Cr(10

nm)/Ag(100 nm) as a function of the annealing temperature after the deposition of the Ag underlayer. The CFAS layers were annealed at a common temperature of 400 °C. The annealing for the Ag underlayer effectively improved the flatness as seen in Fig. 4-2(a). Fig. 4-2(b) is for T_{an} = 300 °C, the surface of the CFAS layer is very flat, which is suitable for the fabrication of CPP-GMR devices. Hereafter, the annealing process of at 300 °C for 30 min was applied for all of films with the Ag underlayer.

[Note 1] Although Ag layer is epitaxially grown directly on the MgO(001) substrate, the surface roughness and the crystallinity of the CFAS layer on Ag was poorer than that on the Cr/Ag underlayer. Therefore, Cr plays an important role as s seed layer for the growth of the Ag layer.

[Note 2] These experiments were carried out at the early stage of the thesis work. In those days, it was our understnding that the magnetic layer has to be thick (*e.g.* more than 10 nm) and be *in situ* annealed before depositing the spacer layer to obtain the high CPP-GMR properties. However, we came to know that the high CPP-GMR properties could be obtained even with thin CFAS layers without the *in situ* annealing. We have confirmed that the surface of CFAS (5 nm) as-deposited film on the Cr (10 nm)/Ag (100 nm) underlayer annealed at 300 °C was very flat (R_a = 0.1 nm and *p-v* = 1.0 nm) as well as the films of Fig. 4-2.

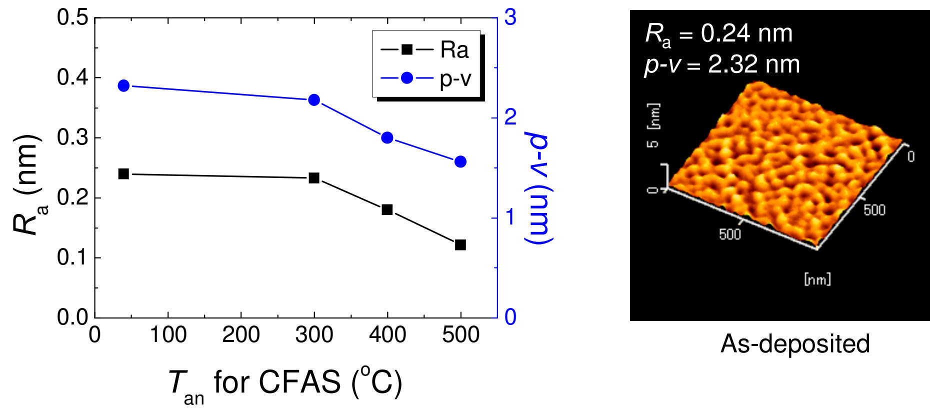

Fig. 4-1 Surface roughness (R_a and p-v) of CFAS(20 nm) deposited on MgO(001) substrate/Cr(10 nm)/Ag(100 nm) for various temperature of the post-annealing after deposition of the CFAS layer.

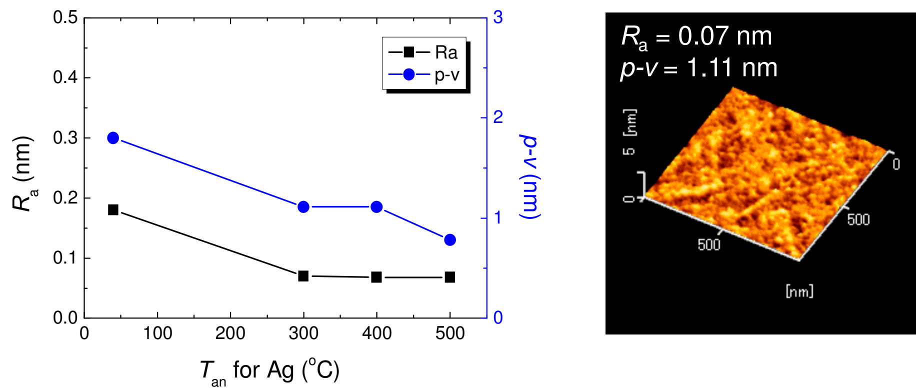

Fig. 4-2 Surface roughness (R_a and p-v) of CFAS(20 nm) deposited on MgO(001) substrate/Cr(10 nm)/Ag(100 nm) for various temperature of the post-annealing after deposition of the Ag layer. The post annealing temperature after depositing the CFAS layer was fixed to 400 ℃.

4.3 Fabrication of CFAS film

The $Co_2Fe(Al_{0.5}Si_{0.5})$ Heusler alloy (CFAS) films used in this work were deposited from an alloy target with a composition of $Co_2FeAl_{0.6}Si_{0.4}$. The composition of the films deposited from this target with a dc 10 W sputtering power and under an Ar 3 mTorr atmosphere was 59.12%Co–28.30%Fe–7.55%Al–5.03%Si (in atomic %), corresponding to $Co_{2.00}Fe_{1.01}Al_{0.56}Si_{0.36}$. This is 10% deficient for the Z elements, although the ratio between Co and Fe is almost stoichiometric. To make film the composition stoichiometric $Co_2FeAl_{0.5}Si_{0.5}$, a Si wafer was mounted on the target. The size of the Si wafer was adjusted, resulting in an almost stoichiometric 57.93%Co–27.59%Fe–7.59%Al–6.90%Si, corresponding to $Co_{2.00}Fe_{1.01}Al_{0.57}Si_{0.50}$.

Samples for crystal characterization and magnetic measurement

Characterizations of the crystal, magnetic properties of the CFAS films were carried out in films of MgO(001) substrate/Cr (10 nm)/Ag (100 nm)/CFAS (10 nm)/Ag (5 nm)/Ru (5 nm). The thickness of 10 nm was necessary to obtain the sufficient count for the x-ray diffraction and the magnetic moment for the VSM measurement. The Ag (5 nm) layer was inserted to make the environment surrounding the CFAS layer the same as the bottom magnetic layer of the CPP-GMR devices with the Ag space layers. The Ru layer is for a protective layer. The annealing for the CFAS layer at T_{an} = 250–550 °C was done after the depositions of all the layers in a vacuum chamber (different from the sputtering chamber) which we use for a magnetic annealing.

Samples for resistivity and Hall measurements

The CFAS films on the Ag underlayer are not suitable for in-plane electric measurements. In addition, the films have to be sufficiently thick to reduce the effect of the surface scattering. Thus, CFAS (80 nm) films was deposited directly on an MgO(001) substrate. Ru (3 nm) film was deposited for the surface protection. For the resistivity and Hall measurements, the films were patterned into the Hall bar as described in 3.5.1.

4.3.1 Crystal structure

Figure 4-3(a) shows the θ-2θ scan profiles from the 001 plane of the films for the various annealing temperatures ranging from 250 °C to 550 °C and the as-deposited. For all the annealing temperature, only the peaks with the indexes of 002 and the

multiples can be seen. Thus these films have (001) texture in the out-of-plane direction. To to know the in-plane crystallographic relationship, ϕ scan profiles were taken from the Ag 220 and CFAS 220 fundamental diffractions as shown in Fig. 4-3(b). The peaks of Ag and CFAS appear with a 45° offset of the ϕ rotation, indicating a 45° in-plane rotation relationship between the Ag and the CFAS layers. Therefore, the epitaxial relationship is Ag(001)[100]//CFAS(001)[110]. The lattice misfit ratio is –1.7% with regard to Ag estimated from the bulk lattice parameters of a_{CFAS} = 5.68 Å and a_{Ag} = 4.086 Å. The out-of-plane lattice parameters $a_{\perp}$ were evaluated from the CFAS 400 and Ag 002 diffraction peaks. Figure 4-5(a) and (b) show the dependences of $a_{\perp}$ of the CFAS and Ag films on the annealing temperature, respectively. For all the annealing temperature, $a_{\perp}$ of the CFAS films are smaller than that of the bulk alloy. This is probably because the CFAS layer has grown coherently on the Ag underlayer with almost the same lattice parameter as Ag. As the misfit ratio of CFAS is negative with regard to Ag ($a_{\mathrm{CFAS}} < \sqrt{2}\, a_{\mathrm{Ag}}$), the in-plane lattice of CFAS has to expand to match with Ag, then the out-of-plane lattice of CFAS shrinks to maintain the volume of the unit cell. Figure 4-5(c) shows the variation of the full-width at half-maximum (FWHM) of the CFAS 004 fundamental peak. For the annealing temperature below 450 °C, the values of FWHM were below 0.35° which is small for epitaxial Heusler alloy films. However, the annealing higher than 500 °C degraded the quality of the crystal as indicated the increase of the FWHM value.

The θ-2θ scan from the 111 plane was measured as shown in Fig. 4-4 for T_{an} = 450, 500 and 550 °C. The diffraction angle of the 111 $L2_1$ superlattice is around 2θ = 27°, which is not seen in the CFAS film for the annealing temperatures up to 550 °C. Thus, the chemical order of the CFAS films is the B2 structure. Wan *et al.* reported the appearance of the $L2_1$ ordering by post-annealing at 540 °C and the enhancement of the degree of $L2_1$ order by annealing at higher than 600 °C for the CFAS films deposited on MgO buffer layer on MgO(001) substrate [3]. However, such a high temperature annealing may not be beneficial due to the degraded crystallinity of the CFAS films shown in Fig. 4-5(c). Indeed, the value of the device resistance *RA* of the pseudo spin-valves (described in 4.5) increased for T_{an} = 550 °C.

The ordering parameter *S* was estimated by the equation of

$$S_{\mathrm{B2}} = \sqrt{\frac{(I_{002}/I_{004})_{\mathrm{experiment}}}{(I_{002}/I_{004})_{\mathrm{simulation}}}},$$

where I_{002} and I_{004} are the intensities of the 002 B2 superlattice and the 004 fundamental

diffractions, the subscript of simulation means the simulated diffraction ratio for the perfectly ordered structure. The simulate intensity ratio I_{002}/I_{004} was simulated to be 0.386 for $Co_2Fe(Al_{0.5}Si_{0.5})$ by a Rietveld analysis software, RIETAN. Since thin films are generally much thinner than the penetration depth of the x-ray, the effective thickness for the diffraction (or in other words, light path of x-ray in the sample) depends on the indent angle θ. The calibration coefficient of the x-ray dependent is given as a function of the film thickness t by [2]

$$G_t = 1 - e^{-2\mu t/\sin\theta},$$

where μ is the mass absorption coefficient of the material of interest. In the case that the penetration depth of x-ray is much longer than the layer thickness, G_t can be reduced to $G_t = 2\mu t/\sin\theta$. Thus, the intensities from thin films are obtained by multiplying $\sin\theta$ to the simulated diffraction intensities for the power sample.

Figure 4-5(d) shows the intensity ratio of the 002 B2 diffraction to the 004 fundamental diffraction (I_{002}/I_{004}) and the corresponding order parameter of B2 (S_{B2}), The B2 order enhanced with increasing the annealing temperature especially higher than T_{an} = 450 °C, however, S_{B2} was up to 0.7, thus the B2 order of the CFAS film was imperfect. The enhancement of the B2 order shows a good agreement with the enhancement of the CPP-GMR output ΔRA as shown later in 4.6.6.

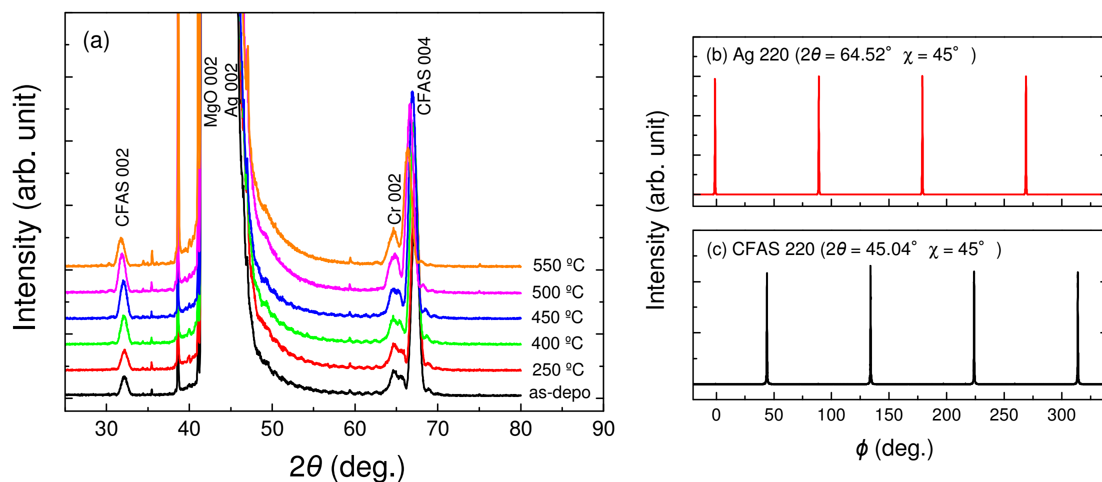

Fig. 4-3 (a) θ-2θ scan profiles of the MgO/Cr(10)/Ag(100)/CFAS(10)/Ag(5)/Ru(5) (in nm) films for various annealing temperatures T_{an} = 250–550 ℃. ϕ scan profiles of (a) Ag 220 and (b) CFAS 220 diffractions of the sample of T_{an} = 450 ℃, which confirm the in-plane 45° rotation relationship at the Ag(001)/CFAS(001) junction.

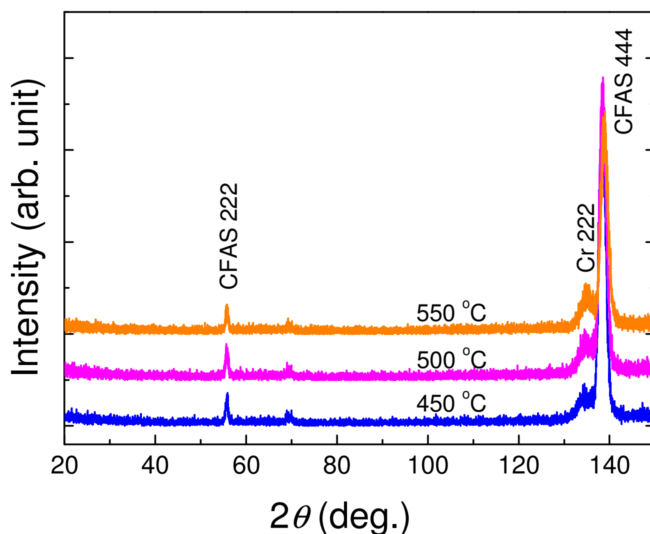

Fig. 4-4 θ-2θ scan profiles from the 111 plain with χ = 54.7°.

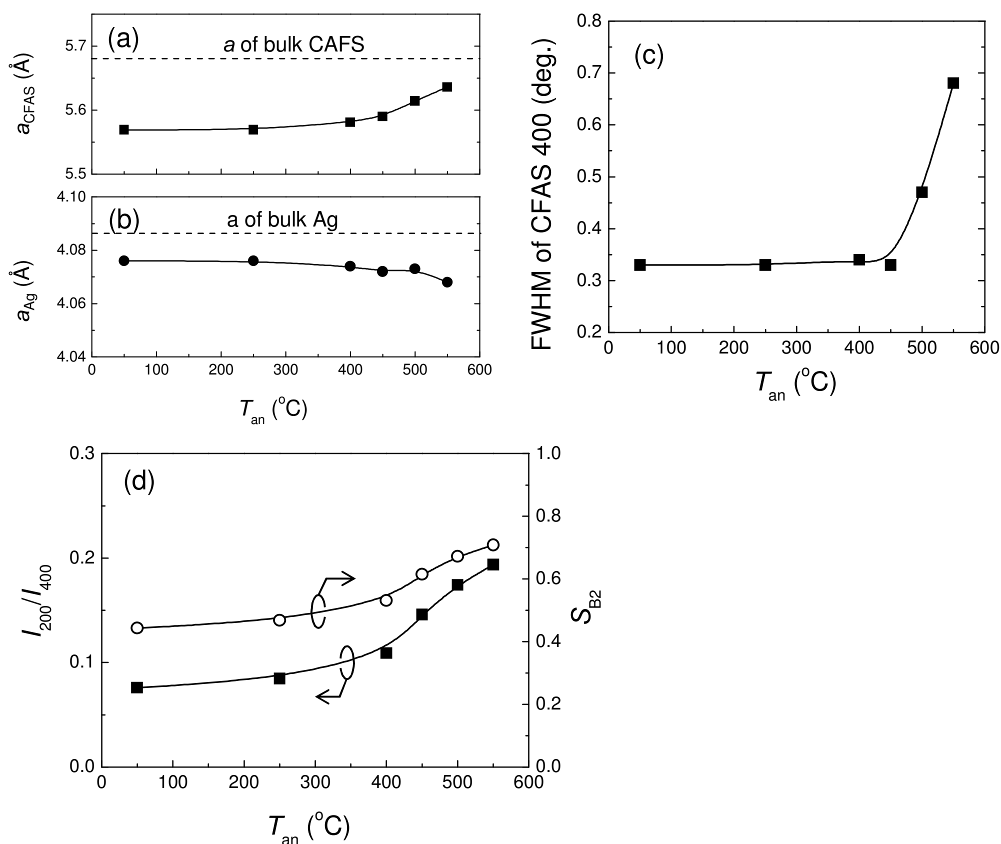

Fig. 4-5 Variations of in-plane lattice parameter of (a) CFAS and (b) Ag for annealing temperature T_{an}, (c) FWHM of the CFAS 004 peak, abd (d) enhancement of the ratio of the intensity of the 002 diffraction to that of the 004 diffraction (square) and the corresponding B2 order parameter S_{B2} (circle).

4.3.2 Magnetic property

Figure 4-6 shows the magnetization curves with the external fields parallel to the [110] and [100] directions of CFAS. The saturation magnetization M_s and the coercivity are summarized in Fig. 4-7(a). The enhancement of M_s was significant by the annealing temperature T_{an} > 400 °C, it reached 1100 emu/cc for T_{an} = 500 and 550 °C, which is close to the theoretical magnetization for the Slater-Pauling rule (5.5 μ_B/f.u. = 1113 emu/cc). Thus, the films annealed at above 500 °C may show high spin polarization. However, the coercivity increased for T_{an} = 500 and 550 °C. This may be because of the degradation of the crystallinity for the annealing temperatures as indicated by the XRD measurements (Fig. 4-5(c)).

For the annealing temperatures up to 450 °C, the ratio of remanence to saturation magnetization (M_r/M_s) clearly shows different values for the external field parallel to [110] and [100] directions of the CFAS films as shown in Fig. 4-7(b), indicating the uniaxial magnetocrystalline anisotropy of the CFAS alloy. The [110] and [100] directions were the easy and hard axes. This is consistent with the previous report for the CFAS films deposited on MgO buffered MgO(001) substrate by Wang *et al.* [3]. The uniaxial magnetocrystalline anisotropy coefficient was estimated to be 1.5×10^4–3.0×10^4 erg/cc for T_{an} < 450 °C. However, the films annealed at T_{an} = 500 °C and 550 °C did not show the clear difference of the magnetization curve between H//[110] and //[100]. The decrease of the magnetocrystalline anisotropy may due to the degradation of the crystallinity by the annealing at above 500 °C as shown by XRD.

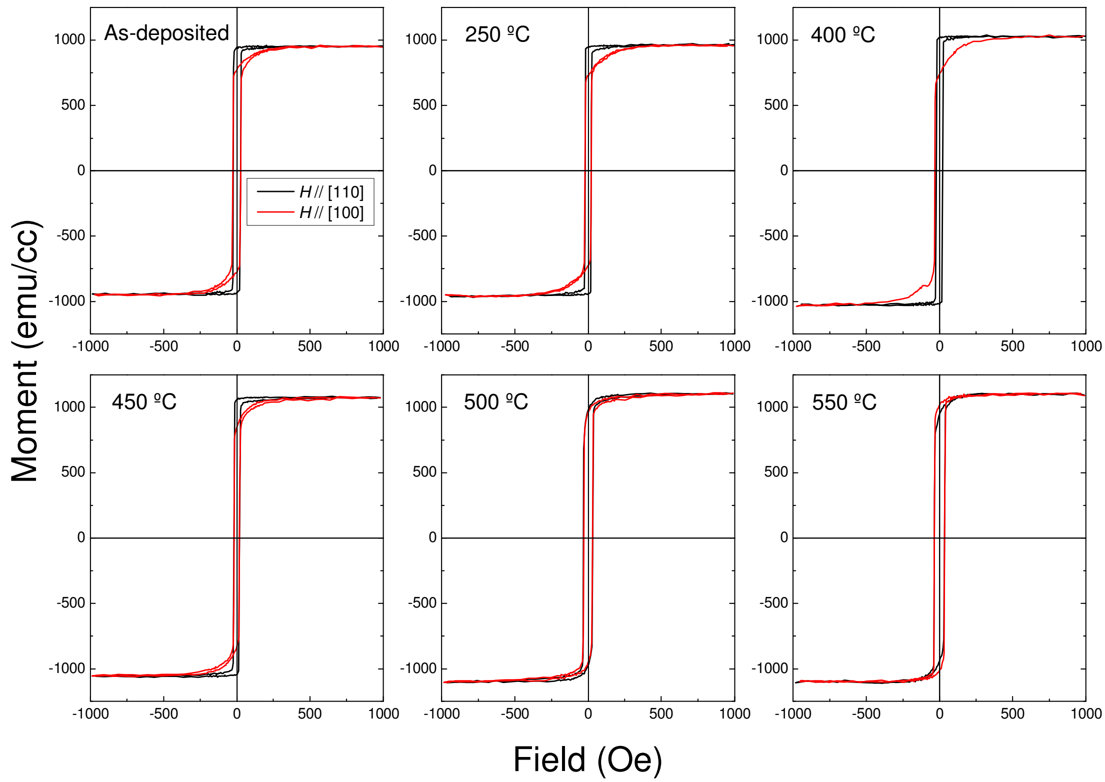

Fig. 4-6 Magnetization curves of MgO/Cr(10)/Ag(100)/CFAS(10)/Ag(5)/Ru(5) films annealed at various temperatures T_{an} = 250–550 ℃. The direction of the external magnetic field is parallel to $[110]_{CFAS}$ easy axis (black) and $[100]_{CFAS}$ hard axis (red).

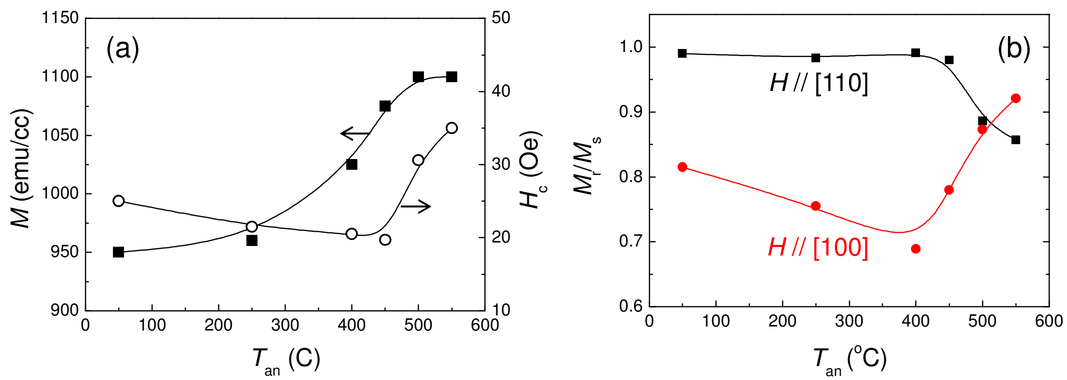

Fig. 4-7 (a) Variations of the saturation magnetization (square) and the coercivity (circle) for annealing temperature. (b) Variation of the ratios of the remanence to the saturation magnetization ratio for the applied field direction parallel to the $[110]_{CFAS}$ hard axis (square) and the $[100]_{CFAS}$ easy axis (circle).

4.3.3 Electric resistivity

The resistivity of the CFAS and the Ag films were measured for 80 nm and 100 nm thick epitaxial films, respectively. The films were deposited directly on the MgO(001) substrate. Figures 4-8(a) and (b) show the temperature dependences of the resistivity of the CFAS and the Ag films, respectively. The value of resistivity of the CFAS film annealed at 500 °C was 71.0 μΩcm and 62.4 μΩcm at 290 K and 15 K, respectively, thus the residual resistivity ratio (RRR) was 1.14. This value is significantly smaller than those of pure metals or well-ordered Heusler alloys, *e.g.* RRR = 5.2 for the bulk Co_2FeSi single crystal with an almost perfect $L2_1$ order made by the floating zone method [4]. The smaller RRR of the CFAS films is attributed to low degree of the chemical ordering. Note that the Fe, Si and Al are randomly mixed in the B2 structure. On the other hand, the resistivity of the Ag film at 290 K of 2.2 μΩcm is close to that for the bulk material of 1.6 μΩcm. The RRR was 3.45, which is relatively large for sputtered films. Thus, the quality of the Ag film should be good with small amount of impurities. It should be noted that the resistivity values measured for the films directly on the substrates can be different from those in the actual films which are deposited on the seed, buffer or spacer layers. However, it is not possible to measure the resistivities of the films in the devices with good accuracies due to the complex current distribution in multilayers. Thus, we assume that the resistivities of the CFAS and Ag films are the same as those measured in the films directly deposited on MgO substrates.

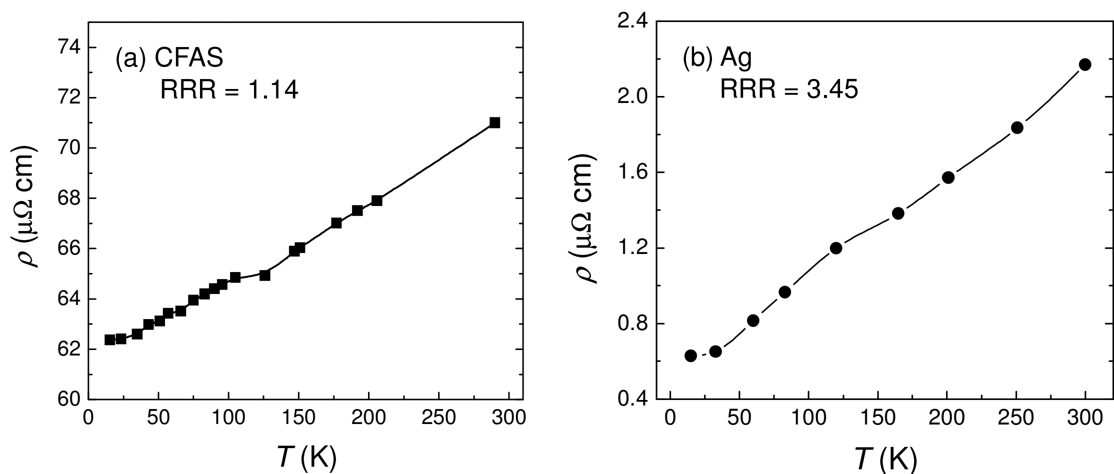

Fig. 4-8 Resistivities as a function of temperature of (a) CFAS(80 nm) film annealed at 500 ℃ and (b) Ag(100 nm) film annealed at 500 ℃. The films were deposited directly on the MgO(001) substrate.

4.3.4 Hall effect

Figure 4-9 shows the results of the Hall measurements of the CFAS (80 nm) film measured at 10 K and 300 K, and the Ag (100 nm) film measured at 300 K. Both the films were deposited directly on the MgO substrate and annealed at 500 °C for 30 min. In the CFAS films, the Hall resistivity ρ_H shows a rapid increase with increasing field below 2 T. This is due to the anomalous Hall effect which is proportional to the magnetization. The saturation field corresponds to the value of the demagnetizing field for the out-of-plane magnetization. In the high field range where the anomalous Hall effect is saturated, the normal Hall coefficient R_H is given by the gradient of ρ_H ($R_H = \rho_H/B$). The signs of the Hall coefficients of the CFAS and the Ag films were negative, thus the carrier type may be electron for both the materials.

The carrier density, the relaxation time of scattering and the mean free path were estimated for the CFAS and the Ag films based on the Drude's free electron model described in 3.6.1 as listed in Table 4-1. The carrier density of the CFAS films at room temperature was 1.63×10^{23} /cm^3, corresponding to ~7 electrons per formula unit ($Co_2FeAl_{0.5}Si_{0.5}$). A straightforward interpretation of the carrier density from the electronic structure is difficult for transition metals and alloys unless one knows the detailed Fermi surface morphology. One the other hand, the carrier density of Ag of 6.38×10^{22} /cm^3 corresponds to ~1 electron per atom is consistent with the description of the electronic structure by the free electron model, *i.e.* the valence electrons of Ag are $4d^{10}5s^1$. Estimating the mean free path of the CFAS and Ag films should be significant because we will fabricate devices with nm thick films. If the layer thickness is comparable to or larger than the mean free path, it is not valid to assume than the resistivity of the film, which is an important factor of bulk spin-dependent scattering, is the same as those of the thicker films. The mean free path of the CFAS film was ~6 Å at room temperature and ~0.7 nm at 10 K, which is much shorter than the thinnest CFAS layer thickness fabricated in this work of 2.5 nm (See 4.6.5.). Thus, the resistivity of the CFAS can be considered to be constant independent of the thickness. On the other hand, the mean free path of the Ag film of 36 nm is longer than the thickness of the spacer layer of 5 nm. Thus, the electric transport in the spacer layer is thought to be rather ballistic than diffusive (See 5.3.).

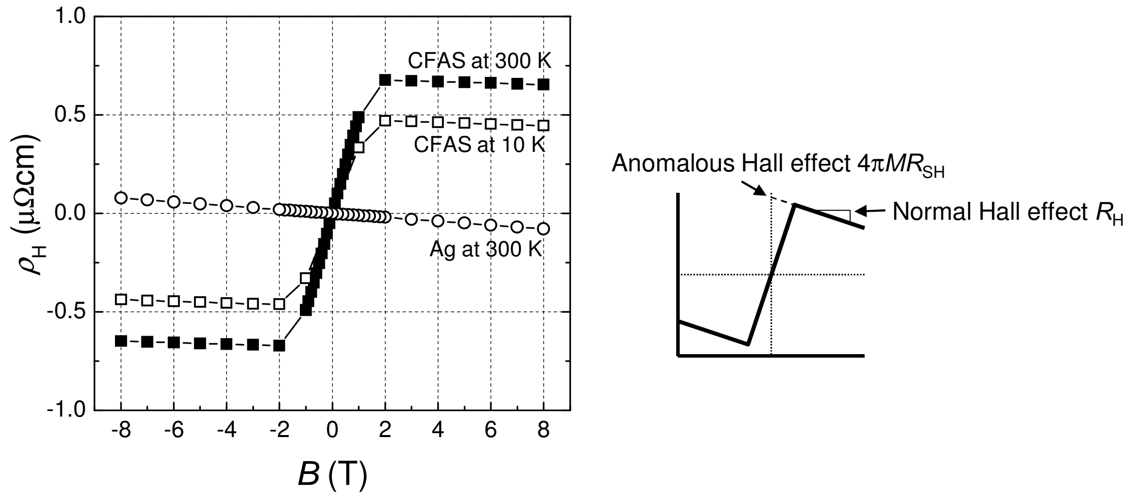

Fig. 4-9 Hall measurements of the CFAS film at 10 K and 300 K and of the Ag film at 300 K.

Material	T (K)	ρ (μΩcm)	R_H ($\times 10^{-5}$ cm^3/A·s)	n ($\times 10^{22}$ cm^{-3})	Relaxation time τ (fsec)	mean fee path ℓ (nm)
CFAS	10	61.4	-4.32	14.5	0.40	0.75
	300	71.0	-3.84	16.3	0.31	0.60
Ag	300	2.17	-9.80	6.38	25.5	36.4

Table 4-1 Summary of the Hall measurements.

4.4 Interlayer coupling in CFAS/Ag/CFAS trilayer

A magnetic coupling appears though a thin spacer layer (typically < 3 nm), the coupling strength often oscillates with the spacer layer thickness [5]. This is called interlayer exchange coupling. Practically, interlayer coupling is not preferable to fabricate spin-valves because it prevents the free magnetization rotation of the magnetic layer, thus the perfect antiparallel magnetization state may not be realized. To determine the thickness of the Ag spacer layer without any interlayer coupling, the magnetization behavior of the CFAS/Ag/CFAS trilayer was measured for various Ag thicknesses.

4.4.1 Sample structure and magnetization measurement

The structure of the samples was MgO(001) substrate/Cr(10 nm)/Ag(100 nm)/CFAS(5 nm)/Ag(t_N)/CFAS(3 nm)/Ag(3 nm)/Ru(5 nm) cap. The thickness of the Ag spacer layer t_N was varied form 1.6 nm to 5 nm. The samples were annealed at various temperatures ranging from 350–500 °C for 30 min. The magnetization behavior was measured by VSM at room temperature.

4.4.2 Magnetization behavior

Figure 4-10 shows the magnetization curves of the CFAS/Ag/CFAS trilayers as-deposited and annealed at 450 °C. All the samples with various Ag spacer layer thicknesses showed ferromagnetic–like behaviors in the as-deposited state. After the annealing at 450 °C, a reduction of the remanence/saturation ratio (M_r/M_s) for particular spacer layer thicknesses was observed, indicating an interlayer coupling. Especially, the trilayers for t_N = 1.8, 2.0 and 3.2 nm, the ratio of the remanence to the saturation magnetization (M_r/M_s) was 0.25, which corresponds to the antiferromagnetic magnetization configuration between the CFAS layers of 5 nm and 3 nm thick (because (5–3)/(5+3) = 0.25). The antiferromagnetic coupling energy J_1 is estimated briefly by

$$J_1 = -M_s H_s (t_1 + t_2)/4,$$

where M_s, H_s, t_1 and t_2 are the saturation magnetization, the saturation filed, thicknesses of the bottom and top magnetic layers, respectively. The value of J_1 of the trilayer with t_N = 1.8 nm annealed at is estimated to be –0.12 erg/cm^2 from M_s = 1075 emu/cc, H_s = 550 Oe, t_1 = 5 nm and t_2 = 3 nm. The antiferromagnetic interlayer coupling disappears once for the Ag thicknesses of t_N = 2.4–3.0 nm, the appears again for t_N = 3.2 and 3.4 nm. Thus, the antiferromagnetic interlayer coupling oscillates for the Ag spacer layer thickness as well as the other systems with conventional materials [5][6][7]. Figure 4-11

summaries the dependence of H_s and M_r/M_s on the annealing temperature. The oscillation of the antiferromagnetic interlayer coupling is clearly seen. The antiferromagnetic interlayer coupling was not degraded for t_N = 2.0 nm and 3.2 nm by the annealing at 500 °C, but degraded for t_N = 1.8 nm as indicated in the increase of M_r/M_s to 0.5 from 0.25. The degradation of the antiferromagnetic interlayer coupling is thought to be due to the deterioration of the Ag(1.8 nm) spacer layer by the high temperature annealing. The onset of the antiferromagnetic coupling by the annealing may be related to the change in the electronic structure expected from the enhancement of the chemical ordering in the CFAS films. Therefore, the interlayer exchange coupling in CFAS/Ag/CFAS or systems with other Heusler alloys and other spacer materials may have a lot of room to study. If one can explain the correlation between the spin polarization and the interlayer coupling, it would be very interesting.

Although the interlayer coupling is scientifically interesting, it is unwanted in spin-valves. Thus, we chose 5 nm for the spacer layer in this study, where the interlayer coupling is expected to be sufficiently weak. Indeed, a stable antiparallel magnetization is obtained in the spin-valve with 5nm thick Ag spacer layer (Fig. 4-13). Due to the long spin diffusion length of Ag reported to be more than 100 nm [8], the spacer layer thickness of below 5 nm may not influence on the spin relaxation in the Ag spacer layer.

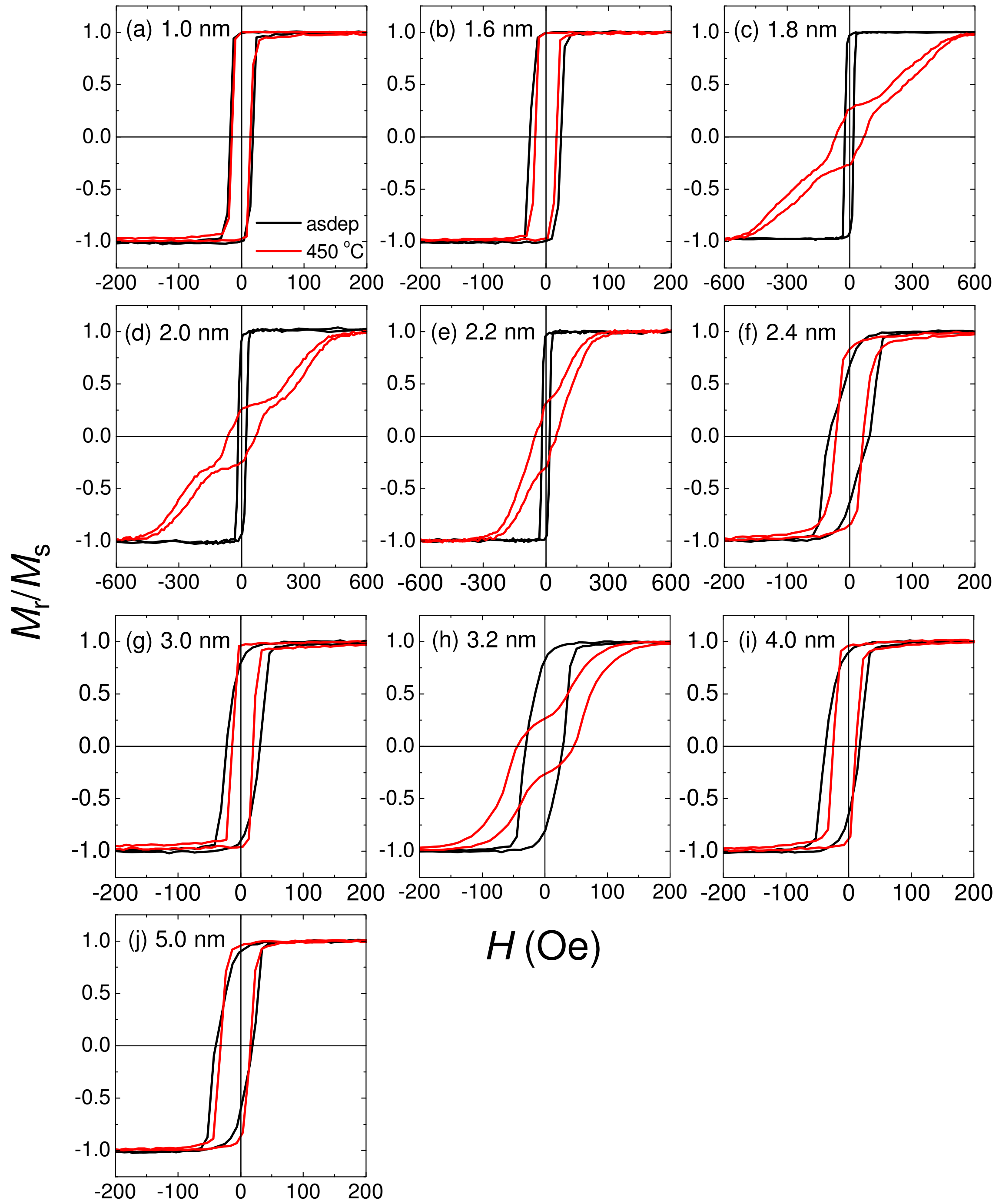

Fig. 4-10 Magnetization curves of CFAS(5 nm)/Ag(t_N)/CFAS(3 nm) trilayers with t_N = 1.0–5.0 nm. (Black) as-deposited and (red) annealed at 450 ℃ for 30 min. The external filed was applied parallel to he CFAS[110] easy axis for the VSM measurements.

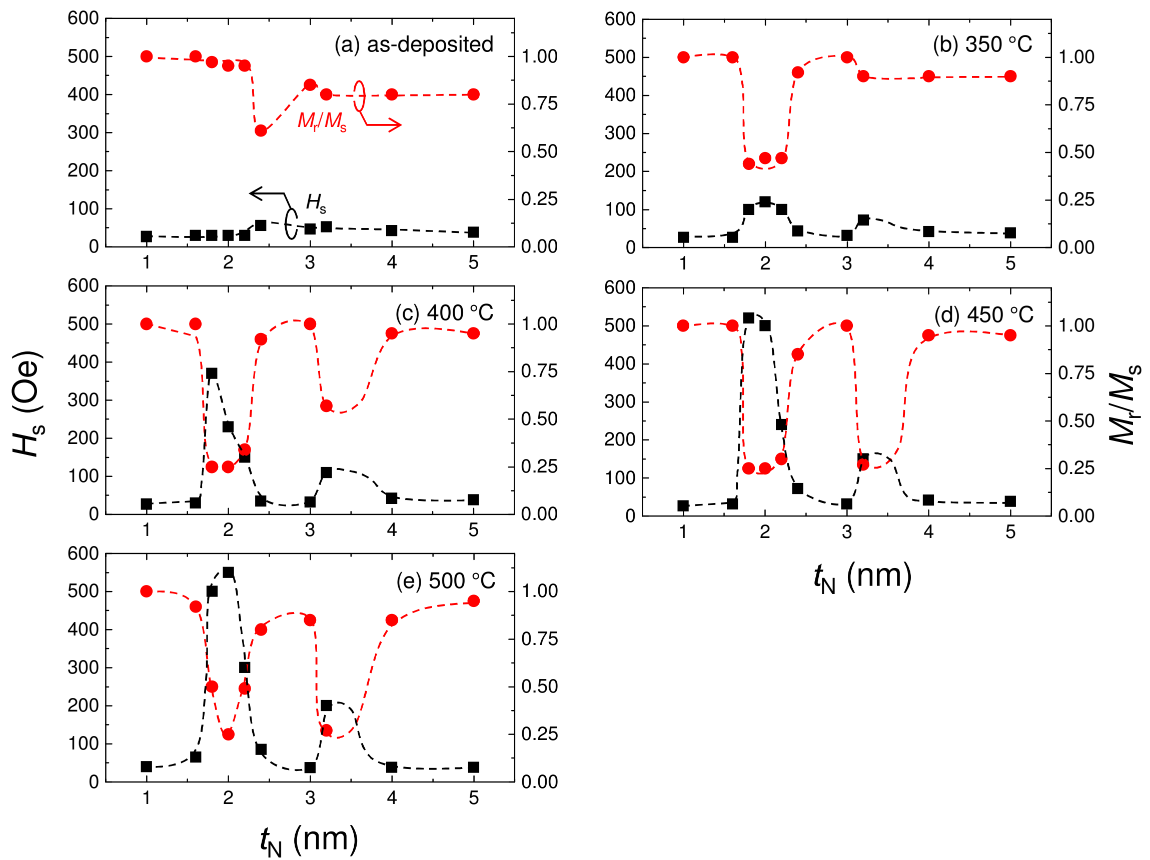

Fig. 4-11 Variations of the saturation field (H_s) (square) and the ratio of the remanence to the saturation magnetization (M_r/M_s) as a function of the Ag spacer layer thickness for various annealing temperatures. M_r/M_s = 0.25 corresponds to the antiparallel magnetization configuration. The broken lines are for guides for eyes.

4.5 Exchange biased spin-valve

4.5.1 Layer and device structures

At the early stage of this study, exchange biased spin-valves were studied. The layer structure is shown in Fig. 4-12. Although the bottom pin type spin-valve with a synthetic antiferromagnet (SyAF) provides the best pinning field as they are used in the practical read heads, the bottom IrMn pinning layer is not preferable for the better growths of the layers on it and the SyAF structure can be degraded by annealing at high temperature which is necessary for the high ordering of the Heusler alloy layers. Thus, we adopted a top pin type spin-valve without a SyAF. A thin $Co_{50}Fe_{50}$ (1 nm) was inserted to enhance the pinning field. In the microfabrication of the CPP-GMR pillar, the Ar ion etching was done until the Ag under appeared, so that the current distribution in the active part for the magnetoresistance (FM/NM/FM trilayer) is well-defined. In addition, the pillar fabrication through the trilayer provides a stable antiparallel magnetization state due to the magnetstatic coupling.

Fig. 4-12 Layer structure of the exchange biased spin-valve.

4.5.2 Magnetization behavior

Figure 4-13(a) shows the magnetization curves of the spin-valves annealed at T_{an} = 300, 400, and 500 °C for 30 min under a magnetic field of 5 kOe. The magnetic field was applied parallel to the CFAS[110] easy axis. For T_{an} = 300 °C, the pinning was not enough so that the magnetization curve did not show a wide plateau range indicating the stable antiparallel magnetization configuration between the free and pinned layers. However, the higher annealing temperatures T_{an} = 400 and 500 °C provided good antiparallel configurations. The dependences of the pinning field by the IrMn layer and the coercivity of the pinned layer are shown in Fig. 4-13(b). The summation of the pinning field and the coercivity of the pinned layer correspond to the field at which the magnetization of the pinned layer starts rotating from the antiparallel state to the parallel state. The pinning field showed the maximum at T_{an} = 400 °C. Since the blocking temperature of IrMn is around 200 °C [9], the magnetic annealing temperature of 300 °C is thought to be sufficient to obtain the exchange bias. The reason of the necessity of the higher annealing temperature is not clear at the present. The change

interfacial structure at the interface between CoFe and IrMn layers could be the origin of the stronger pinning for T_{an} > 400 °C. For T_{an} = 500 °C, the pinning field decreased and coercivity of the pinned layer increased compared to that annealed at T_{an} = 400 °C, which may originate from a interdiffusion of Mn to the pinned layer.

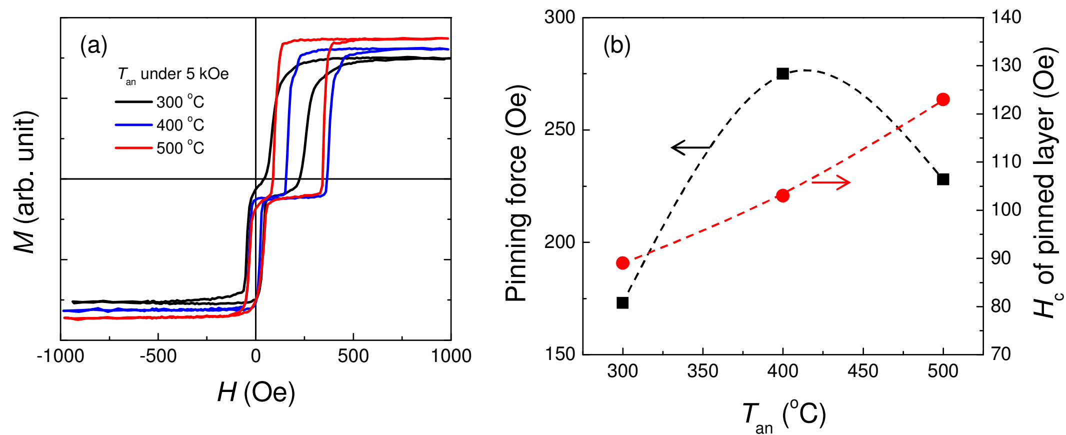

Fig. 4-13 (a) Magnetization curves of the CFAS(5)/Ag(5)/CFAS(5)/CoFe(1)/IrMn(10) spin-valves annealed at T_{an} = 300, 400 and 500 ℃ for 30 min under a magnetic field of 5 kOe. (b) Variations of the pinning field (square) and the coercivity of the pinned layer (circle) for T_{an}.

4.5.3 CPP-GMR property

Figures 4-14 and 4-14 shows the MR curve of the spin-valve annealed at T_{an} = 500 °C measured at room temperature. The pinning direction is parallel to the negative external field. The value of ΔRA was 6.9 m$\Omega\mu$m^2 and the MR ratio was 20.8%. This value of ΔRA is much higher than those obtained with the conventional FM materials of less than 2 m$\Omega\mu$m^2 for the FM layer thickness of 5 nm [10].

The feature of the magnetization configuration in the MR curve is different from that in the magnetization curve for the unpatterned film. First, for the field sweep from the negative to the positive the antiparallel magnetization state is stable up to 900 Oe, which is much larger than that in the magnetization curve of 350 Oe. Second, for the filed sweep from the positive to the negative, the antiparallel magnetization configuration only appears after crossing the zero bias, whereas the pinned layer rotates at +100 Oe in the unpatterned field due to the exchange bias. These features in the fabricated pillar may be due to the magnetostatic coupling between the free and pinned layers with the nearly identical magnetic moments and the larger coercivity in patterned

films.

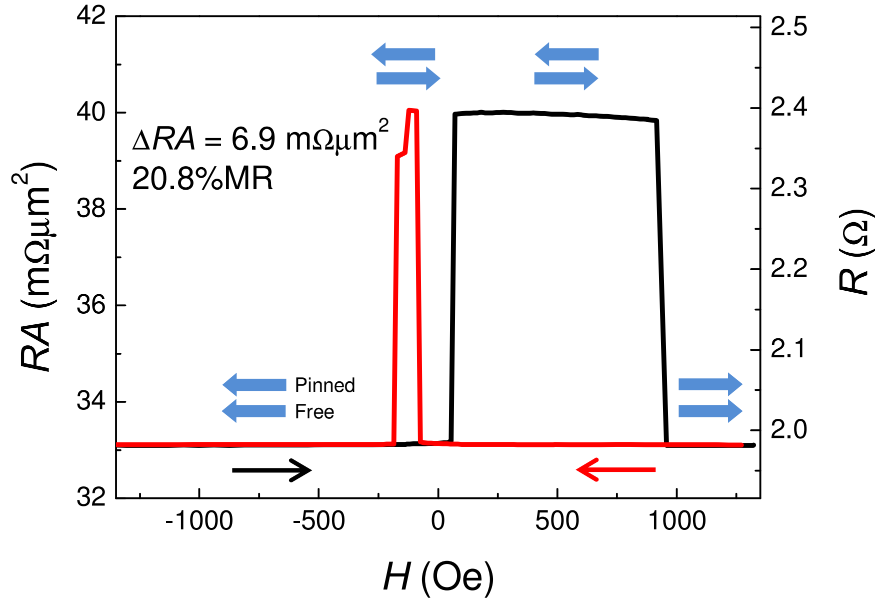

Fig. 4-14 CPP-GMR curve at room temperature of the CFAS(5)/Ag(5)/CFAS(5)/CoFe(1)/IrMn(10) spin-valve annealed at 500 ℃. The device size is 0.1 μm×0.2 μm elliptical.

4.6 Pseudo spin-valve

4.6.1 Necessity of pseudo spin-valves

The main purpose of this thesis is to study the spin-dependent scattering of CPP-GMR using Heusler alloy FM layers. Although we have obtained the MR curves showing the well-defined parallel and antiparallel magnetization states using the exchange biased spin-valves as shown in the previous subsection, there is an inconveniences for the experiments. This is because we need to measure ΔRA from various devices with different FM layer thicknesses so that the contributions of the bulk and interfacial spin-dependent scatterings are separated. For exchange spin values, it is not possible to change the thickness of the pinned layer in a wide range due to the difficulty of pinning thick layers. On the other hand, pseudo spin-valve (PSV) structure composed of FM(t_{F1})/NM/FM(t_{F2}) trilayer surrounded by NM lead electrodes is preferable due to the following reasons,

(i) Analysis by the Valet-Fert model is easier for symmetric spin-valves with $t_{F1} = t_{F2}$.

(ii) The outer interfaces of NM-lead/FM also contribute to the CPP-GMR as the Valet-Fert model assumes an FM/NM multilayer. Therefore, both the NM leads should be the same material.

Even without the exchange bias, the antiparallel magnetization state can be obtained by using the magnetostatic (dipole) coupling between the upper and the bottom FM layers in microfabricated pillars. Therefore, we have shifted to study the CPP-GMR properties using the PSVs.

4.6.2 Layer and device structures

The layer structure of the pseudo spin-valve is MgO substrate/Cr (10 nm)/Ag (100 nm)/CFAS (t_F)/Ag (5 nm)/CFAS (t_F)/Ag (5 nm)/Ru (8 nm). The thicknesses of the top and bottom CFAS layer were same. The devices with different t_F (2.5–22 nm) were fabricated. After all the sputtering processes, the films were *ex-situ* annealed at T_{an} = 250–550 °C for 30 min under a magnetic field of 5 kOe in a vacuum chamber (base pressure ~1×10^{-4} Pa). There is no special reason to apply the magnetic field, simply because the annealing furnace equipped a permanent magnet for magnetic annealing. After the annealing, the films were patterned into pillars. Elliptical shape (major axis : minor axis = 2:1) was chosen for the pillars to make a shape anisotropy. The etching of the pillar was done until the Ag underlayer appeared.

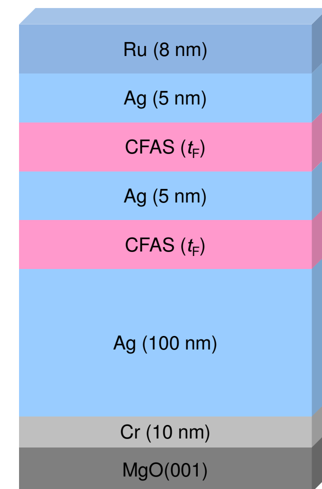

Fig. 4-15 Layer structure of the pseudo spin-valve.

4.6.3 TEM observation

Figure 4-14 shows the cross-sectional high resolution TEM image of the pseudo spin-valve with the CFAS(8 nm)/Ag(5 nm)/CFAS(8 nm) trilayer annealed at 500 °C. The interface between the CFAS layer and the Ag spacer layer is atomically flat and the contrast is very sharp. This indicates that the intermixing between two layers is negligible. Since an intermixing or an interfacial alloying can induce an electron scattering at the interface which is independent of the spin direction, the very sharp interface is important to obtain a large spin-dependent scattering at the interface. The chemical order of the CFAS layer was examined by taking a microbeam diffraction pattern as shown in the inset of Fig. 4-14. Only the fundamental and the B2 superlattice

spots are seen, thus the CFAS layer is B2 ordered. This is consistent with the XRD results measured in the CFAS(10 nm) films (Figs. 4-3 and 4-4).

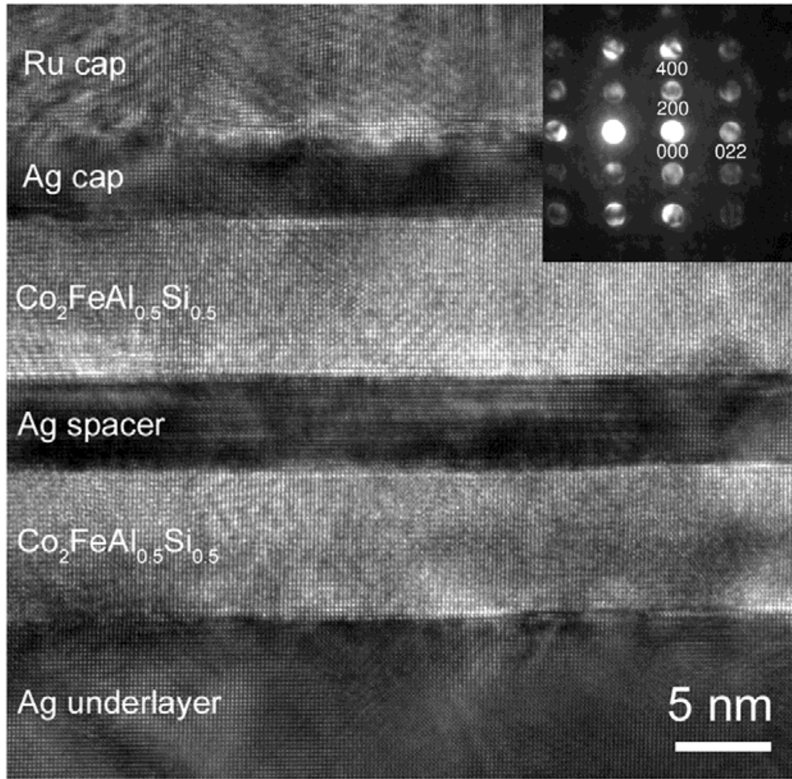

Fig. 4-16 Cross-sectional high resolution TEM image of CFAS(8 nm)/Ag(5 nm)/CFAS(8 nm) pseudo spin-valve. Inset is the microbeam diffraction pattern taken from the CFAS layer.

4.6.4 Microfabrication: measurement of the pillar size

The actual pillar sizes were measured by scanning electron microscopy (SEM) for all the samples. Figure 4-17 shows the SEM micrographs of the reference pillars fabricated for the SEM observation. The film was for the PSV devices of the CFAS(2.5)/Ag(5)/CFAS(2.5) trilayer. At least 10 reference pillars were observed for each size and the areas were measured as shown in Table 4-2. For all of the sizes of the pillars, the scattering of the size was smaller than 10%. Thus, the microfabrication process was sufficiently reliable for these device sizes. As a general tendency, pillars smaller than ~100 nm become bigger than those designed, which is probably due to the overdose of the EB exposure. The deviation of the pillar size from the design depends

also on the condition of the development of the resist. Therefore, measuring the actual size for all the sample is important to obtain reliable data. In this work, the resistance–area product (*RA*) was calculated using the measured *A*.

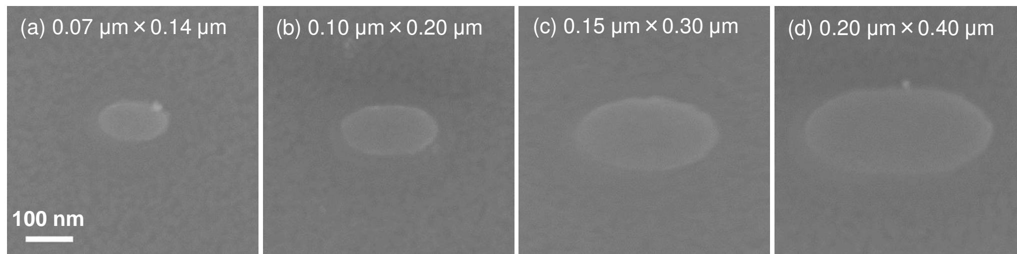

Fig. 4-17 SEM micrographs of microfabricated pillar after the lift-off of the SiO_2 insulation layer (Fig. 3-4 step(7))

Pillar design (μm×μm)	Designed *A* (μm^2)	Actual *A* (μm^2)
0.07×0.14	0.0077	0.0090±0.0005
0.10×0.20	0.0157	0.0157±0.0007
0.15×0.30	0.0353	0.0340±0.0007
0.20×0.40	0.0628	0.0570±0.007

Table 4-2 SEM micrographs of microfabricated pillar after the lift-off of the SiO_2 insulation layer (Fig. 3-4 step(7))

4.6.5 CPP-GMR property

This subsection describes the typical CPP-GMR properties of the CFAS/Ag/CFAS pseudo spin-valves with the CFAS thickness t_F = 2.5 nm and 20 nm. The films were annealed at 500 °C for 30 min after the completion of the all of the sputtering processes. The dependences of Δ*RA* on the annealing temperature and on the CFAS thickness will be describes in 3.5.5 and Chapter 4, respectively for the pseudo spin-valves.

Subtraction of the lead resistance

The measured resistance for the pillars contains a parasitic resistance whose value is independent of the area of the pillar. This is perhaps due to the curvature of the

current near the ends of the pillar as shown by the simulation (3.2.2). The value can be obtained by plotting the device resistance R for the inverse area $1/A$ as shown in Fig. 4-18(a). The value of the parasitic lead resistance can be estimated by extrapolating the R-$1/A$ relationship into $1/A \rightarrow 0$. A finite resistance remains even for the pillar with infinitely large size, which corresponds to the lead resistance. Moreover, the linear R-$1/A$ relationship may guarantee the homogeneous current distribution in the pillars, because R should shift to higher value for large pillars if there is a current crowding. The value of the lead resistance at each measurement temperature was obtained as follows. For the precise estimation of the lead resistance, it is necessary to measure the resistance for a lot of devices and take the statics of the values. However, the number of devices to be measured is limited by the limitation of the measurement system. Thus, the resistance of the devices was measured for three devices with different sizes, and the ratio of the change of the device resistance was taken as a function of the measuring temperature as shown in Fig. 4-17(b) and (c).

The subtraction of the parasitic lead resistance is justified by as follows. The value of RA should be independent of A as long as the current distribution in the pillar is homogeneous. However, RA obtained by the raw device resistance and the device area linearly increased with A as shown in Fig. 4-18(d). This is because the raw resistance contains the parasitic resistance independent of A. On the other hand, the value of RA after subtracting the parasitic lead resistance is constant for all the value of A. The subtraction of the lead resistance is also important to discuss the measuring temperature dependence of the values of RA for the parallel and the antiparallel magnetization configurations.

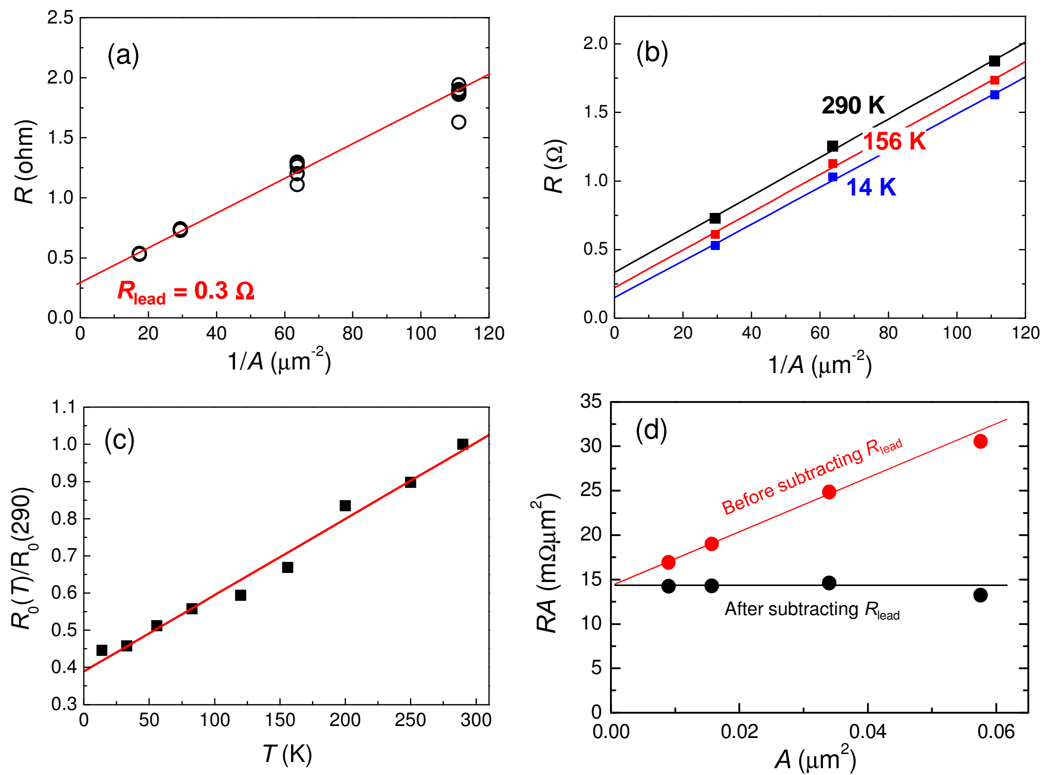

Fig. 4-18 (a) R–$1/A$ plot. The intercept value corresponds to the parasitic lead resistance independent of the pillar size. (b) Estimation of the parasitic resistance at each measurement temperature. (c) Temperature dependence of the parasitic lead resistance. (d) The subtraction of the lead resistance gives a constant RA independent of the pillar size (black).

CPP-GMR property of the PSV

Figure 4-19 and 4-20 show the MR curves of the PSVs with the CFAS layer thickness of t_F = 2.5 nm and 20 nm, respectively measured at low temperature (14 K or 19 K) and room temperature (290 K). The difference of the temperature for the low temperature measurement was simply because of the instability of the cooling power of the helium refrigerator. However, since ΔRA is nearly temperature independent at below 30 K as shown later, the difference in temperature does not matter for the experiments and the interpretations of the physics.

The typical feature of the MR curve in the PSV dependent on the ferromagnetic layer thickness is shown. For the PSV with thin ferromagnetic layers, the magnetostatic coupling is not strong enough to align the magnetization configuration to antiparallel in the absence of external field. Thus, when the external field is swept from the negative field to the positive field or vice versa, the magnetization configuration remains parallel

until crossing the zero field. After crossing the zero field and the sign of the external field has changed, the magnetization of one FM layer with a lower coercivity switches to another. Then, the antiparallel magnetization state becomes stable due to the magnetostatic coupling In the device with t_F = 2.5 nm shown in Fig, 4-19, the magnetization reversal appears at ~ 10 Oe and the antiparallel state was stable up to 130 Oe of the external field. It is not clear which ferromagnetic layer (upper or bottom) has a lower coercivity and thus rotates first. Presumably, the difference of the coercivity originates from a difference of the crystallinity of the layers, namely the bottom ferromagnetic layer is deposited on the annealed thick Ag underlayer with a high crystallinity, whereas the upper layer is deposited on thin Ag spacer layer which has not been annealed. The field at which the magnetization of the one ferromagnetic layer switches depends on temperature because the coercivity generally increases with decreasing temperature. One the other hand, in devices with thick ferromagnetic layers, the magnetostatic coupling is strong so that the magnetization configuration under the absence of an external field is antiparallel. Therefore, when the external field is swept from a strong negative (or positive) field, the magnetization rotation happens before crossing the zero field as shown in Fig. 4-18 for t_F = 20 nm.

The PSV with t_F = 2.5 nm showed ΔRA of 5.1 m$\Omega\mu$m^2 and 11.4 m$\Omega\mu$m^2 at 290 K and 14 K, respectively. The MR ratios were 26% and 70% at 290 K and 14 K, respectively for the raw measured data including the lead resistance estimated to be 0.3 Ω at 290 K and 0.13 Ω at 14 K. In order to more accurate MR ratio of the trilayer which is the active part for the MR, the lead resistance was subtracted. Then the MR ratios were 34% at 290 K and 80% at 14 K. Both ΔRA and the MR ratio using the CFAS FM layers showed much larger values compared to those with the conventional FM materials. For example, PSVs with 2.5 nm $Co_{50}Fe_{50}$ FM layers and a Ag spacer layer were fabricated and the values of ΔRA were 2.1 m$\Omega\mu$m^2 at 290 K and 3.0 m$\Omega\mu$m^2 at 14 K.

The PSV with t_F = 20 nm showed ΔRA of 5.1 m$\Omega\mu$m^2 and 11.4 m$\Omega\mu$m^2 and the MR ratio after subtracting the lead resistances of 22% and 49% at 290 K and 14 K, respectively. The enhancement of ΔRA compared to the PSV with t_F = 2.5 nm is thought to due to the contribution of the bulk scattering. On the other hand, however, the MR ratio of the device with t_F = 20 nm was much lower than that with t_F = 2.5 nm both at LT and RT. This is because the range of the CFAS film which contributes to the bulk scattering is much a thinner thickness than 20 nm, in other words, the enhancement of ΔRA has been saturated at a thinner thickness. The analysis of the spin-dependent

scattering in the CFAS/Ag/CFAS PSVs is discussed in Chapter 5 in detail.

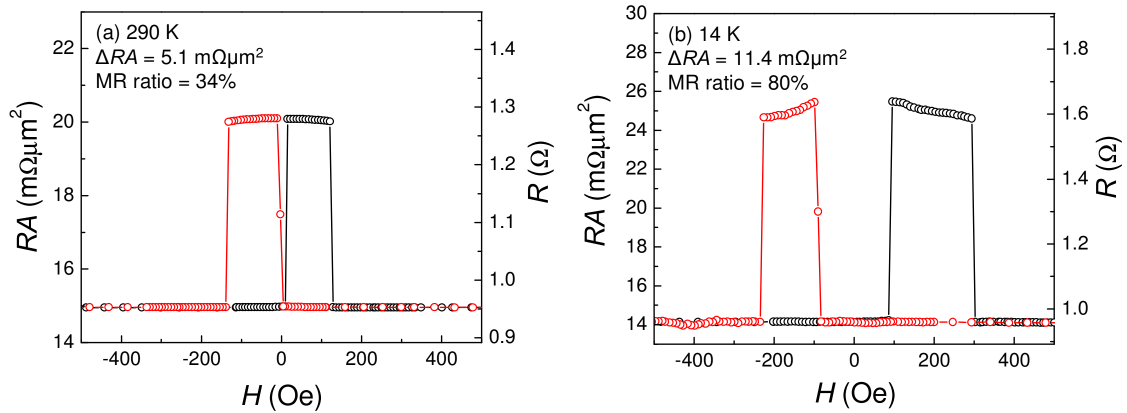

Fig. 4-19 CPP-GMR curves of the CFAS(2.5 nm)/Ag(5 nm)/CFAS(2.5 nm) pseudo spin-valve measured at (a) 290 K and (b) 14 K. The lead resistance has been subtracted.

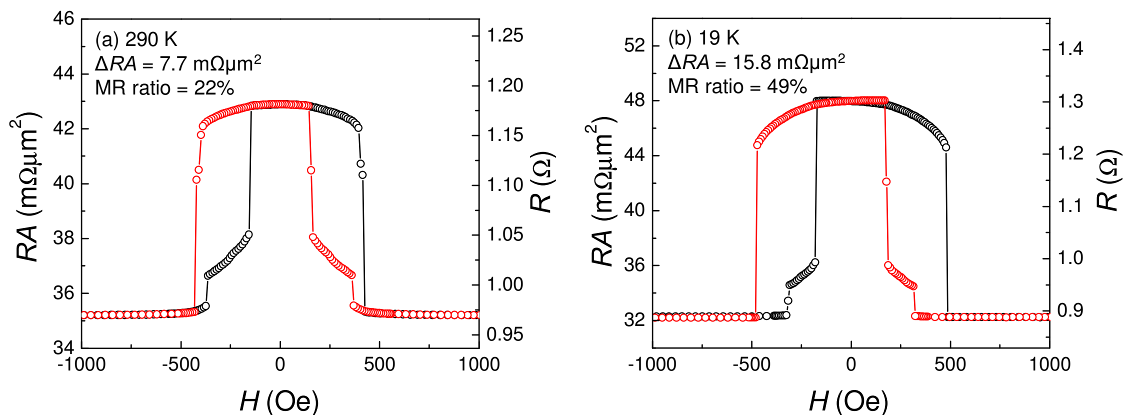

Fig. 4-20 CPP-GMR curves of the CFAS(20 nm)/Ag(5 nm)/CFAS(20 nm) pseudo spin-valve measured at (a) 290 K and (b) 19 K. The lead resistance has been subtracted.

The temperature dependences of RA for the parallel (RA_P) and the antiparallel (RA_{AP}) magnetization state and that of ΔRA are shown in Fig. 4-21 for the PSV with t_F = 2.5 nm. The lead resistance was subtracted for each measurement temperature. The features of the temperature dependences were almost same for all the CFASF/Ag/CFAS PSVs regardless of the CFAS layer thickness t_F. RA_P showed a small temperature dependence of RA_P(290 K)/RA_P(14 K) = 1.06, which roughly corresponds to the temperature dependence of the resistivity of the CFAS film shown in 4.3.3. Although

there should be some additional boundary resistance resulting from the spin accumulation as discussed in Chapter 2, the value for the P state is thought to be negligibly small. On the other hand, RA_{AP} decreases with increasing temperature. This may be due to the decrease of the boundary resistance spin accumulation due to the reduction of the spin-dependence of the scattering. Thus, ΔRA ($=RA_{AP} - RA$) decreases with increasing temperature.

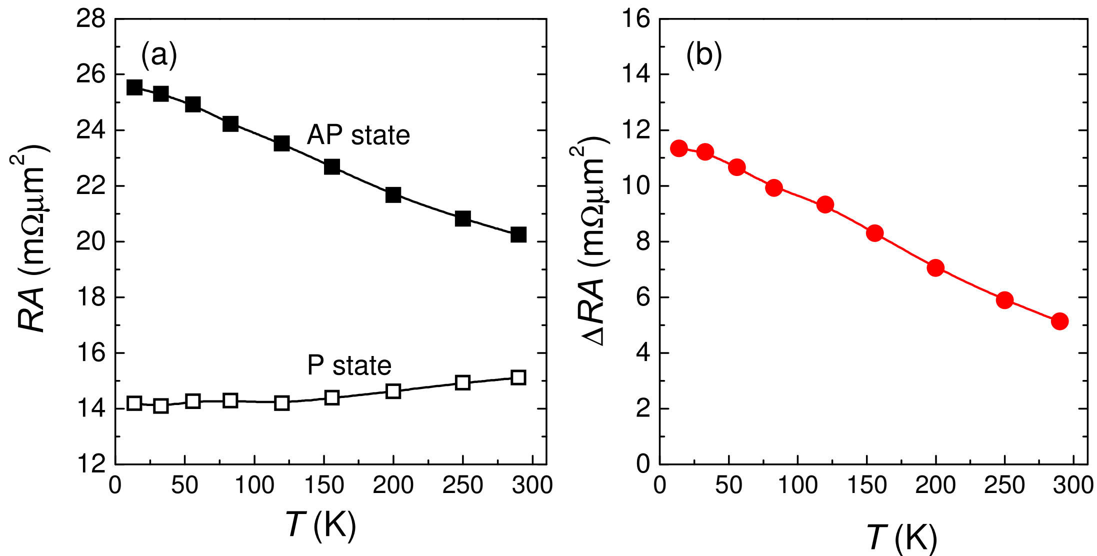

Fig. 4-21 Temperature dependence of (a) *RA* of P and AP states and (b) Δ*RA* CFAS(2.5 nm)/Ag(5 nm)/CFAS(2.5 nm) pseudo spin-valve. The lead resistance has been subtracted.

4.6.6 Dependence of Δ*RA* on the annealing temperature

The dependence of ΔRA on the annealing temperature was investigated for the PSVs with the CFAS layer thickness of t_F = 2.5 nm. The devices were annealed at T_{an} = 250–550 °C and the CPP-GMR properties were measured at various temperatures from ~15K to 290 K. Figure 4-20(a) shows the variation of ΔRA at 290 K as a function of the annealing temperature. The devices annealed at T_{an} = 250 °C showed ΔRA = 1.3 mΩμm^2, which is lower than that of a device using CoFe (2.5 nm) as the ferromagnetic layers of 2.1 mΩμm^2. However, ΔRA enhanced with increasing the annealing temperature. The enhancement of ΔRA shows a good correspondence with the enhancements of the magnetization and the degree of B2 order measured for 10 nm thick CFAS films deposited on the Cr/Ag underlayer as shown in Fig. 4-20(b). Thus, the enhancement of the B2 order improves the CPP-GMR with CFAS and Ag. It is also worth mentioning

that the chemical ordering can improve by annealing even in the very thin film of 2.5 nm, although it is difficult to directly measure the degree of order in the very thin films by XRD. The enhancement of the CPP-GMR according to the improvement of the chemical ordering is consistent with the tunnel magnetoresistance using CFAS electrodes [11],[12].

The dependence of ΔRA on the measurement temperature for the devices annealed at the various temperatures is summarized in Fig. 4-21. For comparison, the data in the PSV with CoFe(2.5)/Ag(5)/CoFe(2.5) is shown together. Interestingly, the variation of ΔRA normalized by the values at 15 K is almost identical for all the PSVs with the CFAS layers but with the different annealing temperatures, *i.e.* the value of ΔRA decreases to less than the half from 15 K to 290K regardless of the annealing temperature. This means that the temperature dependence of ΔRA is regardless of the degree of the chemical order of the CFAS alloy. Thus, it is likely that the large temperature dependence of ΔRA of the devices with the CFAS layers are related not to the spin polarization but to the composition only. This may be an important point to clarify the origin of the temperature dependence of ΔRA. On the other hand, the temperature dependence of ΔRA of the device with the CoFe layers was much smaller: ΔRA decreased by 30% between 15 K and 290 K. These experimental results may indicate that the large temperature dependence of the CPP-GMR output (ΔRA) is not related to the high spin polarization in the well-ordered structure.

Such a large temperature dependence of MR has been reported for tunnel magnetoresistance (TMR) with AlO_x or MgO barriers. Also in the case of the TMR devices, the physical origin of the large temperature dependence is not very clear. The most likely mechanism would be a decrease of the exchange energy of the Heusler alloy at the interface with the barrier, thus the magnetization tends to tilt from the magnetization of the bulk of the film. Such a noncolinear magnetization at the interface is a mixture of the up and down spin states, which can induce a tunneling of an interfacial scattering.

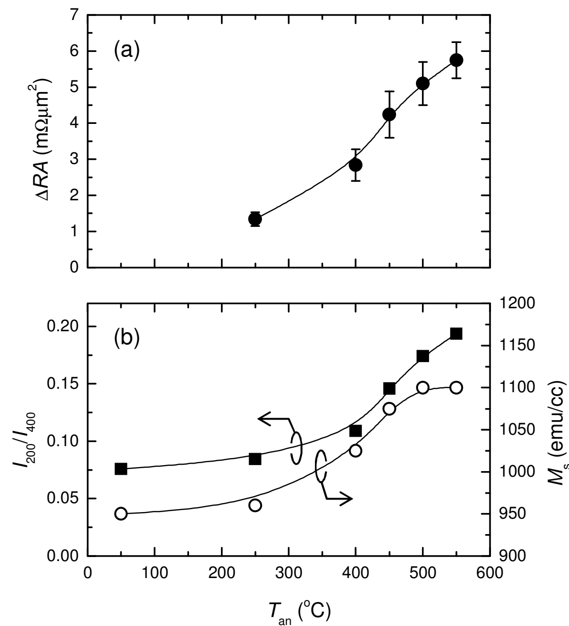

Fig. 4-22 Dependences of (a) Δ*RA* and (b) the degree of B2 order and the magnetization on the annealing temperature. Δ*RA* is for the CFAS(2.5 nm)/Ag(5 nm)/CFAS(2.5 nm) pseudo spin-valve. The degree of order and the magnetization are for the CFAS(10 nm) film on the Cr/Ag underlayer (the same as shown in Fig. 4-4, 4-6).

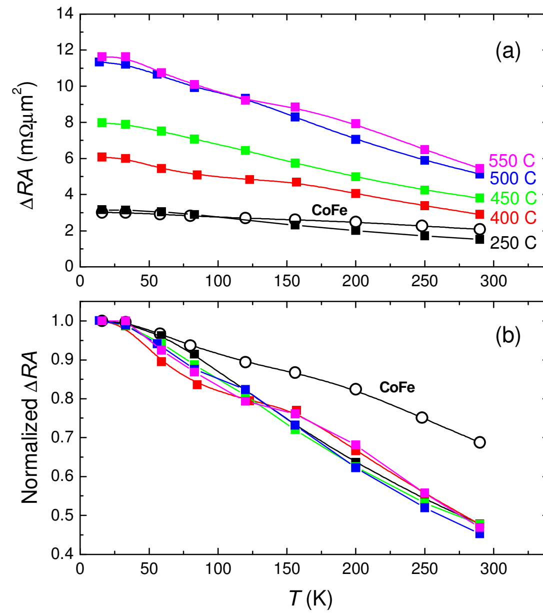

Fig. 4-23 Dependences of (a) Δ*RA* and (b) the degree of B2 order and the magnetization on the annealing temperature. CPP-GMR is for the CFAS(2.5 nm)/Ag(5 nm)/CFAS(2.5 nm) pseudo spin-valve. The degree of order and the magnetization is for the CFAS(10 nm) film on the Cr/Ag underlayer (the same as shown in Fig. 4-4, 4-6).

4.7 Effect of sense current density

The sense current density is essential for CPP-GMR devices both fundamentally and practically. In CPP-GMR trilayer or multilayer, electron propagating from one ferromagnetic layer applies a spin torque to the other ferromagnetic layers. When the current density exceeds a critical value which is determined by the damping parameter of the ferromagnetic materials as so on, the magnetization of the ferromagnetic layer is destabilized. This causes a reduction of the CPP-GMR output (ΔRA), a deterioration of the linear response of the read sensor or a noise [13][14]. Since the sensor output is given by $\Delta RA \times J$, where J is the sense current density, a high critical sense current density of the appearance of the spin torque effect is required for the read head application.

The spin torque effect in CPP-GMR spin-valve has been reported by Maat *et al* [15]. The sample structure is substrate/underlayer/IrMn/$Co_{50}Fe_{50}$(2.5)/Ru(0.7) /$Co_{50}Fe_{50}$(2.5)/Cu(4)/$Co_{50}Fe_{50}$(0.7)/$Ni_{86}Fe_{14}$(4)/Ru (thickness in nm). Figure 4-24 shows the MR curves for different sense current densities. The negative value of the sense current is defined to be the electron flow from the free layer to the reference (pinned) layer. The sense current of -4×10^7 A/cm^2 destabilizes the parallel magnetization state due to the reflected electron by the reference layer. On the other hand, by the positive current of $+2\times10^7$ A/cm^2, the electron from the reference layer destabilizes the free layer in the antiparallel (AP) states by. Thus, the onset of the magnetization destabilization shows a large asymmetry on the current polarity when the magnetization of one of the magnetic layers is strongly pinned by exchange bias. They reported the critical sense current density of the onset of the spin torque induced magnetization instability to be -3×10^7 A/cm^2 and $+1\times10^7$ A/cm^2. In a practical point of view, the critical sense current is not high enough to obtain the sensor output (see Fig. 1-10). Thus, suppressing the onset of the spin torque induced magnetization instability is necessary. Maat *et al.* demonstrated that Dy capping layer on the $Ni_{86}Fe_{14}$ free layer has effectively increase the critical current density to -5×10^7 A/cm^2 and $+2\times10^7$ A/cm^2, which is thought to be due to a spin pumping effect by the Dy layer [15].

In this work, the effect of the sense current density on the CPP-GMR property was measured for the exchange biased spin-valve and the pseudo spin-valve devices annealed at 500 °C. For the measurements, dc sense current was applied with various current.

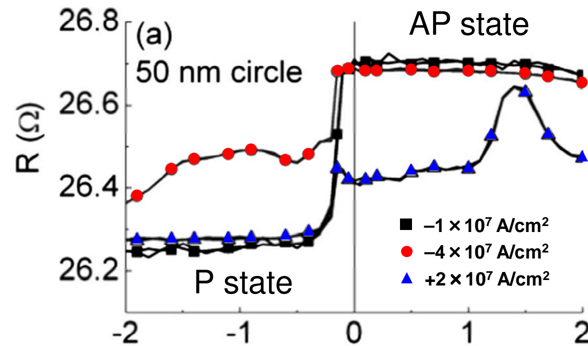

Fig. 4-24 MR curves of IrMn/CoFe/Ru/CoFe/Cu/CoFe/NiFe/Ru spin-valves. The electron flow direction is from the free layer to the pinned layer for the negative current. The negative current destabilizes the parallel (P) state, while the positive current destabilizes the antiparallel (AP) state. By Maat et al. [15].

4.7.1 Exchange biased spin-valve

The spin-valve device with the layer structure of MgO(001)/Cr(10 nm)/Ag(100 nm)/CFAS(5 nm)/Ag(5 nm)/CFAS(5 nm)/CoFe(1 nm)/IrMn(10 nm)/Ru(8 nm) was employed to examine the effect of spin torque. First, it should be noted that he effect by the current flowing in the pillar on the magnetic layer is not only the spin torque but also the induced magnetic field (Oersted field) and the Joule heating. The current creates a vortex-like magnetic in the pillar. The intensity of the field is the strongest at the edge of the pillar and zero at the center of the pillar. Figure 4-25 shows the distribution of Oersterd field in a pillar with a cross-section of 50 nm×50 nm simulated by Meguro *et al*. [16]. Such an Oersted field degrades the antiparallel magnetization configuration at the edge of the pillar, thus decreases ΔRA. The Joule heating may induce a reduction of the coercivity of the magnetic layer and the reduction of ΔRA due to the smaller spin-dependent scattering with increasing temperature. The increase of temperature by the Joule heating can be estimated by the increase of the device resistance in principle.

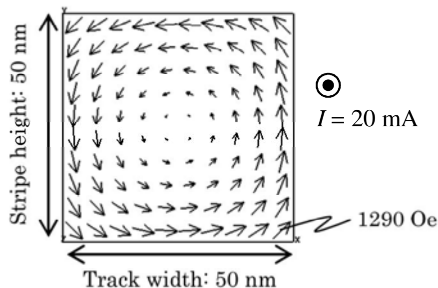

Fig. 4-25 Distribution of Oersted field in a pillar of 50 nm square by a current of 20 mA. Ref. [16].

In order to discuss these three effects by the sense current, devices with different sizes were examined. The designed sizes were 0.07 μm×0.14 μm and 0.15 μm×0.30 μm and the actual device area measured by SEM observations were A = 0.010 μm^2 and 0.036 μm^2, respectively. Figures 4-26 and 4-27 show the MR curves of these two devices with different sense current. The pinning direction is to the negative field, the external field was swept from negative to positive. In the device with A = 0.010μm^2, the behavior of the MR curve changed with different sense currents. Briefly, the resistance change (ΔR) decreased and the squareness of the MR curve was degraded with increasing sense current. In Fig. 4-26(a), where the electron flow from the pinned layer to the free layer, the resistance shows a plateau from 0 to +1000 Oe corresponding to the antiparallel magnetization state for the smallest sense current of 0.1 mA. When a sense current of 2 mA (corresponding to current density $j = 2\times10^7$ A/cm^2) is applied, the resistance of the device shows an irregular change at the small external field in the antiparallel state. This is because of the instability of the antiparallel state by current. For the opposite current polarity shown in Fig. 4-26(b) (electron flows from the free layer to the pinned layer), the parallel magnetization is destabilized so that the switch field from AP to P becomes large in the negative field. These features of the current polarity on the destabilization of the magnetization state are qualitatively consistent with the results by Maat *et al.* shown Fig. 4-24. However, due to the weak pinning field of ~250 Oe (see 4.4.2), the effect of the current polarity was not very clear and the scattering of the behavior from device to device was somehow large. Thus, we do not discuss the current polarity effect on the spin torque in detail.

In order to study whether the effect of current on the manner of the MR curve was by the induced Oersted field or not, let us see MR curves of a device with the same layer structure but a larger device size as shown Fig. 4-27. The device is almost 4 times larger than that shown in Fig. 4-26. The amplitude of the induced field is thought to be determined by the current not by the current density. In this device, the shape of the MR curve for the electron current from the free layer to the pinned layer (Fig. 4-27(b)) did not change even at the sense current of 10 mA. Moreover, the effect of the Oersted field should not depend on the current polarity. Thus, the change of the MR curve in the smaller device (Fig. 4-22) by the currents higher than 2 mA may not be due to the induced field.

Next concern is whether the reduction of ΔR is due to the Joule heating or not. The resistance of the device in P state slightly increased with increasing current, indicating that the temperature in the pillar might increase for some extent due to the

Joule heating. However, the increase of temperature should decrease the coercivity of the magnetic layers and decrease the spin-dependence of the scattering, which induce a change of the switching field of the free and pinned layers and a reduction of ΔR. Thus, it is unlike that the irregular change of the resistance by the sense currents higher than 2 mA shown in Fig. 4-22 is attributed to the Joule heating.

By the discussions above, the destabilization of the AP state by current is thought to be by the spin torque. Indeed, the electron flowing from PL to FL destabilizes the AP state by the spin torque from PL to FL. On the other hand, for the electron current polarity from FL to PL, the switching field from P state to AP state becomes larger in the negative external field. This may be because the electron reflected by the PL/Ag spacer interface gives a spin torque to the FL, which tries to switch the FL. The onset of the spin torque effect was by the current higher than 2 mA for the device with A = 0.010 μm^2, thus the critical current density of the spin torque in the CFAS/Ag/CFAS device was j_{crit} = 2–3×10^7 A/cm^2, which is comparable to those in devices with conventional CoFe or NiFe magnetic layers [15], [17].

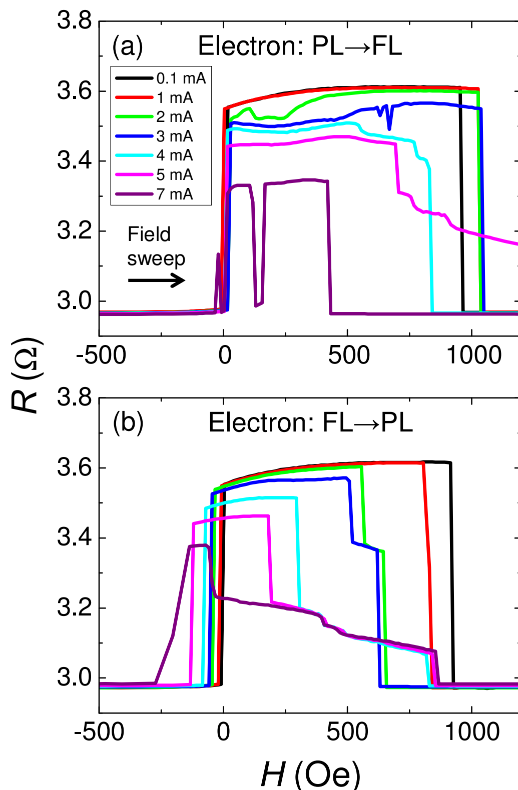

Fig. 4-26 MR curves with various sense current of CFAS(5 nm)/Ag(5 nm)/CFAS(5 nm) spin-valve. The device area was A = 0.010 μm^2. The electron flow direction was (a) from the pinned layer (PL) to the free layer (FL) (b) from the free layer to the pinned layer.

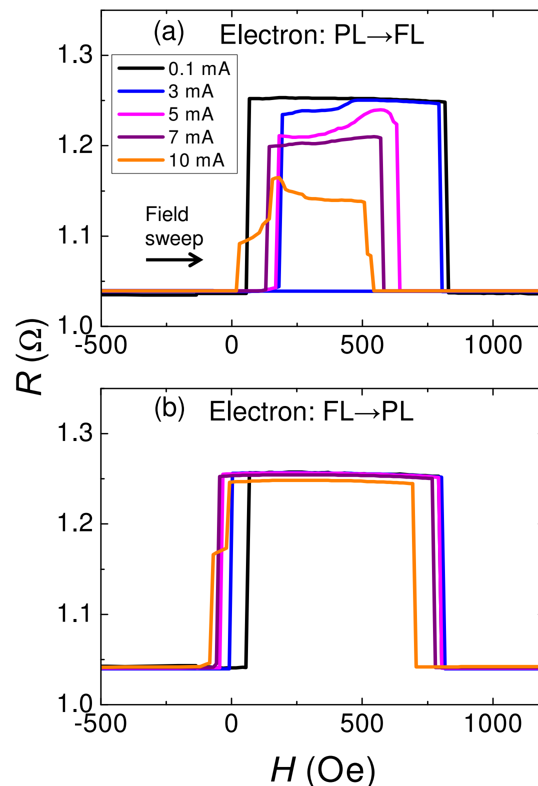

Fig. 4-27 The same measurements as those in Fig. 4-26 for a device with A = 0.036 μm^2.

4.7.2 Pseudo spin-valve

The effect of the spin torque was examined for the pseudo spin-valve with 2.5 nm thick CFAS layers. The MR curves measured with sense currents (0.1–5 mA) are shown in Fig. 4-28. The device area was A = 0.009 μm^2. The switching field from P to AP (shown by arrows in figure) became larger in the negative field with increasing sense current even by 2 mA (j = 2.2×10^7 A/cm^2). This is attributed to the spin torque which destabilizes the P state. At 3 mA corresponding to j = 3.3×10^7 A/cm^2, the MR curve showed a unique behavior. When the external field is swept from negative to positive, the resistance dropped at around zero field once and recovers to the AP state again at +70 Oe. This may mean that there is some intermediate state (neither P nor AP), possibly spin torque oscillation state is realized. Since this MR measurement is a static test by applying dc bias current and measuring the resistance averaged during a time constant, the spin torque oscillation cannot be examined. An ac measurement with a frequency resolution will reveal what is happing in the intermediate state.

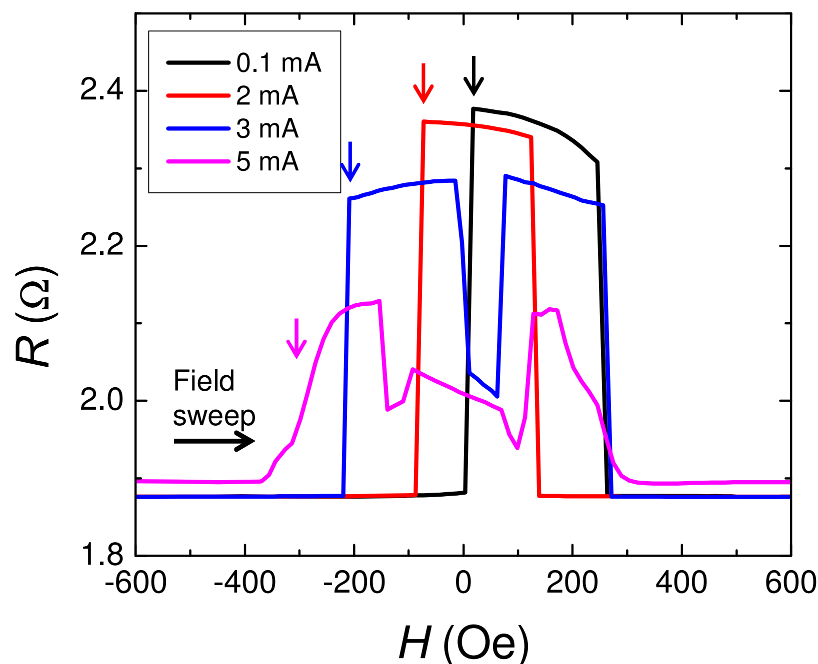

Fig. 4-28 MR curves of CFAS(2.5 nm)/Ag(5 nm)/CFAS(2.5 nm) pseudo spin-valves (A = 0.009 μm^2) measured at room temperature with various sense currents. The arrows indicate the switching from P state to AP state.

4.8 Summary of this chapter

This chapter described the fabrications of thin films and CPP-GMR devices, and the MR properties. The findings and achievements are as follows.

1) The fabrication of process of the Cr(10 nm)/Ag(100 nm) underlayer for a lead electrode was established. An *in situ* annealing at 300 °C for 30 min after the deposition of Ag was effective to obtain flat surface.

2) The B2-ordered $Co_2Fe(Al_{0.5}Si_{0.5})$ (CFAS) film was successfully fabricated on the Ar underlayer with the magnetization close to the value of the Slator-Pauling rule (5.5 μ_B/f.u.). The degree of B2 order enhanced up to S_{B2} ~ 0.7 by annealing at >500 °C.

3) An oscillatory antiferromagnetic interlayer coupling was observed in the annealed CFAS/Ag/CFAS trilayer for the Ag spacer layer thickness t_N=1.8–2.2 nm and ~3.2 nm. The oscillation period of the interlayer exchange coupling was ~1.4 nm. The 5 nm thick Ag spacer layer was thick enough to decoupled the CFAS magnetic layers.

4) The fabrication process of the pseudo spin-valves with various ferromagnetic layer thicknesses ranging from 2.5 nm to 22 nm was established. A large CPP-GMR output was obtained for the devices with very thin CFAS layers of 2.5 nm.
5) The strong correlation between the CPP-GMR output (ΔRA) and the chemical order was shown. The annealing temperature at 250 °C provided ΔRA only 1.3 m$\Omega\mu$m^2 in CFAS(2.5 nm)/Ag(5 nm)/CFAS(2.5 nm) pseudo spin-valve, which was lower than that with $Co_{50}Fe_{50}$ magnetic layers. However, the high temperature annealing at >500 °C enhanced ΔRA up to 5.5 m$\Omega\mu$m^2. The trends of between the annealing temperature and ΔRA showed a good correspondence with that of the degree of B2 order.

6) The temperature dependence of ΔRA was almost independent of the annealing temperature, *i.e.* the ration of ΔRA measured at 15 K to that at 290 K was constant for all the annealing temperature. This may mean that the temperature dependence of ΔRA is governed by the alloy composition itself but by the spin polarization.

7) Spin torque induced magnetization instability was examined by a dc measurement.

The critical current density of the spin torque induced magnetization instability was approximately 2×10^7 A/cm^2.

Next chapter will describe the analysis and discussion of the spin–dependent scattering characteristics of the CFAS/Ag/CFAS trilayer by the Valet–Fert model.

References

[1] T. Furubayashi, K. Kodama, H. Sukegawa, Y. K. Takahashi, K. Inomata, and K. Hono, Appl. Phys. Lett. 93, 122507 (2008).
[2] (textbook written in Japanese) X 線構造解析（材料学シリーズ），早稲田嘉夫・松原英一郎著，内田老鶴圃，1998 年，p.89–91.
[3] W. H. Wang, H. Sukegawa, R. Shan, T. Furubayashi, and K. Inomata, Appl. Phys. Lett. **92**, 221912 (2008).
[4] C. G. F. Blum, C. A. Jenkins, J. Barth, C. Felser, S. Wurmehl, G. Friemel, C. Hess, G. Behr, B. Büchner, A. Reller, S. Riegg, S. G. Ebbinghaus, T. Ellis, P. J. Jacobs, J. T. Kohlhepp, and H. J. M. Swagten, Appl. Phys. Lett. **95**, 161903 (2009).
[5] S. S. P. Parkin, N. More, and K. P. Roche, Phys. Rev. Lett. **64**, 2304 (1990).
[6] S. S. P. Parkin, R. Bhadra, and K. P. Roche, Phys. Rev. Lett. **66**, 2152 (1991).
[7] S. S. P. Parkin, Phys. Rev. Lett. **67**, 3598 (1991).
[8] J. Bass, and W. P. Pratt, Jr., J. Phys.: Condens. Matter **19**, 183201 (2007).
[9] A. J. Devasahayam, P. J. Sides, and M. H. Kryder, J. Appl. Phys. **83**, 7216 (1998).
[10] J. R. Childress, M. J. Carey, M. -C. Cyrille, K. Carey, N. Smith, J. A. Katine, T. D. Boone, A. A. G. Driskill-Smith, S. Maat, K. Mackay, and C. H. Tsang, IEEE Trans. Magn. **42**, 2444 (2006).
[11] N. Tezuka, N. Ikeda, S. Sugimoto, and K. Inomata, Appl. Phys. Lett. 89, 252508 (2006).
[12] N. Tezuka, N. Ikeda, S. Sugimoto, and K. Inomata, Jpn. J. Appl. Phys. 46, L454 (2007).
[13] M. Covington, M. AlHajDarwish, Y. Ding, N. J. Gokemeijer, and M. A. Seigler, Phys. Rev. B **69**, 184406 (2004).
[14] J.-G. Zhu, N. Kim, Y. Zhou, Y. Zheng, J. Chang, K. Ju, X. Zhu, and R. M. White, IEEE Trans. Mag. **40**, 2323 (2004).
[15] S. Maat, M. J. Carey and J. R. Childress, Appl. Phys. Lett. **93**, 143505 (2008).
[16] K. Meguro, H. Hoshiya, and K. Nakamoto, J. Magn. Soc. Jpn. **32**, 234 (2008).
[17] K. Nagasaka, A. Jogo, H. Oshima, Y. Shimizu, S. Eguchi, and A. Tanaka, Intermag 2009, Digest EA-01, (2009).

Chapter 5
Analysis of spin asymmetries of CPP-GMR in $Co_2Fe(Al_{0.5}Si_{0.5})$/Ag/$Co_2Fe(Al_{0.5}Si_{0.5})$ trilayer

5.1 Introduction

The understanding of the spin-dependent scattering in CPP-GMR is very important to develop the materials for further improvements of the MR output. This has not been investigated sufficiently for the Heusler alloy based CPP-GMR showing much larger MR outputs than those with conventional magnetic alloys. In the previous chapter, relatively large CPP-GMR outputs have been shown using $Co_2Fe(Al_{0.5}Si_{0.5})$ (CFAS) Heusler alloy layers and a Ag spacer layer. Then, this chapter describes analyses of the spin-dependent scattering characteristics of the CPP-GMR. Fitting of ΔRA measured in the CFAS/Ag/CFAS pseudo spin-valves with various CFAS layer thicknesses by the Valet-Fert reveals the bulk and interfacial scatterings quantitatively. In addition, the band matching between CFAS and Ag, and the spin-flip scattering at the CFAS/Ag are discussed.

5.2 Experimental data: variation of ΔRA for the CFAS layer thickness

Figure 5-1 shows the data of ΔRA of the PSVs with the CFAS(t_F)/Ag(5 nm)/ CFAS(t_F) trilayer measured at 14 K and 290 K. All the devices were annealed at 500 °C for 30 min before the microfabrication. At 14 K, ΔRA increased with increasing the CFAS thickness up to ~8nm, indicating the contribution of the bulk scattering. However, in the thickness range $t_F > 8$ nm, ΔRA showed an almost constant value of ~17 mΩμm^2. At 290 K, ΔRA showed a nearly constant value in the examined CFAS thickness range except below 4 nm. The most likely physical description which explains these experimental results may be as follows. The bulk scattering contributes to the CPP-GMR only within a thin thickness due to the short spin diffusion length of the CFAS film. The spin diffusion length becomes shorter with increasing temperature, thus there was no increment of ΔRA from $t_F = 4$ nm to 8 nm at 290 K unlike those at 14 K.

Figure 5-2 shows the variation of the device resistance in the parallel magnetization state (RA_P) for t_F. The lead resistance estimated by the R–$1/A$ plot has been subtracted (see 4.6.5). The increment of RA_P should be accounted for the resistivity of the CFAS film ρ_F. The least square fitting yields ρ_F to be ~50 μΩcm. This value is somewhat smaller than that obtained by measuring in the 80 nm thick film of 71 μΩcm (see 4.3.3). The reason of the deviation is not clear. However, it is difficult to measure the resistivity from the plot of RA_P for t_F with a good accuracy due to the scattering of the data. Thus, we use the value of the resistivity of the 80 nm thick CFAS films deposited directly on the substrate for the analysis of the data.

It should be noted that there is a finite resistance of RA_P ~ 13 mΩμm^2 at the $t_F = 0$ in Fig. 5-2. This residual or parasitic resistance is too high to be accounted for the resistance of the other layers, *i.e.* the Ag spacer layer and the capping layer. We consider that the parasitic resistance is the contact resistance between the Ru capping and the Ta/Cu top lead electrode, because the Ru capping was exposed into air before depositing the top lead electrode. Indeed, the resistance of the active part of the CPP-GMR device, *i.e.* CFAS/Ag/CFAS trilayer, is thought to be much smaller than those shown in Fig. 5-2, which is estimated to be only several mΩμm^2 from the values of the resistivity of the CFAS film and the interfacial resistance at CFAS/Ag. Thus, the intrinsic MR ratio of the current CPP-GMR could be ~100%. On the other hand, the device resistance of tunnel magnetoresisnce (TMR) is predominantly governed by the tunnel resistance which is

intrinsic for the MR, thus the measured TMR ratio mostly indicates the intrinsic MR ratio. Thus, discussing the CPP-GMR output by the MR ratio of the device is less significant because it does not reflect the intrinsic resistance change ratio.

Figure 5-3 shows the variation of the MR ratio for t_F at 14 K and 290 K. In the CFAS thickness range where ΔRA increases with increasing the thickness, the MR ratio shows an almost constant value. On the other hand, in the thicker range, the MR ratio monotonically decreases because the value of ΔRA is saturated, whereas the device resistance increased along with the increasing CFAS thickness.

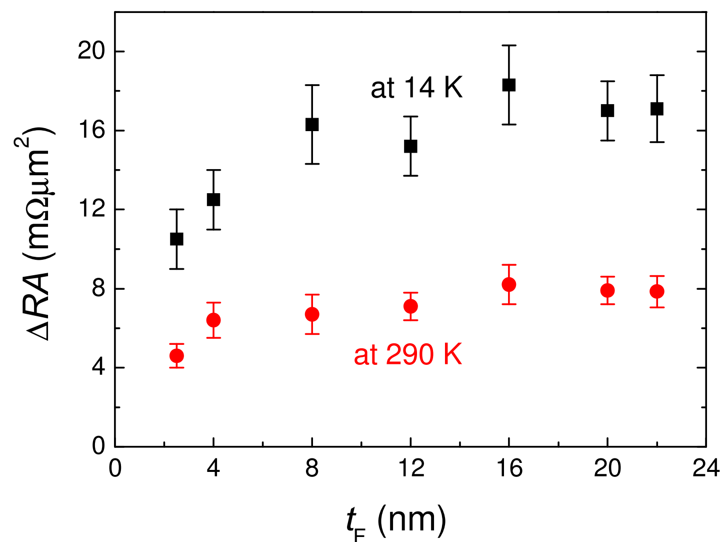

Fig. 5-1 Variation of ΔRA for the CFAS layer thickness t_F in CFAS(t_F)/Ag(5 nm)/ CFAS(t_F) pseudo spin-valve devices.

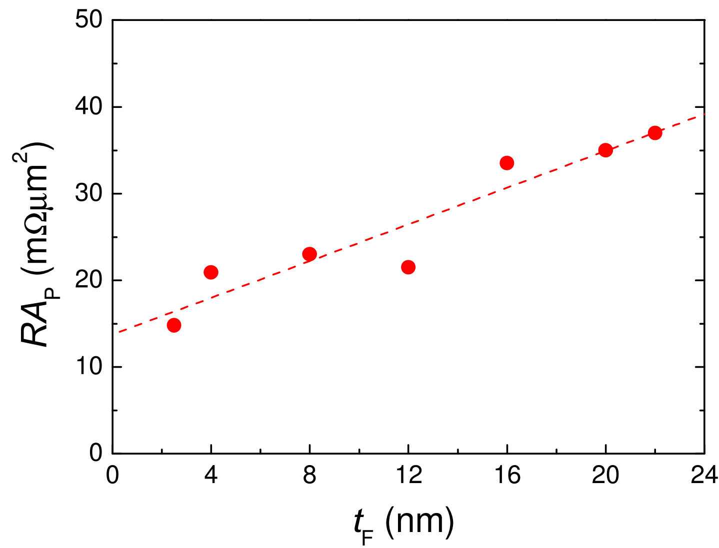

Fig. 5-2 Values of *RA* for the parallel magnetization (RA_P) state at 290 K as a function of the CFAS layer thickness t_F. The residual resistance in the limit of t_F = 0 may be the contact resistance between the top of the pillar and the lead electrode.

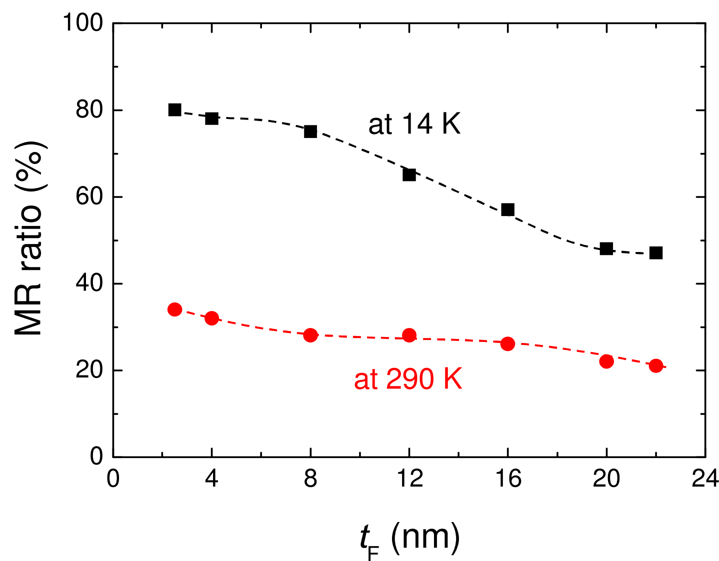

Fig. 5-3 MR ratio for various CFAS layer thickness t_F. The lead resistance was subtracted from RA_P. The lines are the guides for eyes.

5.3 Estimation of the CFAS/Ag interfacial resistance

The interfacial specific resistance $AR_{F/N}$ at the ferromagnetic (F)/nonmagnetic (N) junction is one of the physical factors which determine the value of CPP-GMR. Since the portion of ΔRA by the contribution of the interfacial scattering is given as a product of the term of the interfacial spin asymmetry and the interfacial resistance, $\gamma^2 AR^*_{F/N}$, where $AR^*_{F/N} = AR_{F/N} / (1-\gamma^2)$. The values of γ and $AR_{F/N}$ cannot be obtained independently by fitting ΔRA using the Valet-Fert model. $AR_{F/N}$ can be estimated from the increment of RA in F/N multilayers with different stacking periods. The specific resistances of various F/N interfaces have been measured for antiferromagnetically coupled systems as shown in Table 5-1 [1]. In the antiparallel magnetization configuration, the total resistance of the parallel resistance circuit is given by

$$RA^{AP} = M(\rho^*_F t_F + \rho_N t_N + 2AR^*_{F/N}), \qquad (5.1)$$

where M is the number of the multilayer period. The advantage of these systems is that the extended interfacial specific resistance $AR^*_{F/N}$ is directly obtained. However, the current CFAS/Ag/CFAS devices do not show an antiforromagnetic coupling with the 5 nm thick spacer layers. Although the thinner Ag spacer layers show an antiferromagnetic coupling as shown in 4.4, measuring $AR_{F/N}$ in devices with a different spacer thickness from those used for characterize CPP-GMR should be avoided, since the same film quality may not be guaranteed for the CFAS layers grown on the spacer layers with different thicknesses. Moreover, the lower resistance for heat treatments may give rise to a problem for multilayers with thin spacer layers. The current PSVs are annealed at 500 °C to obtain the large CPP-GMR value. Therefore, the direct estimation of $AR^*_{F/N}$ for the CFAS/Ag system is not realistic.

In this work, the interfacial specific resistance was estimated by measuring RA in the parallel magnetization state (RA_P) for three multilayers as follows.

Sample1: CFAS(10)/Ag(5)/CFAS(10) $M = 1$,

Sample2: $[CFAS(5)/Ag(5)]_{\times 3}$/CFAS(5) $M = 3$,

Sample3: $[CFAS(3.3)/Ag(5)]_{\times 5}$/CFAS(3.3) $M = 5$,

where M is the number of the Ag spacer layers. The total thickness of the CFAS layers was kept to 20 nm for all the samples. It should be mentioned that the mean free path is an important factor for the resistivity of very thin films. This is because the effective

resistivity of electron flowing perpendicular to the film plane should increase when the thickness of the individual film is comparable to the mean free path or thinner, since the scattering at the interfaces with the adjacent layers plays the dominant role in the scattering of electron. We have estimated the mean free path of the CFAS films with ρ = 71 μΩcm to be 0.6 nm at room temperature from the Hall effect measurement and by the Drude's free electron model (see 4.3.4), which is sufficiently smaller than the thinnest CFAS layer thickness of this work. Thus, the resistivity of the CFAS film is reasonably assumed to be independent of the layer thickness. On the other hand, the mean free path of the Ag film was estimated to be 36 nm, which is much larger than the spacer layer thickness of 5 nm. Thus, the transport in the Ag spacer layers is thought to be rather ballistic than diffusive, therefore the resistance in the bulk of the spacer layers may not be taken into account for the resistivity of the multilayer.

Figure 5-4 shows the values of RA_{P} of the CFAS/Ag multilayes for M = 1, 2, and 3. Since the total thicknesses of the CFAS layers are the same for all the multilayers and the resistance in the Ag spacer layers is negligible as mentioned above, the increment of the RA_{P} is accounted for the interfacial resistance ($AR_{\mathrm{F/N}}$) and the boundary resistance caused by the spin accumulation ($RA_{\mathrm{SI}}^{\mathrm{P}}$) given by Eq. (2.21). The value of $RA_{\mathrm{SI}}^{\mathrm{P}}$ is expected to be negligibly small as plotted in Figs. 2-5 and 2-6. Thus, the increment of the RA_{P} for M should correspond to the double of the interfacial specific resistance, thus $AR_{\mathrm{F/N}} = 0.25^{+0.30}_{-0.25}$ mΩμm^2 is obtained. These measurements were done for various temperatures, however, no noticeable temperature dependence of $AR_{\mathrm{F/N}}$ was found. Therefore, we regard the value of $AR_{\mathrm{F/N}}$ to be temperature independent. The value of the interfacial specific resistance at CFAS/Ag was comparable to those of the conventional materials as listed in Table 5-1.

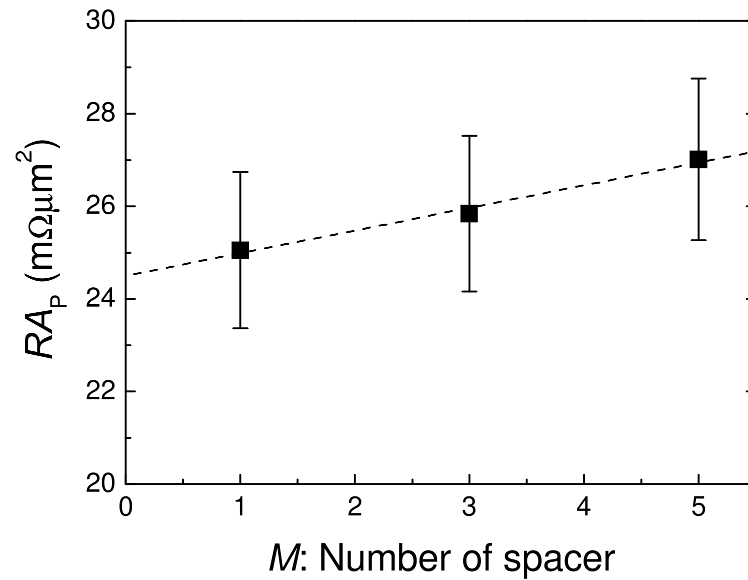

Fig. 5-4 Resistance-area product of the parallel magnetization state (RA_P) of the CFAS/Ag multilayers with M spacer layers measured at room temperature. The total thickness of the CFAS layers were fixed to 20 nm.

F/N	$AR_{F/N}$ (mΩμm^2)	γ
Co/Cu	0.23	0.77
Co/Ag	0.18	0.8
Py/Cu	0.17	0.7
Fe/Cr	0.4	–0.7

Table 5-1 Specific resistance and spin asymmetry of conventional F/N interfaces reported by Bass and Pratt, Jr. [1].

5.4 Analysis of the spin-dependent scattering

5.4.1 Valet-Fert model

Now we know all the physical values to interpret the data of ΔRA–t_F using the Valt-Fert model, *i.e.* the resistivities of the ferromagnetic and nonmagnetic layers ρ_F and ρ_N, and the interfacial specific resistance $AR_{F/N}$. The spin diffusion length of Ag has been reported to be up to several hundred nm, which is sufficiently long to approximate to be $t_N \ll \ell_{sf}$ in Eqs. (2.22) and (2.23). Thus, ΔRA is given as a function of t_F by

$$\Delta RA = 4\left[\frac{\frac{\gamma^2}{\rho_F^*\ell_{sf}}\coth\left(\frac{t_F}{2\ell_{sf}}\right)+\frac{\beta^2}{AR_{F/N}^*}}{\frac{1}{AR_{F/N}^*}\frac{1}{\rho_F^*\ell_{sf}}\coth\left(\frac{t_F}{2\ell_{sf}}\right)} - \frac{\frac{2(\beta-\gamma)^2}{\rho_N t_N}+\frac{\gamma^2}{\rho_F^*\ell_{sf}}\coth\left(\frac{t_F}{2\ell_{sf}}\right)+\frac{\beta^2}{AR_{F/N}^*}}{\frac{2}{\rho_N t_N}\frac{1}{\rho_F^*\ell_{sf}}\coth\left(\frac{t_F}{2\ell_{sf}}\right)+\frac{1}{AR_{F/N}^*}\left[\frac{2}{\rho_N t_N}+\frac{1}{\rho_F^*\ell_{sf}}\coth\left(\frac{t_F}{2\ell_{sf}}\right)\right]}\right]$$

(5.2),

where β: bulk scattering spin asymmetry,
ℓ_{sf}: spin diffusion length of the ferromagnetic layer,
γ: interfacial scattering spin asymmetry
are the free parameters for the fitting.

Figure 5-5 shows the fitted curves for ΔRA–t_F of the CFAS(t_F)/Ag(5 nm)/CFAS(t_F) PSVs annealed at 500 °C for 30 min measured at 14 K and 290 K, which yielded β = 0.77±0.05, ℓ_{sf} = 3.0±0.8 nm and γ = 0.93±0.07 at 14 K and β = 0.70±0.08, ℓ_{sf} = 2.2±1.0 nm and $\gamma = 0.77^{+0.23}_{-0.14}$ at 290 K. The values of error are by the errors of the measured values of ΔRA and the uncertainty of the fitting. The relatively high bulk scattering spin asymmetry β and the high resistivity of the CFAS film provides a larger bulk scattering per unit layer thickness ($\beta^2\rho_F^*$). However, the short spin diffusion length of the CFAS layer effectively limits the contribution of the bulk scattering within the thin thickness range from the interface with the spacer layer. Therefore, the enhancement of ΔRA with increasing t_F was saturated at ~8 nm at 14 K and ~4 nm at 290 K. The spin diffusion length of the CFAS film is much shorter than those of other ferromagnetic alloys (*e.g.* 5.5 nm of NiFe at 4.2 K [4], 12 nm of CoFe at 4.2 K[5], ~3 nm of CoFeAl at RT [6], and ~5 nm of CoFeGe at RT [7]). This is reasonable for the relatively high resistivity of the CFAS films of 62.4 μΩcm at 14 K and 71.0 μΩcm at 290 K, considering the empirical relationship that the spin diffusion length is proportional to the inverse

resistivity (namely, the conductivity) for both nonmagnetic and ferromagnetic materials as pointed out by Bass and Pratt, Jr. [1]. Figure 5-6 plots the spin diffusion length of various 3*d* ferromagnetic elements and alloys as a function of the inverse resistivity [1], the spin diffusion length of the CFAS film shows a good agreement with the empirical relationship of ℓ_{sf}–$1/\rho_F$. Reflecting the imperfect B2 ordering the CFAS films of S_{B2} ~ 0.7 (see 4.3.1), the value of β was much smaller than the half-metallic value. Obtaining higher degree of order will realize a higher β and a longer spin diffusion length, which will improve the maximum ΔRA.

The interfacial scattering spin asymmetry of the CFAS/Ag system was found to be remarkably high, reflecting the large value of ΔRA extrapolated into $t_F = 0$ (the intercept of ΔRA–t_F). In addition, the temperature dependence of the interfacial scattering spin asymmetry was found, which is uncommon among conventional materials [3]. If one fits ΔRA–t_F of the current CFAS/Ag/CFAS PSVs under a restriction that the interfacial scattering is temperature independent, a physically invalid result that the spin diffusion length of the CFAS layer increases with increasing temperature is obtained. Therefore, we consider that the large temperature dependence of the interfacial scattering is a correct interpretation of the experimental results. The values of the interfacial specific resistance of the up and down spin channels can be obtained by the relationships of

$$\frac{1}{AR_{\mathrm{F/N}}} = \frac{1}{AR_{\mathrm{F/N}}^{\uparrow}} + \frac{1}{AR_{\mathrm{F/N}}^{\downarrow}} \tag{5.3}$$

$$\gamma = \frac{AR_{\mathrm{F/N}}^{\downarrow} - AR_{\mathrm{F/N}}^{\uparrow}}{AR_{\mathrm{F/N}}^{\uparrow} + AR_{\mathrm{F/N}}^{\downarrow}} \tag{5.4}$$

to be $AR_{F/N}^{\uparrow}$ = 0.28 m$\Omega\mu$m^2 and $AR_{F/N}^{\downarrow}$ = 7.2 m$\Omega\mu$m^2 at 14 K, and $AR_{F/N}^{\uparrow}$ = 0.26 m$\Omega\mu$m^2 and $AR_{F/N}^{\downarrow}$ = 2.2 m$\Omega\mu$m^2 at 290 K. $AR_{F/N}^{\uparrow}$ was almost constant because the total interfacial resistance ($AR_{F/N}$) was independent of temperature which is dominated by the channel with the lower resistance. On the other hand, $AR_{F/N}^{\downarrow}$ was strongly dependent on temperature, reflecting the large temperature dependence of the interfacial scattering spin asymmetry. The origins of the large interfacial scattering and the temperature dependence are discussed below.

The short spin diffusion length can be a big obstacle to obtain large CPP-GMR outputs ΔRA, when there is no limitation in the magnetic layer thickness in the device. For the read head application, however, the thickness of the devices has to fit the read gap (shield-to-shield spacing), thus the thickness of the magnetic layer is limited less

than a few to several nm. In addition, for high reading resolution the magnetic flux from the individual recording bit has to match that the free layer of the read head absorbs. Thus, the thickness of the individual magnetic layer has to be a few nm. Under such a limitation of the thickness, the short spin diffusion length of ~ 2.2 nm is rather desirable because the maximum MR output can be obtained with very thin magnetic layers [6].

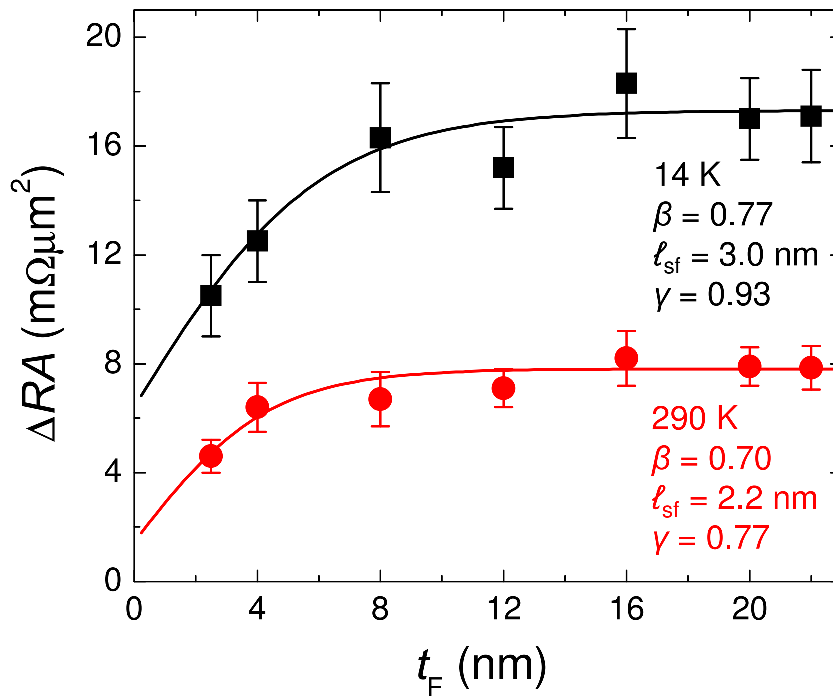

Fig. 5-5 Variation of Δ*RA* of the pseudo spin-valves of CFAS(t_F)/Ag(5 nm)/CFAS(t_F) at 14 K (square) and 290 K (circle) and the fittings curves by the Valet-Fert model (Eq. (5.1)).

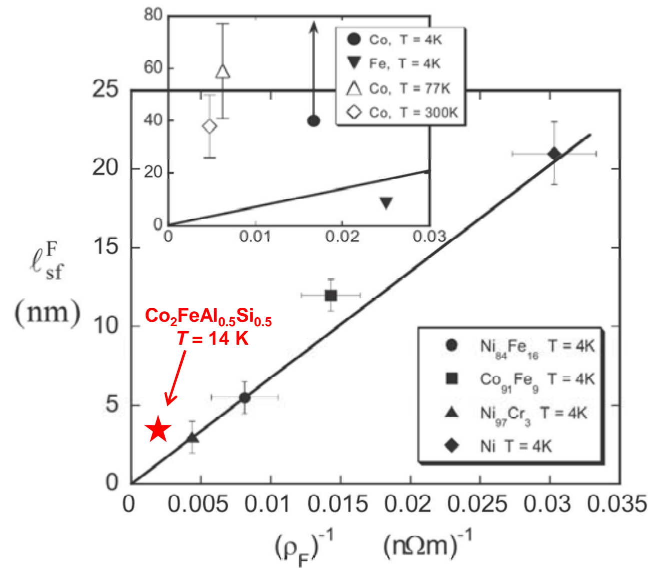

Fig. 5-6 Empirical relationship between the spin diffusion length and the inverse resistivity for 3*d* metals and alloys by Bass and Pratt, Jr. [1]. The data for the $Co_2Fe(Al_{0.5}Si_{0.5})$ shows a good agreement with the linear line of $\ell_{sf} = 1/\rho_F$.

5.4.2 Newly developed Taniguchi-Imamura model

The Valet-Fert equation is obtained by solving the diffusion equation under the periodic boundary condition of F/N multilayer, where F and N represent the ferromagnetic and nonmagnetic layers, respectively. However, the actual CPP-GMR devices are not always such periodic F/N multilayers. Especially, the spin-valves are composed of an F/N/F trilayer connected with lead electrodes, which does not satisfy the periodic boundary condition for obtaining the Valet-Fert equation. Very recently, Taniguchi and Imamura developed a new theoretical model for N-lead/F/N-spacer/F/N-lead five-layer system which is the same as pseudo spin-valves [8]. The nonmagnetic lead electrodes (N-lead) are treated to be semi-infinite in this model. The Valet-Fert equation applied to a pseudo spin-valve has a coefficient of 4 in Eq. (5.2), which originates from the four interfaces of F/N (two for N-lead/F and two for F/N-spacer) contributing to the CPP-GMR. Thus, the Valet-Fert model treats the contributions of the spin accumulations at the four F/N interfaces to be equal. However, Taniguchi and Imamura revealed that the spin accumulations at the two interfaces between F and N-spacer are much larger than those at the N-lead/F interfaces. Therefore, the Valet-Fert model leads to underestimations of the contribution of the spin accumulations at the F/N-spacer

interfaces to ΔRA, so that the values of β and γ are underestimated. Figure 5-7 shows the fitting by the Taniguchi-Imamura equation, yielding $\beta = 0.86^{+0.02}_{-0.06}$, $\ell_{sf} = 4.2^{+2.3}_{-0.2}$ and $\gamma = 0.93^{+0.02}_{-0.03}$ at 14 K and $\beta = 0.75^{+0.03}_{-0.05}$, $\ell_{sf} = 3.5^{+1.0}_{-0.5}$ and $\gamma = 0.89^{+0.02}_{-0.03}$ at 290 K. The Taniguchi-Imamura model gives higher β and γ, and a longer spin diffusion length. The difference of the scattering spin asymmetries between 14 K and 290 become larger for β and smaller for γ compared to the Valet-Fert model.

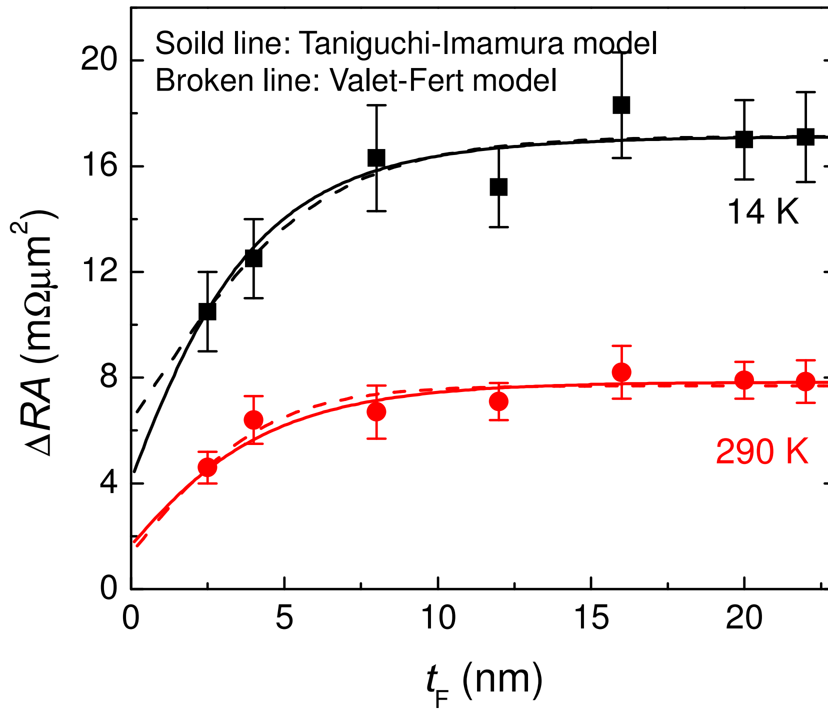

Fig.5-7 (solid line) Fitting of ΔRA–t_F by the new theoretical model developed by Taniguchi and Imamura [8]. (broken line) Fitting by the Valet-Fert model.

5.5 Effect of the insertion of CFAS(1 nm) layers at CoFe/Ag interfaces

As described in 5.4, a large contribution of the interfacial scattering at CFAS/Ag has been suggested. However, data is lacking for the very thin t_F range (< 2 nm) due to the difficulty in obtaining the antiparallel magnetization state in PSVs with such thin magnetic layers. In this subsection, an effect of insertions of very thin CFAS(1 nm) layers at $Co_{50}Fe_{50}$/Ag interfaces is shown to demonstrate the large spin-dependent scattering at CFAS/Ag interface. The samples are

Sample 1: CoFe(2 nm)/Ag(5 nm)/CoFe(2 nm)

Sample 2: CoFe(2 nm)/CFAS(1 nm)/Ag(5 nm)/CFAS(1 nm)/CoFe(2 nm)

on the Cr(10 nm)/Ag(100 nm) underlayer and capped with Ag(5 nm)/Ru(8 nm). The surfaces of the films were observed by RHEED after the deposition of each layer. As shown in Fig. 5-8, the RHEED patterns of the CFAS(1 nm) layers were streaky, thus the layers are considered to be grown two-dimensionally rather than island-like. The samples were annealed at 500 °C for 30 min and microfabricated into CPP-GMR devices.

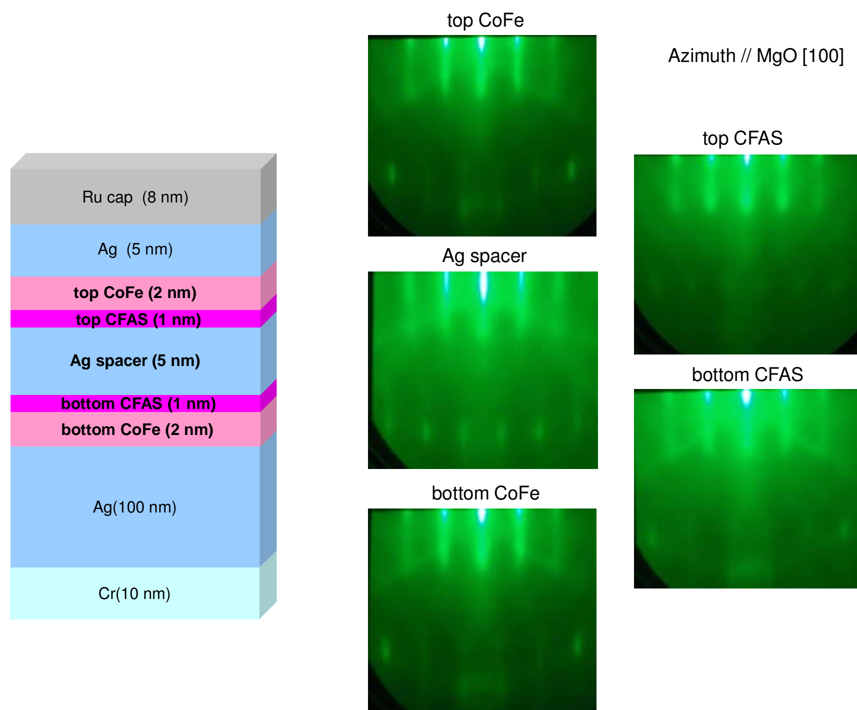

Fig. 5-8 RHEED patterns of CoFe(2)/CFAS(1)/Ag(5)/CFAS(1)/CoFe(2) (thickness in nm) PSV taken after the deposition of each layer.

Figure 5-9 shows the CPP-GMR curves of the devices (a) without and (b) with the CFAS (1 nm) insertions at the CoFe/Ag interfaces measured at room temperature. The CoFe/Ag/CoFe trilayer showed ΔRA of 2.1 m$\Omega\mu$m^2. The insertion of the thin CFAS layer effectively enhanced ΔRA to 3.8 m$\Omega\mu$m^2. This value of ΔRA is thought to be due to the bulk scattering in the CoFe layers, the bulk scattering in the CFAS layers and the scattering at the CFAS/Ag interfaces. The contribution of the bulk scattering of CoFe is considered to be up to 1 m$\Omega\mu$m^2 from the reported β [5], [8] and the resistivity of the CoFe film (6.3 $\mu\Omega$cm at RT). Thus, the value of ΔRA derived from both the bulk scattering in the CFAS layers and the scattering at the CFAS/Ag interfaces is thought to be 2–3 m$\Omega\mu$m^2. This value lies on the fitting curves by both the Valet-Fert model and the Taniguchi's model shown in Fig. 5-7. Figure 5-10 shows the temperature dependences of ΔRA of samples 1 and 2. Sample 2 (with CFAS insertion) showed a larger temperature dependence than that of sample 1 due to the larger temperature dependence of ΔRA in CFAS/Ag/CFAS than in CoFe/Ag/CoFe. As shown in Fig. 4-23, ΔRA in CFAS/Ag/CFAS shows the temperature dependence of ΔRA(14 K)/ΔRA(290 K) = 0.45 independent of the degree of B2 order of the CFAS layer. Therefore, the value of ΔRA derived from the 1 nm CFAS layers at 14 K is estimated to be (2–3/0.45) ~ 5.5 m$\Omega\mu$m^2. This value does not lie on the fitting curves very well (Fig. 5-7), which can be due to that the degree of order in the 1 nm CFAS may be lower than those in the thicker films.

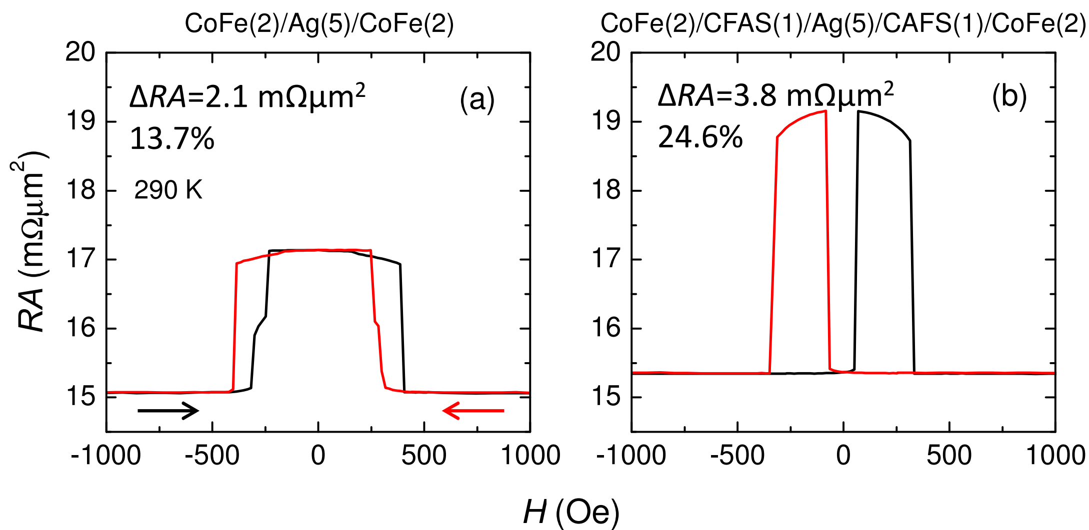

Fig. 5-9 MR curves at room temperature of (a) CoFe/Ag/CoFe and (b) CoFe/CFAS/Ag/CFAS/CoFe PSVs.

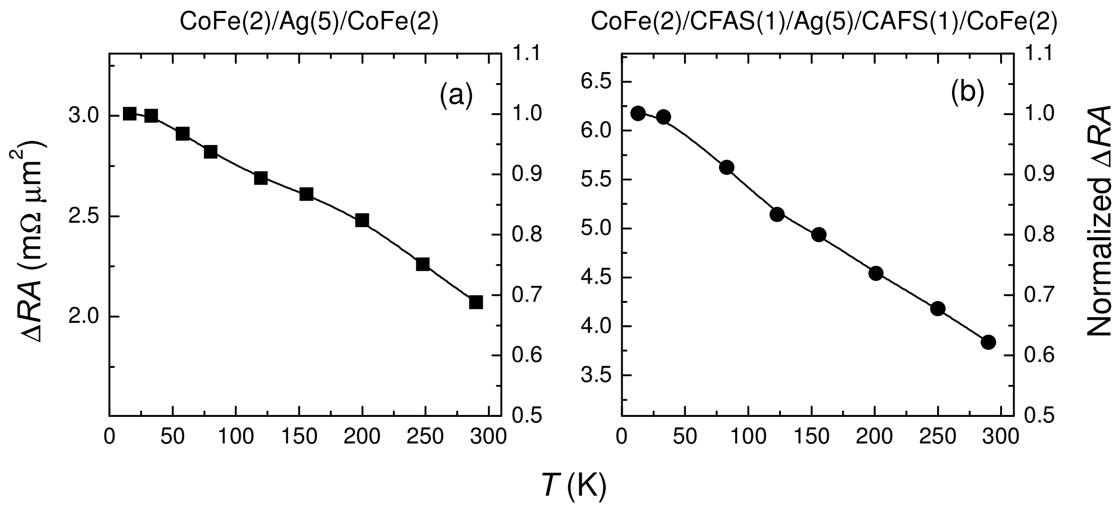

Fig. 5-10 Measurement temperature dependences of Δ*RA* of (a) CoFe/Ag/CoFe and (b) CoFe/CFAS/Ag/CFAS/CoFe PSVs.

5.6 Relationship between the spin asymmetries and the degree of B2 order

The CFAS/Ag/CFAS PSVs showed relatively large Δ*RA* even with the thin magnetic layer thicknesses down to 2.5 nm, where the films were annealed at 500 °C for 30 min to improve the B2 ordering. In 4.6.6, a strong dependence of Δ*RA* on the annealing temperature (T_{an} = 250–550 °C) has been shown for the PSVs with the CFAS layer thickness of 2.5 nm. This means that the degree of B2 order strongly affects on the spin-dependent scattering of the CPP-GMR. However, the spin asymmetries and the spin diffusion length have not been discussed since the PSVs with only one CFAS layer thickness was compared for the different annealing temperatures. In this chapter, the values of Δ*RA* of the CFAS/Ag/CFAS PSVs annealed at 400 °C for 30 min with different CFAS layer thicknesses are shown and the spin asymmetries and the spin diffusion length are discussed.

PSVs with CFAS(t_F)/Ag(5 nm)/CFAS(t_F) (t_F = 2.5, 4.0, and 8.0 nm) annealed at T_{an} = 400 °C for 30 min were fabricated. The layered structures and the fabrication

procedures are the same as described above. The resistivities, the degrees of B2 order, and the saturation magnetizations of the CFAS films annealed at 400 and 500 °C are summarized in Table 5-1. The resistivity was measured in 80 nm CFAS films directly deposited on the MgO(001) substrates and the degree of order and the magnetization were measured in 10 nm thick CFAS films deposited on MgO(001) substrate/Cr(10 nm)/Ag(100 nm) underlayers as described in 4.3.

T_{an} (℃)	ρ_F (μΩcm) at 15 K	ρ_F (μΩcm) at 290 K	S_{B2}	M_s (emu/cc) at 290 K
400	71.0	82.0	0.53	1025
500	62.4	71.0	0.67	1100

Table 1-2 Resistivity, degree of B2 order, and saturation magnetization of the CFAS films annealed at 400 °C and 500 ℃.

Figure 5-11 shows the values of ΔRA of the PSVs annealed at 400 °C (open symbols) measured at 15 K and 290 K. Although the accuracy of the fitting from only the three data may not be sufficient, we can discuss the spin asymmetries and the spin diffusion length by comparing with those of the PSVs annealed at 500 °C (solid symbols). First, the increment of ΔRA from t_F = 2.5 nm to 4.0 nm, *i.e.* the contribution of the bulk scattering to ΔRA, in the PSVs annealed at T_{an} = 400 °C is comparable to that of the PSVs annealed at T_{an} = 500 °C. Thus, the bulk scattering spin asymmetry of the devices of T_{an} = 400 °C is expected to be only somehow smaller than that of T_{an} = 500 °C due to the higher resistivity of the CFAS film of T_{an} = 400 °C than that of T_{an} = 500 °C. Second, there is no increment of ΔRA between t_F = 4.0 nm and 8.0 nm for T_{an} = 400 °C even at 15 K unlike that for T_{an} = 500 °C. This indicates that the spin diffusion length of the CFAS films annealed at 400 °C is shorter than those annealed at 500 °C, which can be understand due to the higher resistivity and the empirical relationship that the spin diffusion length is proportional to the conductivity shown by Bass and Pratt, Jr. [1]. Third, the values of the intercept of ΔRA–t_F of the PSVs annealed at T_{an} = 400 °C and 500 °C measured at 15 K and 290 K seem different, indicating that the contribution of the interfacial scattering depends both on the degree of B2 order and on temperature. The fitting by the Valet-Fert model yielded β ~ 0.75, ℓ_{sf} ~ 2.0 nm, and γ ~ 0.73 for the

PSVs of T_{an} = 400 °C measured at 15 K and β ~ 0.68, ℓ_{sf} ~ 1.7 nm, and γ ~ 0.50 for those measured at 290 K. The difference in the bulk scattering spin asymmetry β between T_{an} = 400 °C and 500 °C was not significantly large. On the other hand, the interfacial scattering spin asymmetry seems to be strongly dependent on both the degree of B2 order and the measurement temperature, although the determination of the value of the intercept of ΔRA–t_F may include an uncertainty due to the limited number of the data points and the short spin diffusion length of the CFAS films. Thus, the observed large dependence of ΔRA both on the annealing temperature and on the measurement temperature may be derived rather from the change of the contribution of the interfacial scattering to ΔRA than from that of the bulk scattering.

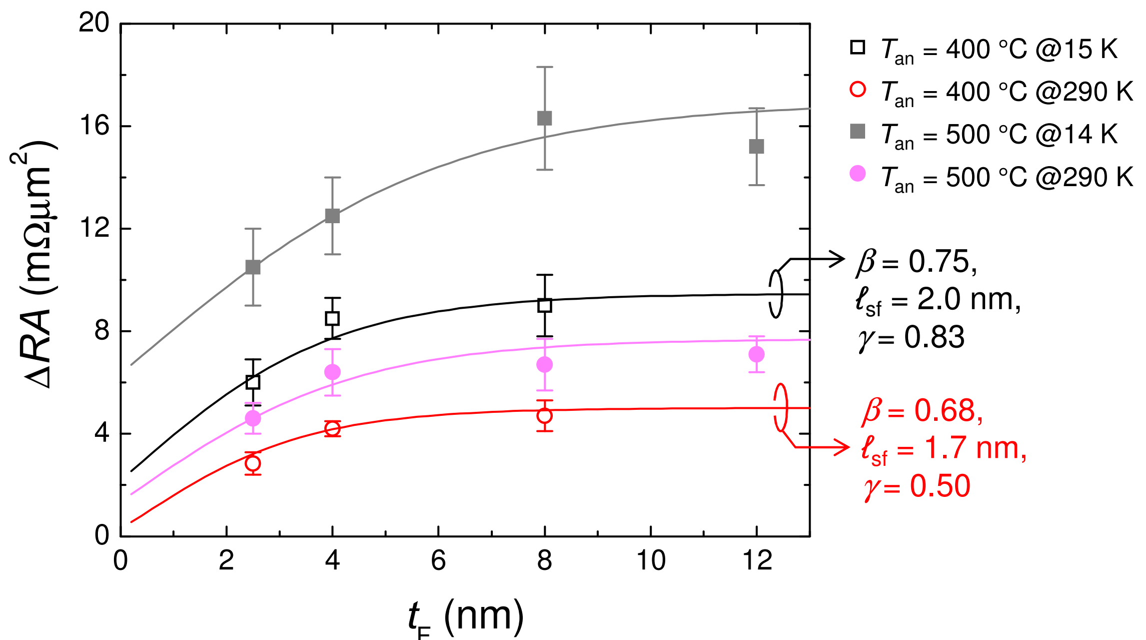

Fig.5-11 ΔRA as a function of the CFAS layer thickness (t_F) of the CFAS/Ag/CFAS PSVs annealed at 400 ℃ measured at 15 K (open square) and at 290 K (open circle) and the fitting curves by the Valet-Fert model. The data and fittings of the PSVs annealed at 500 ℃ measured at 14 K (filled square) and at 290 K (filled square) are shown together.

5.7 Discussion

5.7.1 Origins of the large interfacial scattering at CFAS/Ag and its temperature dependence

The band matching between the ferromagnetic and nonmagnetic materials should intrinsically influence the interfacial spin-dependent scattering. Band matching means the similarity of the band structures at an interface between two different materials. When the band matching of the up spin band is better than that of the down spin band, the up spin electron has the higher transmission probability (or, less scattered) than that of the down spin electron. Thus, interfacial resistance of the up spin electron ($R_{F/N}^{\uparrow}$) is smaller than that of the down spin electron ($R_{F/N}^{\downarrow}$), which gives rises to a nonzero interfacial scattering spin asymmetry (γ). The interface between fcc-Co and fcc-Cu is believed to be good band matched for the up spin electrons due to the similarity of the band dispersions of Co and Cu for the up spin electron. One the other hand, the band structure of the down spin electron is dissimilar at the Co/Cu due to the exchange splitting. Thus, the band matching at the Co/Cu interface is good for the up spin electron but poor for the down spin electron [10][11].

The CPP-GMR devices with the CFAS/Ag/CFAS showed a relatively small interfacial specific resistance $AR_{F/N}$ and a large interfacial scattering spin asymmetry γ, which results in a large contribution of the interfacial scattering to ΔRA. These experimental results clearly indicate a good band matching between CFAS and Ag. This is consistent with the theoretical calculation of the transport at the Co_2MnSi/Ag(001) interface [12].

The origin of the large temperature dependence of the interfacial resistance is a question. Although there is no experimental result to support, we think the reduction of the contribution of the interfacial scattering is related to the reduction of the bulk spin polarization. Schep *et al.* derived a form of the interfacial resistance between materials A and B from the Boltzmann equation to be

$$AR = \frac{h}{e^2}\left[\frac{1}{T_{\mathrm{tot}}} - \frac{1}{2}\left(\frac{1}{S_{\mathrm{A}}} + \frac{1}{S_{\mathrm{B}}}\right)\right], \qquad (5.5)$$

where h is the Plank constant, e is the elementary charge, S_i (i = A, B) is the area of the Fermi surface projected in the direction of the interface, and T_{tot} is the transmission probability integrated over the Fermi surface (FS) given by

$$T_{\mathrm{tot}} = \frac{1}{(2\pi)^2} \int_{\mathrm{FS_A}} d^2 K T_{\mathrm{A} \leftarrow \mathrm{B}}(\mathbf{k}) \,. \qquad (5.6)$$

This means that the interfacial resistance is given by the inverse of the transmission probability from one material to the other material integrated over the Fermi surface [13][14]. We consider that in Heusler alloy with high spin polarization the shape of the Fermi surface can change dependent on temperature due to the thermally excited electronic state in the (pseudo) band gap at the Fermi level. Thus, total transmission probability T_{tot} may depends on temperature for the down spin channel, which gives rise to the temperature dependence of the interfacial resistance of the down spin electron. In practical point of view, the suppression of the large temperature dependence of the interfacial scattering is required to obtain large CPP-GMR outputs at room temperature. For that, some refinement of the electronic structure at the F/N interface may be effective as recently attempted by inserting thin CoFe layers at Heusler alloy/spacer layer interfaces [15].

5.7.2 Spin-flipping at the CFAS/Ag interface

The Valet-Fert model does not consider the effect of the spin-flip scattering at the F/N interface. However, the loss of spin memory by the spin flip scattering at the interface with spacer layer is thought to occur. In this section, experiments which were made to investigate the spin flip at the CFAS/Ag interface are discussed.

Experiments

Three PSVs were fabricated. The one was a normal PSV with two CFAS magnetic layers separated by a Ag spacer layer. The other ones had very thin insertions of Ag within the CFAS layers. The layered structures were

Sample 1: CFAS(4)/Ag(5)/CFAS(4)

Sample 2: CFAS(4)/Ag(5)/CFAS(2)/Ag(1)/CFAS(2)

Sample 3: CFAS(2)/Ag(1)/CFAS(2)/Ag(5)/CFAS(2)/Ag(1)/CFAS(2)

on the Cr(10)/Ag(100) underlayer and with the Ag(5)/Ru(8) capping layer (thickness in nm). The thickness of the Ag insertion layer was chosen to couple the CFAS layers ferromagnetically as discussed in 4.4. Then, the magnetization directions of the CFAS(2 nm) layers separated by the Ag(1 nm) insertion layer are always parallel.

The growth of the CFAS/Ag insertion layer/CFAS layered structure was observed by RHEED. Although the diffraction from the Ag(1 nm) layer was broaden compared to that from the CFAS(2 nm) layers (suggesting poorer crystallinity of the thin Ag), the diffraction pattern was still streaky, thus the growth of the Ag layer is thought to be two-demensional.

Results and discussion

Figure 5-12 show the variation of ΔRA at room temperature as a function of the number of the Ag insertion. The MR curves were square shaped for the samples, showing only the parallel and antiparallel magnetization configurations between the magnetic layers separated by the Ag(5 nm) spacer layer. Thus the CFAS(2 nm) layers separated by the Ag(1 nm) insertion layer were ferromagnetically coupled. ΔRA decreased with increasing number of Ag insertion. In the case that there is no loss of the spin memory at the interface between the ferromagnetic and the nonmagnetic layers, *i.e.* in the absence of the spin flip at the interface, ΔRA should not decrease, but it rather increases because of the spin-dependent scattering between the CFAS layers and the Ag insertion layer. Such an enhancement of ΔRA has been reported for Cu insertions in Co,

CoFe or CoFeB magnetic layers [16]–[23]. For example, Ohshima *et al*. reported that ΔRA increased by 20% by inserting Cu(1.5 nm) layers in the CoFeB free layers [16],[17]. In the CFAS/Ag/CFAS PSVs, the analysis by the Valet-Fert model has revealed the significantly large contribution of the interfacial scattering at the CFAS/Ag interface, however, the Ag(1 nm) insertion decreased ΔRA. This is considered to be due to the presence of a considerable spin flip at the interface between the CFAS layer and the inserted Ag layer. In principle, the linear decrease with increasing number of Ag insertion shown in Fig. 5-12 should enable us to estimate the rate of spin flip scattering at the interface. Indeed, Dassonneville *et al.* have estimated the spin flip parameter δ of Co/Cu interface at 4.2 K to be 0.33 by measuring ΔRA of dual spin-valves with the free layers composed of $[Co(3 nm)/Cu(1.5 nm)]_n/Co(3 nm)$ multilayers (n = 0–8) [24]. The spin flip parameter gives the spin flip probability P by the relationship of $P = 1-\exp(-\delta)$ [24]. The long spin diffusion length of Co of ℓ_{sf} ~ 60 nm at 4.2 K [25] enabled them to assume that all the Co layers of the multilayer (total thickness of Co maximum 27 nm for n = 8) contributed to the bulk scattering. On the other hand, the spin diffusion length of the CFAS film has been estimated to be 2–4 nm as described in 5.4. Thus, the layer thickness of the CFAS film in the device examined here is comparable to the spin diffusion length. This makes the analysis of the spin flip rate at the CFAS/Ag interface complicated.

The other complex is the different behavior of the temperature dependence of ΔRA between the samples without (Sample 1) and with (Sample 2, 3) the Ag insertions as shown in Fig. 5-13. At room temperature (290 K), ΔRA decreased nearly linearly with increasing number of Ag insertion as shown in Fig. 5-12. However, at temperatures below room temperature, the difference of ΔRA between Samples 1 and 2 becomes much larger than that between Samples 2 and 3. This means that the insertion of Ag in one CFAS layer significantly decreases ΔRA, whereas the further decrease of ΔRA by inserting Ag into the other CFAS layer is much smaller. If the spin flip at the CFAS/inserted Ag interface contributes to the decrease of ΔRA wherever the insertion is (whether in the top CFAS layer or in the bottom CFAS layer), the observed behavior of decrease of ΔRA among Sample 1–3 is difficult to understand. Moreover, very interestingly, ΔRA of Sample 2 and 3 rapidly increased at around 50 K. Due to this, ΔRA of Sample 2 and 3 at below 30 K were almost the same as that of Sample 1. The reason of this unique behavior of the temperature dependence of ΔRA in the samples with the Ag insertion(s) is unclear at present. We would like to mention spin flip by phonon

scattering with spin–orbit interaction. According to the Elliott-Yafet mechanism [26][27][28], the spin relaxes by momentum scattering in a presence of the spin–orbit interaction. Since the continuity of the material is destroyed at the interface, the spin efficient spin–orbit coupling at the interface between a 3*d* magnetic layer and a nonmagnetic layer becomes effective to electrons propagating the multilayer. Then, the the electron scattering by the phonon is generally frozen at low temperature (typically below 30–50 K [29]). Thus, we think that the rapid increase of ΔRA in Samples 2 and 3 with the Ag insertion(s) may be due to the freezing of the phonon scattering, which may suppresses the spin flip by the Elliott-Yafet mechanism.

Although the quantitative interpretation on the spin flip rate at the CFAS/Ag interface is difficult at present due to the complexes as mentioned above, these experimental results indicate the presence of the loss of the spin memory by the spin flip scattering at the CFAS/Ag interface. It should be noted that the separation of the contributions of the two scatterings; *i.e.* the bulk and the interfacial scatterings is valid only when there is no spin mixing at the F/N interface. In the presence of the spin mixing at the interface, the effective spin asymmetry of the interfacial scattering which contributes to the CPP-GMR is thought to decrease. Furthermore, the contribution of the bulk scattering to the CPP-GMR may decrease since the spin flip at the interface should decrease the efficiency of the spin injection into the nonmagnetic spacer layer. We think the interfacial spin flip can be the origin of the large temperature dependence of ΔRA in the Heusler alloy based CPP-GMR devices. Thus, some refinement of the interface is expected to be effective to suppress the temperature dependence of ΔRA.

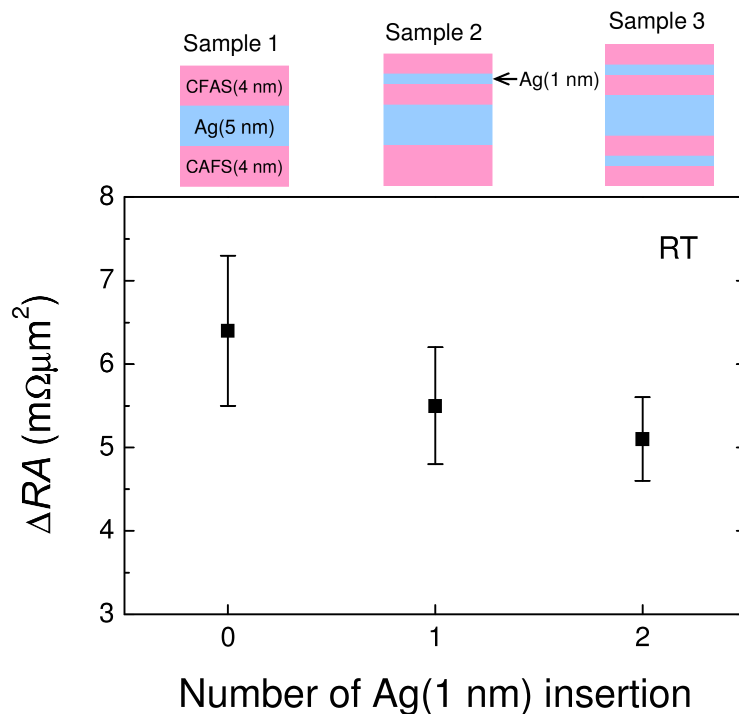

Fig. 5-12 ΔRA measured at room temperature of CFAS(4)/Ag(5)/CFAS(4) PSV and those with Ag(1 nm) insertion(s) within the CFAS layer(s).

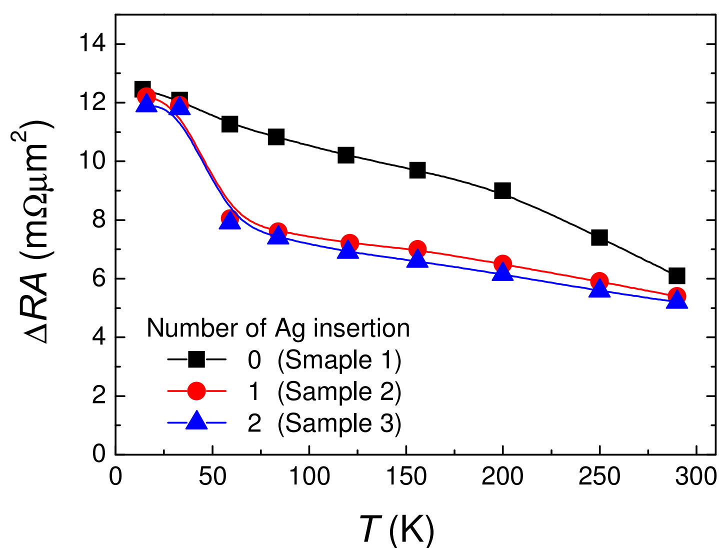

Fig. 5-13 Temperature dependence of ΔRA of Samples 1–3.

5.8 Summary of this chapter

The spin-dependent scattering characteristics were investigated for the trilayer composed of two $Co_2Fe(Al_{0.5}Si_{0.5})$ (CFAS) magnetic layers separated by the Ag spacer layer. The results are summarized as follows:

1) The interfacial specific resistant at CFAS/Ag(001) epitaxial interface was estimated experimentally to be $AR_{F/N}$ ~ 0.25 m$\Omega\mu$m^2 by measuring RA in the parallel magnetization states of CFAS/Ag multilayers. The value of $AR_{F/N}$ for the CFAS/Ag interface was comparable to those of the conventional materials such as Co/Cu.

2) The bulk (β) and interfacial (γ) spin asymmetries and the spin diffusion length of the CFAS layer (ℓ_{sf}) was evaluated by the Valet-Fert model for the pseudo spin-valves (PSVs) annealed at 500 °C. The fitting yielded β = 0.77, γ = 0.93, and ℓ_{sf} = 3.0 nm at 14 K and β = 0.70, γ = 0.77, and ℓ_{sf} = 2.2 nm at 290 K. This indicates that the bulk scattering contributes only within a few or several nm thick CFAS layers from the interfaces with the Ag spacer due to the short spin diffusion length of the CFAS film. On the other hand, the contribution of the scattering at the CFAS/Ag was revealed to be large, which provided the relatively large ΔRA even for t_F = 2.5 nm. Due to the large interfacial scattering at CFAS/Ag interface, the matching of the band structure of the up spin electron at the CFAS/Ag interface is considered to be good.

3) A significant temperature dependence of the contribution of the interfacial scattering was suggested, which has not been known for CPP-GMR systems with conventional magnetic materials. The decrease of the bulk spin polarization may influence on the decrease of the interfacial scattering. The physical origin of the temperature dependence is an open question.

4) The dependence of the spin asymmetries and the spin diffusion length on the degree of B2 order was studied with the PSVs annealed at 400 °C, in which the CFAS film has the B2 order parameter S_{B2} of 0.53, whereas the film annealed at 500 °C does S_{B2} = 0.67. The CFAS films in the PSVs annealed at 400 °C had a bit smaller β and a shorter ℓ_{sf} than those at 500 °C. One the other hand, the fitting indicated a large change in the contribution of the interfacial scattering by the annealing temperature.

5) A considerable spin flip at the CFAS/Ag was indicated at from 50 K to room temperature by measuring the change of ΔRA of the samples with and without Ag(1 nm) insertion layer(s) in the CFAS magnetic layer. The suppression of the interfacial spin flip was observed below 30 K, which may indicate the spin flipping mechanism of the spin-orbit interaction along with the momentum scattering by phonon.

In summary, the bulk scattering of the CFAS film with an imperfect B2 ordered structure was limited within a few nm film range from the interface with the Ag spacer layer due to the short spin diffusion length even at low temperature. On the other hand, the the interfacial scattering at between CFAS and Ag largely contributed to the CPP-GMR. Since the degree of B2 order of the present CFAS films annealed at 500 °C was 0.7 at the most, the films with higher degree of order are expected to provide a much larger spin-dependent scattering not only for the bulk scattering but also for the interfacial scattering, thus larger CPP-GMR output should be obtained. The origin of the temperature dependence of the interfacial scattering, the mechanism of the interfacial spin fillip and its quantitative analysis are tasks to be solved in future.

References

[1] J. Bass, and W. P. Pratt, Jr., J. Magn. Magn. Mater. **200**, 274 (1999). J. Bass, and W. P. Pratt, Jr., J. Phys.: Condens. Matter **19**, 183201 (2007), and references therein.

[2] T. Kimura, and Y. Otani, Phys. Rev. Lett. **99**, 196604 (2007).

[3] W. Oepts, M. A. M. Gijs, A. Reinders, R. M. Jungblut, R. M. J. van Gansewinkel, and W. J. M. de Jong, Phys. Rev. B **53**, 14024 (1996).

[4] S. D. Steenwyk, S. Y. Hsu, R. Loloee, J. Bass, and W. P. Pratt, Jr., J. Magn. Magn. Mater. **170**, L1 (1997).

[5] A. C. Reilly, W. Park, R. Slater, B. Ouaglal, R. Loloee, W. P. Pratt, Jr., and J. Bass, J. Magn. Magn. Mater. **195**, L269 (1999).

[6] S. Maat, M. J. Carey, and J. R. Childress, J. Appl. Phys. **101**, 093905 (2007). *ibid*. **102**, 049902 (2007).

[7] S. Maat, M. J. Carey, and J. R. Childress, Appl. Phys. Lett. **93**, 143505 (2008).

[8] T. Taniguchi, H. Imamura, T. M. Nakatani, and K. Hono, Appl. Phys. Lett. (2011) **98**, 042503 (2011).

[9] C. Ahn, K.-H. Shin, R. Loloee, J. Bass, and W. P. Pratt, Jr., J. Appl. Phys. **108**, 023908 (2010).

[10] W. H. Butler, X. -G. Zhang, D. M. C. Nicholson, and J. M. MacLaren, Phys. Rev. B **52**, 13399 (1995).

[11] M. D. Stiles, J. Appl. Phys. **79**, 5805 (1996).

[12] Y. Sakuraba, K. Izumi, T. Iwase, S. Bosu, K. Saito, K. Takanashi, Y. Miura, K. Futatsukawa, K. Abe, M. Shirai, Phys. Rev. B **82**, 094444 (2010).

[13] K. M. Schep, J. B. A. N. van Hoof, P. J. Kelly, G. E. W. Bauer, and J. E. Inglesfield, J. Magn. Magn. Mater. **177–181**, 1166 (1998).

[14] M. D. Stiles, and D. R. Penn, Phys. Rev. B **61**, 3200 (2000).

[15] N.Hase, T. M. Nakatani, S. Kasai, Y. K. Takahashi and K. Hono, J. Appl. Phys. (2011) in press.

[16] H. Oshima, K. Nagasaka, Y. Seyama, Y. Shimizu, S. Eguchi, and A. Tanaka, J. Appl. Phys. **91**, 8105 (2002).

[17] H. Oshima, K. Nagasaka, Y. Seyama, Y. Shimizu, and A. Tanaka, Phys. Rev. B **66**, 140404(R) (2002).

[18] H. Yuasa, M. Yoshikawa, Y. Kamiguchi, K. Koi, H. Iwasaki, M. Takagishi, and M. Sahashi, J. Appl. Phys. **92**, 2646 (2002).

[19] K. Eid, W. P. Pratt, Jr., and J. Bass, J. Appl. Phys. **93**, 3445 (2003).

[20] H. Yuasa, H. Fukuzawa, H. Iwasaki, and M. Sahashi, J. Appl. Phys. **97**, 113907 (2005).

[21] H. Yuasa, H. Fukuzawa, and H. Iwasaki, J. Magn. Magn. Mater. **286**, 95 (2005).

[22] J. R. Childress, M. J. Carey, S. I. Kiselev, J. A. Katine, S. Maat, and N. Smith, J. Appl. Phys. **99**, 08S305 (2006).

[23] F. Delille, A. Mahchon, N. Strelkov, B. Dieny, M. Li, Y. Liu, P. Wang, and E. Favre-Nicolin, J. Appl. Phys. **100**, 013912 (2006).

[24] B. Dassonneville, R. Acharyya, H. Y. T. Nguyen, R. Loloee, W.P. Pratt, Jr., and J. Bass, Appl. Phys. Lett. **96**, 022509 (2010).

[25] L. Piraux, S. Dubois, A. Fert, and L. Belliard, Eur. Phys. J. B **4**, 413 (1998).

[26] R. J. Elliott, Phys. Rev. **96**, 266 (1954).

[27] Y. Yafet, in *Solid State Physics*, vol. 14, edited by F. Seitz and D. Turnbull, (Academic, New York, 1963), p. 2.

[28] I. Zutic and J. Fabian, Concepts in Spin Electronics, edited by S. Maekawa, (Oxford, 2006), p. 56–57.

[29] (for example) T. Ambrose, J. J. Krebs, and G. A. Prinz, Appl. Phys. Lett. **76**, 3280 (2000).

Chapter 6
CPP-GMR with NiAl spacer layer

6.1 Introduction

The band matching between the ferromagnetic and the nonmagnetic materials critically affects the interfacial spin-dependent scattering [1,2]. Although we have experimentally shown that the band matching between the B2-ordered $Co_2Fe(Al_{0.5}Si_{0.5})$ (CFAS) and Ag might be relatively good, there is still a large room to obtain better choices of the spacer layer materials showing better band matching. Indeed, Mryasov and Ambrose argued that nonmagnetic Heusler alloy could be a spacer layer for ferromagnetic Heusler alloys due to the potentially good band matching [3]. Simply speaking, their argument can be understood by comparing between the band dispersions of a Heusler alloy and a noble metal (*e.g.* Cu) as schematically shown in Fig. 6-1. The slopes of band dispersion curves are opposite between a Heusler alloy and Cu, thus there are a large difference in the electronic character between them. Thus, materials of well-band-matched spacer layer have to have the similar band dispersions to that of the ferromagnetic Heusler alloys. Mryasov and Ambrose have proposed a nonmagnetic Heusler alloy of Rh_2CuSn. Nikolaev *et al*. have reported CPP-GMR spin-valves with $Co_2MnGe/Rh_2CuSn/Co_2MnGe$ trilayer [4]. As shown in Fig. 6-2, the band dispersions of Co_2MnGe and Rh_2CuSn have similar slopes for the up spin band, which indicates a good band matching at the interface. They demonstrated the capability of to the read head for a recording density of 670 Gbit/in^2 [4].

The first criterion for spacer layer materials with good band matching with the ferromagnetic materials is considered to be the same crystal symmetry with that of the ferromagnetic layer. Thus, the $L2_1$ ordered *all Heusler trilayer* using nonmagnetic Heusler alloys for the spacer layer may be promising. However, obtaining $L2_1$ ordered Heusler alloy films may be difficult. On the other hand, as shown in Chapters 4 and 5, a

high spin-dependent scattering can be obtained even with B2 ordered Heusler alloys, like for the $Co_2Fe(Al_{0.5}Si_{0.5})$. Thus, the *all L2$_1$ Heusler trilayer* may not necessary to achieve the good band matching. Instead, a*ll B2 trilayer* may provide a better band matching than those with Heusler alloy magnetic layers and the spacer layers of noble metals. So far, there is not report on CPP-GMR devices using binary alloys either B2 or other ordered structures for the spacer layer.

In this chapter, we focus on a NiAl intermetallic compound with the B2 ordered intermetallic compound and studied the capability to the spacer layer with the CFAS magnetic layers.

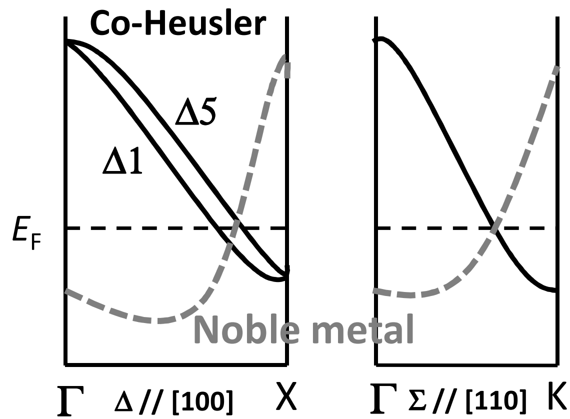

Fig. 6-1 Schematic band dispersions of Co based Heusler alloys for the up spin (solid line) and noble metal (broken line). The opposite slopes of the curves indicate a mismatching of the band structure.

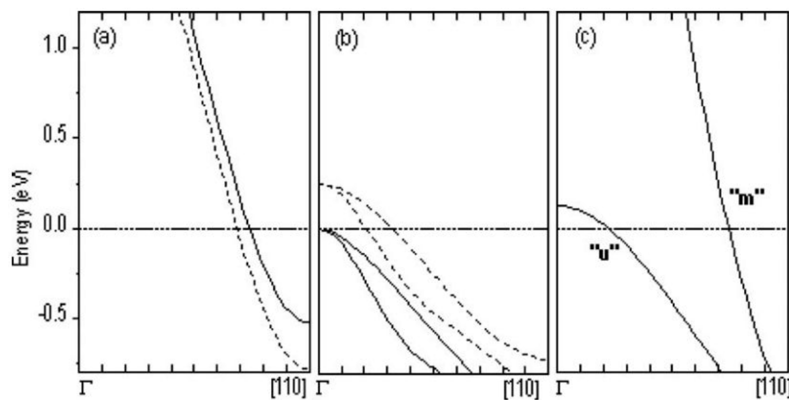

Fig. 6-2 Proposed matching of the band dispersion for **k** along [110]. (a) Co_2MnGe majority spin, (b) Co_2MnGe minority spin, and (c) Rh_2CuSn. By Nikolaev *et al.* [4].

6.2 Choice of NiAl B2 intermetallic compound

The material which may have a good band matching is required to have

(i) a similar band electronic structure with ferromagnetic Heusler alloys,

(ii) a similar lattice parameter with ferromagnetic Heusler alloys,

(iii) a chemical stability and a heat-resistance.

Although there are a lot of B2 ordered alloys or intermetallic compounds, NiAl intermetallic compound seems to be one of the few materials which may satisfy the criteria. The band structure has been studied both theoretically and experimentally [5]. Despite the ferromagnetic constituent of Ni, the 3*d* band of NiAl is fully occupied with electrons, thus the electronic character near the Fermi level is rather *s*-like. The density of state near the Fermi level is low, which is similar to that of CFAS. The carrier type has been clarified to be hole-like as well as some of Heusler alloys [5]. The lattice parameter of NiAl is 0.2886 nm [6], which is close to that of $Co_2Fe(Al_{0.5}Si_{0.5})$, $a_{CFAS}/2$ = 0.284 nm [7]. As seen in the Ni–Al phase diagram, the ordered NiAl phase is stable up to the melting point of 1638 °C [6], which is by the large negative enthalpy of mixing between Ni and Al of –59 kJ/atom at room temperature [8]. The magnetic property has been clarified to be Pauli paramagnetic due to the independence of the magnetic susceptibility of temperature [9].

Due to these physical and metallurgical properties of NiAl, we decided to apply NiAl to the spacer layer for the CPP-GMR devices with the CFAS magnetic layers.

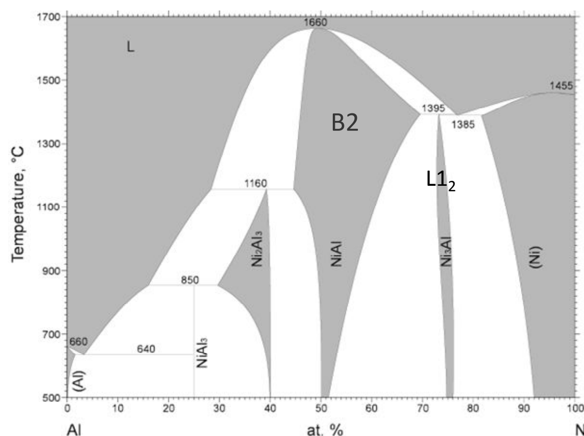

Fig. 6-3 Ni–Al binary phase diagram.
From ASM Alloy Phase diagrams Center.

Fig. 6-4 Calculated band dispersion of NiAl B2 phase by Lui *et al.* [5].

6.3 Fabrication of the exchange biased spin-valve

6.3.1 Sputtering deposition of NiAl film

The sputtering condition of the NiAl films was optimized. Fig. 6-5 shows the θ–2θ profiles of 50 nm thick NiAl films directly deposited on MgO(001) substrates by four sputtering conditions. As seen from the intensities of the 001 and 002 peaks of NiAl, the out-of-plane texture strongly depended on the sputtering condition. Although the optimization of the deposition condition was investigated only for several conditions, sputtering with a low dc power and in a low Ar atmosphere was good in our sputtering apparatus. A sputtering condition with the dc 10 W power under the Ar 4 mTorr atmosphere was used for the deposition of NiAl. The film composition deposited by this sputtering condition was determined to be $Ni_{51.1}Al_{48.9}$ (in at.%) by the ICP mass analysis. In addition, the NiAl film grew flatly on the MgO substrates. The average roughness (R_a) of the NiAl(50 nm) as-deposited film on the MgO substrate was 0.15 nm.

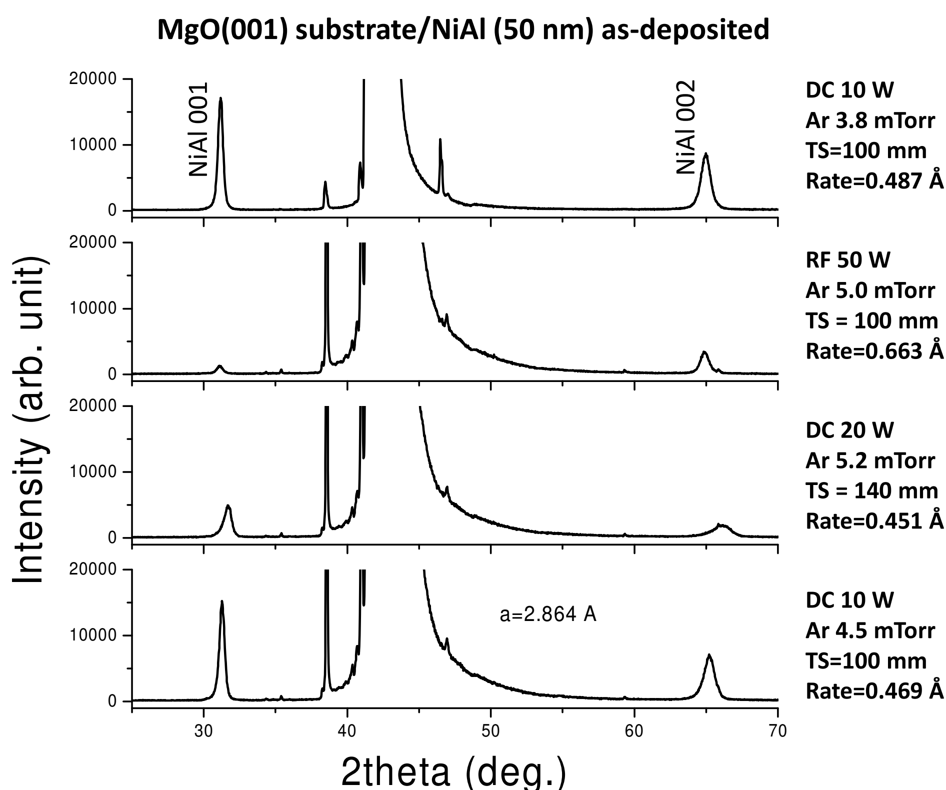

Fig. 6-5 θ-2θ scan profiles of NiAl(50 nm) films deposited on a MgO(001) single crystalline substrate by various deposition conditions (as-deposited). TS is the target-substrate distance.

6.3.2 Layer structure of the spin-valve

The film stack of the exchange biased spin-valve is the same as those with the Ag spacer layer. Cr(10 nm)/Ag(100 nm)/CFAS(5 or 20 nm)/NiAl(t_N)/CFAS(5 nm)/$Co_{50}Fe_{50}$(1 nm)/IrMn(10 nm)/Ru(8 nm) were deposited on a MgO(001) substrate. The Cr/Ag underlayer was *in situ* annealed at 300 °C for 30 min to obtain the flat surface. The rests of the layers were deposited at room temperature. The films were annealed at 500 °C for 30 min under a magnetic field of 5 kOe. The reason of the thick CFAS free layer (20 nm) for some samples is to obtain antiparallel magnetization against a ferromagnetic interlayer coupling through the NiAl spacer as mentioned in 6.3.4.

6.3.3 Structural characterizations

Figure 6-6 shows the θ–2θ scan profile of the spin-valve of Cr(10 nm)/Ag(100 nm)/CFAS(5 nm)/NiAl(4 nm)/CFAS(5 nm)/CoFe(1 nm)/IrMn(10 nm)/Ru(8 nm) annealed at 500 °C. The diffraction peaks from the NiAl layer and the CFAS layer overlap. This is considered to be due to the growth of the CFAS/NiAl/CFAS trilayer with almost identical lattice parameters perpendicular to the plane. The out-of-plane lattice parameter was estimated to be a = 0.2826 nm from the CFAS(004) and NiAl(002) peaks. The diffraction peak around $2\theta = 31°$ is the B2 superlattice diffraction. The intensity of this peak was much higher than that of the spin-valve with a Ag spacer layer. Thus, it appears that the peak composed of both the CFAS 002 and the NiAl 001 B2 superlattice diffractions. Microbeam diffraction was taken to confirm the B2 order in the NiAl spacer layer as shown below. The satellite peaks around the B2 peak and the fundamental peak are attributed to the combination of the layer thickness of CFAS(5 nm)/NiAl(4 nm)/CFAS(5 nm). Indeed, such strong satellite peaks do not appear in the profile of the spin-valve with the CFAS(20 nm) free layer.

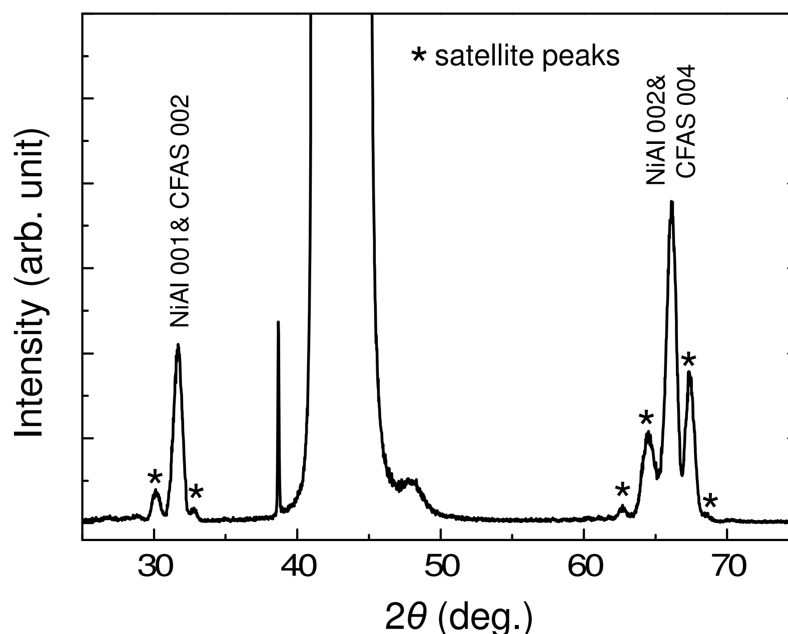

Fig. 6-6 θ-2θ scan profile of MgO substrate/Cr(10)/Ag(100)/CFAS(5)/NiAl(4)/CFAS(5)/CoFe(1)/IrMn(10)/Ru(8) (thickness in nm) spin-valve annealed at 500 ℃ for 30 min.

The multilayer structure of the spin-valve was studied by transmission electron microscopy. The sample is the spin-valve with CFAS(5 nm)/NiAl(4 nm)/CFAS(5 nm) trilayer, which is the same as that shown in Fig. 6-6. Figure 6-7(a) shows a bright field image with the two-beam condition of $\boldsymbol{g}$ = [220] of CFAS and [110] of NiAl parallel to the film plane. In this diffraction condition, the strain parallel to the film plane such as those by the lattice misfit should show the diffraction contrast. In Fig. 6-7(a), there is no diffraction contrast either at the CFAS/Ag interface or in the films of CFAS and Ag, indicating the absence of strain in the CFAS/Ag/CFAS trilayer. This is probably due to the growths of the NiAl spacer layer on the CFAS layer and vice versa with keeping the same lattice parameter as shown by XRD. The high resolution image (Fig. 6-7(b)) shows that there is no misfit dislocation, although the contrast between the CFAS and NiAl layers are small due to the close average masses. The crystalline structure of the NiAl spacer layer was examined by taking microbeam diffraction as shown in Fig. 6-7(c). The 100 spots clearly indicate the B2 order of the NiAl spacer layer. Form the results of XRD and TEM, we can conclude that the crystalline structure is B2 through the CFAS/NiAl/CFAS trilayer.

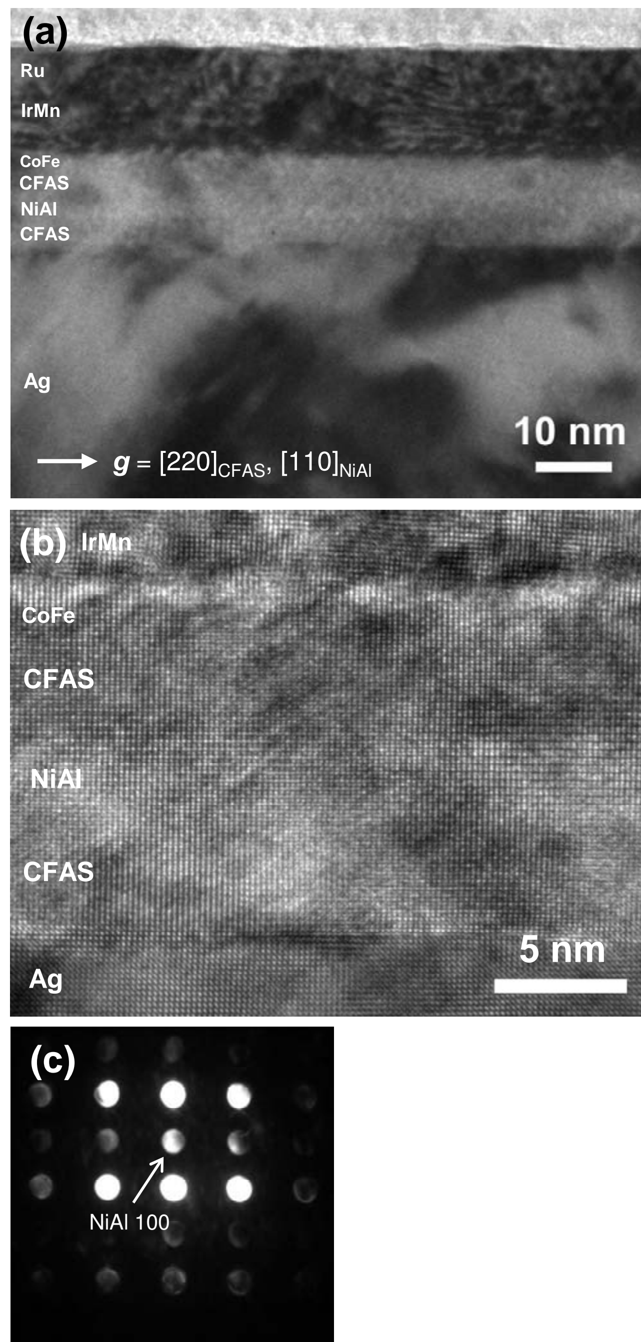

Fig. 6-7 TEM micrographs of MgO substrate/Cr(10)/Ag(100)/CFAS(5)/NiAl(4)/CFAS(5)/CoFe(1)/IrMn(10)/Ru(8) (thickness in nm) spin-valve annealed at 500 ℃ for 30 min. (a) bright field image with the two-bean condition of $\boldsymbol{g}$ = $[220]_{CFAS}$, $[110]_{NiAl}$, (b) high resolution image, and (c) microbeam diffraction pattern from the NiAl spacer layer.

6.3.4 Magnetization behavior

Figure 6-8 shows the magnetization behavior of the spin-valves of CFAS(5 nm) free layer/NiAl(t_N)/CFAS(5 nm) pinned layer (t_N = 2.5, 4.0, 7.0, 10 nm). The hysteresis curve of the spin-valve with the NiAl(2.5 nm) spacer layer shows a shift from the zero external field due to the exchange bias of the IrMn pinning layer. However, it does not show the antiparallel magnetization configuration between the free and the pinned layers. This is attributed to a ferromagnetic interlayer coupling between the free and the pinned CFAS layers through the NiAl spacer layer, by which the magnetizations of the free and the pinned layers rotate simultaneously. In the spin-valve with t_N = 4.0 nm, the hysteresis curves of the free layer and the pinned layer are separated, but the antiparallel magnetization configuration is not perfectly obtained because of the ferromagnetic coupling. The ferromagnetic coupling still remains in t_N = 7.0 nm as indicated by the incompleteness of the antiparallel magnetization state between the free layer and the pinned layer. The thickness of 7.0 nm seems unusually thick to maintain a ferromagnetic interlayer coupling. The ferromagnetic coupling is decoupled in the spin-valve with the NiAl spacer layer of 10 nm as indicated by the very flat plateau of the antiparallel magnetization state. The energy of the ferromagnetic interlayer coupling was roughly estimated by the relationship of

$$H_{\text{shift}} = \frac{J}{M_S t_F}, \qquad (6.1)$$

where H_{shift} is the shift of the hysteresis loop of the free layer from the zero external field as schematically shown in Fig. 6-9(a), J is the interlayer coupling energy, M_s is the saturation magnetization of the free layer, and t_F is the free layer thickness. In these devices, M_s = 1100 emu/cc and t_F = 5 nm. The interlayer coupling energy can be estimated only in the magnetization curves in which the magnetization rotations between the free and pinned layers are separated. Thus, the estimation of J is valid for the devices of t_N = 4.0 and 7.0 nm, and the values of J were 0.02 and 0.04 erg/cm^2, respectively (Fig. 6-9). By applying Eq. (6.1) to the magnetization curve of the spin-valve with t_N = 2.5 nm, J is estimated to be 0.07 erg/cm^2. However, this is underestimated because the hysteresis loops of the free layer and the pinned layer are not separated. As shown in Fig. 6-9(b), the effective pinning field of the IrMn films decreases with decreasing the NiAl spacer layer thickness due to the ferromagnetic coupling. The origin of the ferromagnetic coupling is not clear at the present. The interfacial roughness between the ferromagnetic and nonmahnetic layers often causes a

ferromagnetic interlayer coupling, the so-called orange peel coupling [10][11]. However, the values of H_{shift} for the 5 nm thick free layer of up to 120 Oe in the present spin-valves seems to be too large to be derived from the orange peel coupling, which is typically less than a few 10 Oe [10][11]. In addition, we have confirmed that the CFAS film on the Ag underlayer was very flat (R_a ~ 0.1 nm, p–v ~ 1 nm) using an atomic force microscope. Therefore, the ferromagnetic coupling is considered to be intrinsic by the combination of the electronic structures of CFAS and NiAl rather than by the interfacial roughness.

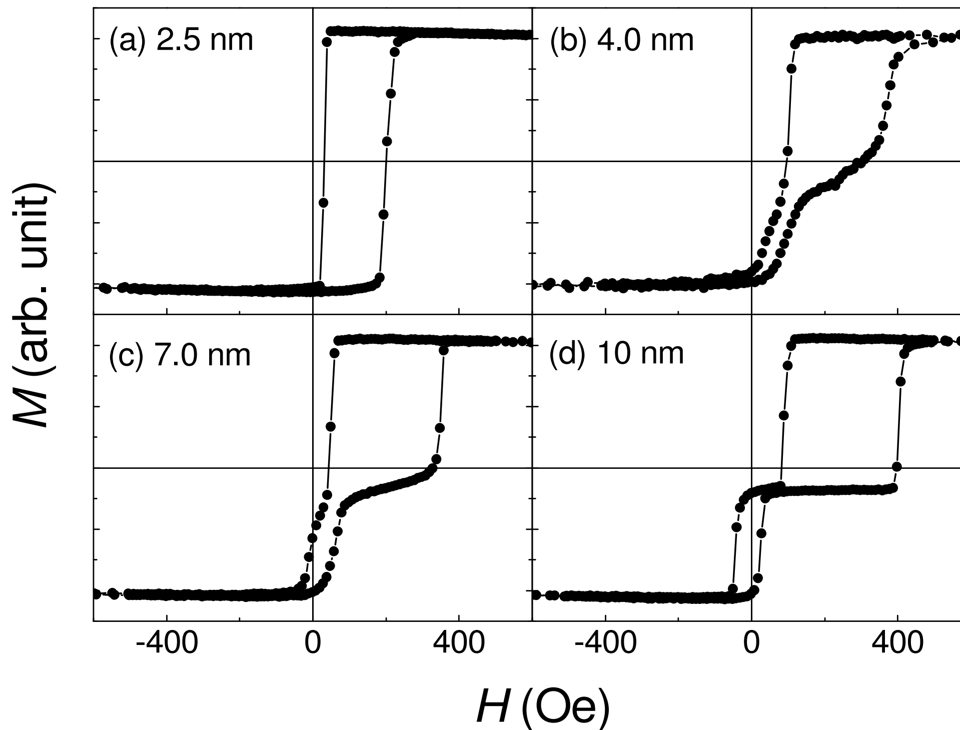

Fig. 6-8 Magnetization curves of CFAS(5 nm)/NiAl(t_N)/CFAS(5 nm)/CoFe(1 nm)/IrMn(10 nm) the spin-valves with various NiAl spacer layer thicknesses t_N = 2.5–10 nm measured at room temperature.

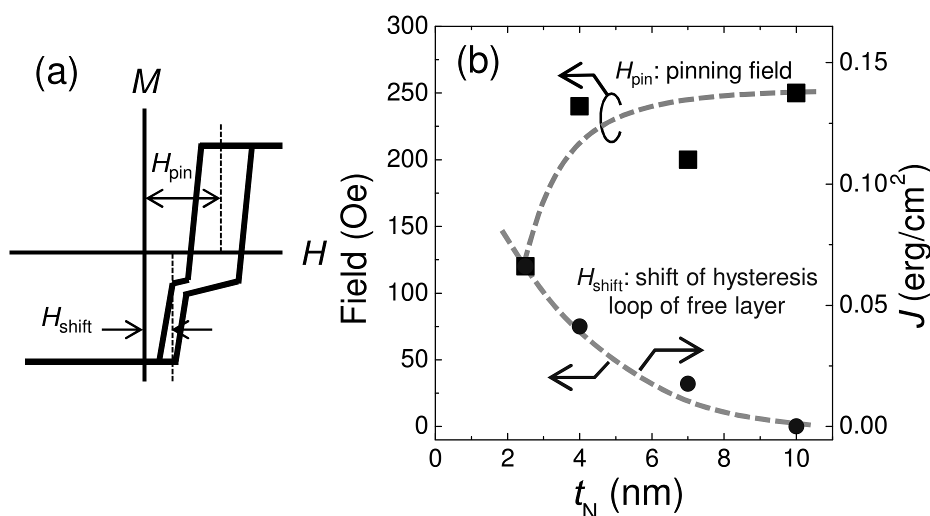

Fig. 6-9 (a) Schematic magnetization of the spin-valve and the definitions of the shift of the hysteresis loop of the free layer (H_{shift}) and the pinning field (H_{pin}). (b) The values of H_{shift}, H_{pin} and the ferromagnetic interlayer coupling energy J as a function of the NiAl spacer layer thickness.

6.3.5 CPP-GMR property

The CPP-GMR properties were measured at room temperature with a sense current of 0.1 mA. Figure 6-10 shows the MR curve of the spin-valve with the NiAl (4 nm) spacer annealed at 500 °C for 30 min. The Ar ion etching to fabricate the pillars was stopped when the Ag underlayer appeared. Thus, the whole the CFAS/NiAl/CFAS trilayer was fabricated into pillars. The pillar size of the device shown in Fig 6-10 was 0.10 μm×0.20 μm ellipse. Although a sufficient antiparallel magnetization state could not be obtained in the unpatterned film due to the ferromagnetic interlayer coupling between the pinned and the free layers (Fig. 6-8(b)), the CPP-GMR pillar showed a rather stable antiparallel magnetization state by the magnetostatic coupling between the two CFAS layers. The resistance change–area product (ΔRA) and the MR ratio were 4.5 m$\Omega\mu$m^2 and 13.8%, respectively. On the other hand, the spin-valve device with a Ag (5 nm) spacer layer and an identical structure for the other layers showed ΔRA of 6.8 m$\Omega\mu$m^2 and an MR ratio of 21% at RT (Fig. 4-14). Thus, unfortunately, the spin-valve with the NiAl(4 nm) did not show a CPP-GMR output as high as that with the Ag spacer layer.

In order to study the effect of the NiAl spacer layer thickness on ΔRA, spin-valves with t_N = 2.5, 4.0 and 10 nm were fabricated and measured at room temperature. In

these devices, the 20 nm thick CFAS free layers were used in order to obtain the antiparallel magnetization state even with the strong ferromagnetic interlayer coupling for t_N = 2.5 nm. The pillar etching was done up to the spacer layer for obtaining the large magnetic moment of the free layer so that the large Zeeman energy of the free layer realizes the antiparallel magnetization state. The difference in ΔRA between the spin-valves with the free layer thicknesses of 20 nm and 5 nm was small, *i.e.* 5.0 m$\Omega\mu$m^2 for 20 nm thick free layer and 4.5 m$\Omega\mu$m^2 for 5 nm thick free layer, the NiAl spacer layer was 4 nm for both. This small difference in ΔRA is due to the short spin diffusion length of the CFAS alloy layer of ~ 2.2 nm at RT as studied in Chapter 5. The device with the NiAl spacer of t_N = 2.5 nm showed ΔRA of 6.5 m$\Omega\mu$m^2, which is considerably higher than that with t_N = 4.0 nm and comparable to that of the spin-valves with the CFAS layers and the Ag spacer layer. On the other hand, the device with t_N = 10 nm only showed ΔRA of 2.5 m$\Omega\mu$m^2. The reduction of ΔRA with increasing t_N is thought to be due to the spin relaxation within the NiAl spacer layer. The spin diffusion length of the NiAl film ℓ_{sf} was estimated by the phenomenological relationship of

$$\Delta RA(t_N) = \Delta RA_0 \times \exp(-t_N / \ell_{sf}), \qquad (6.2)$$

where ΔRA_0 is ΔRA extrapolated into t_N = 0 [12]. The fitting by Eq. (2) yielded ℓ_{sf} ~ 8 nm and ΔRA_0 ~ 8.5 m$\Omega\mu$m^2. The spin relaxation was not given rise to be a problem in devices with Ag spacer layers due to the long spin diffusion length up to several hundred nm [13]. Thus, the reason of the lower CPP-GMR with the NiAl(4 m) spacer layer than that of the Ag spacer layer is not the lower scattering spin asymmetry but the spin memory loss in the spacer layer. Note that the value of ΔRA_0, which is the value when there is no spin relaxation in the spacer layer, is higher than the value of ΔRA using the Ag spacer layer. Thus, a higher ΔRA would be obtained by using a thinner NiAl spacer layer where the spin memory loss becomes negligibly small.

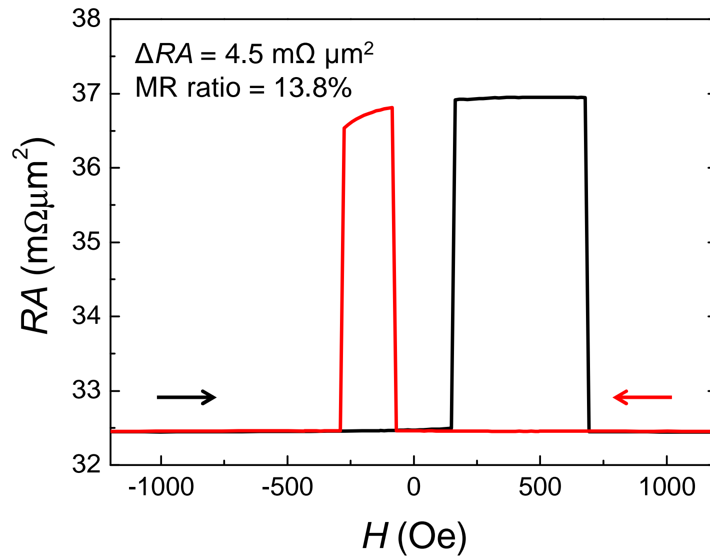

Fig. 6-10 CPP-GMR curve of the spin-valves with CFAS(5 nm)/NiAl(4 nm)/CFAS(5 nm) trilayer measured at room temperature.

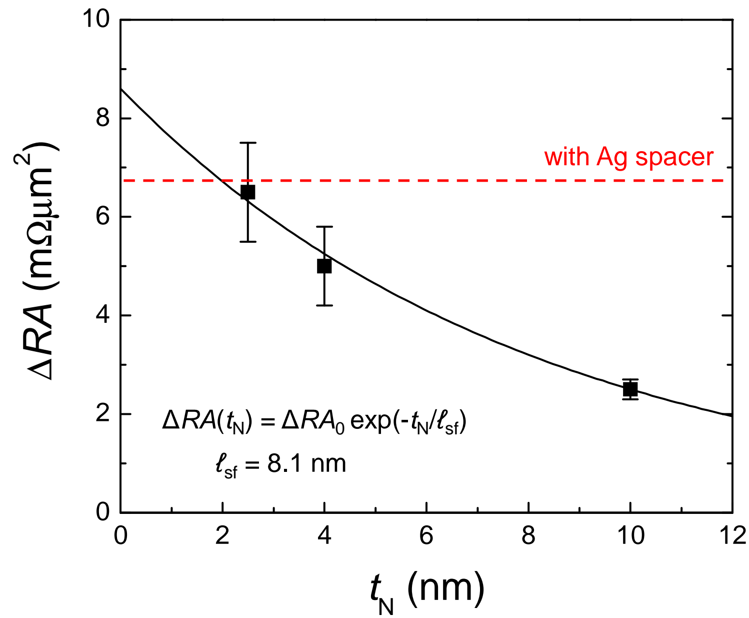

Fig. 6-11 Dependence of ΔRA at room temperature on the NiAl spacer layer thickness t_N in the spin-valves of CFAS(20 nm) free layer/NiAl(t_N)/CFAS(5 nm)/CoFe(1 nm)/IrMn(10 nm).

6.4 Discussion

6.4.1 Band matching at the CFAS/NiAl interface

As seen in Fig. 6-11, ΔRA might be higher than those with the Ag spacer layer in the spin-valve with a very thin NiAl spacer layer, although it was difficult because of the strong ferromagnetic coupling between CFAS layers. The difference in the spacer layer material should influence the spin asymmetry of the interfacial scattering which is derived from the difference in the band structure between the ferromagnetic and nonmagnetic materials. Therefore, the expected enhancement of ΔRA by using the thin NiAl spacer layer might from a better band matching at the CFAS/NiAl interface than that at the CFAS/Ag interface. This may originate from the difference of the crystallographic symmetry between the fcc Ag and the B2 NiAl for the CFAS FM layers with the B2 structure. Theoretical works on the electric transports through the CFAS/NiAl and the CFAS/Ag heterostructures are anticipated for the clarification of the band matching.

6.4.2 A way to obtain a larger CPP-GMR with the NiAl spacer layer

Although a large ΔRA is expected as seen in Fig. 6-11, making the NiAl spacer layer thinner disable us to obtain the antiparallel magnetization state. Thus, making the spin diffusion length of the NiAl film is a more realistic way to achieve larger CPP-GMR output. The short spin diffusion length of the NiAl spacer layer may originate from the high resistivity of the NiAl film of ρ = 40 μΩcm. This is much higher than that reported for the bulk stoichiometric alloy is ρ ~ 10 μΩcm at RT [9]. The origin of the larger resistivity of the film may be the chemical disorder, impurities or a strain, which can be improved by optimizing the target purity and the deposition condition etc. As mentioned by Bass and Pratt, Jr. [13], there is an empirical relationship for both nonmagnetic and ferromagnetic materials that the spin diffusion length is proportional to the inverse resistivity, namely conductivity. Therefore, if the resistivity of the NiAl film can be reduced by improving the fabrication processes, the spin diffusion length may become longer, which leads to higher CPP-GMR outputs.

6.5 Summary of this chapter

In this chapter, NiAl B2 intermetallic compound was first applied to the spacer layer with the $Co_2Fe(Al_{0.5}Si_{0.5})$ (CFAS) layers. The CPP-GMR property was compared with that with the Ag spacer layer qualitatively. The findings and the achievements are as follows.

1) A CFAS/NiAl/CFAS trilayer nearly free from defects and strain was successfully fabricated due to the small lattice mismatch of 1.5%. The B2 structure through the trilayer was confirmed by XRD and TEM.

2) A ferromagnetic interlayer coupling was observed in the CFAS/NiAl/CFAS trilayer, which remains even for the NiAl spacer layer of 7 nm. Due to the flat CFAS/NiAl interfaces, the interlayer coupling may be intrinsic phenomenon for the combination of CFAS and Ag, not by an orange peel coupling.

3) CPP-GMR spin-valves were successfully fabricated. The dependence of ΔRA on the NiAl spacer thickness was examined. The device with a 2.5 nm thick NiAl spacer showed almost the same value of ΔRA as that with the Ag spacer layer. However, ΔRA decreased with increasing NiAl spacer layer thickness due to the short spin diffusion length of the NiAl film which was estimated to be ~ 8 nm.

4) A larger CPP-GMR output than those with the Ag spacer layers is expected if the spin relaxation in the NiAl spacer layer can be suppressed. This may indicate a larger interfacial scattering at CFAS/NiAl than that at CFAS/Ag due to a good band matching. The improvement of the short spin diffusion length of the NiAl spacer layer is necessary to obtain the large CPP-GMR output experimentally.

References

[1] W. H. Butler, X. -G. Zhang, D. M. C. Nicholson, J. M. MacLaren, Phys. Rev. B **52**, 13399 (1995).

[2] M. D. Stiles, J. Appl. Phys. **79**, 5805 (1996).

[3] O. Mryasov and T. Ambrose, Half-metallic Alloys: Fundamentals and Applications, Lecture Notes in Physics, Vol. 676, I. Galanakis, D. H. Dederichs (Eds.), Springer, Berlin-New York, 2005, pp. 187-219.

[4] K. Nikolaev, P. Kolbo, T. Pokhil, X. Peng, Y. Chen, T. Ambrose, O. Mryasov, Appl. Phys. Lett. **94**, 222501 (2009).

[5] S. -C. Lui, J. W. Davenport, E. W. Plummer, D. M. Zehner, G. W. Fernando, Phys. Rev. B **42** (1990) 1582.

[6] Y. I. Dutchak, V. G. Chekh, Russ. J. Phys. Chem. **55**, 1326 (1981).

[7] T. M. Nakatani, A. Rajanikanth, Z. Gercsi, Y. K. Takahashi, K. Inomata, K. Hono, J. Appl. Phys. **102**, 033916 (2007).

[8] F.R. de Boer, R. Boom, W.C.M. Mattens, A.R. Miedema, and A.K. Niessen, Cohesion in Metals: Transition Metal Alloys, North Holland, 1988.

[9] L. P. Zelenin, A. N. Bashkatov, F. A. Sidorenko, P. V. Gel'd, Fiz. metal. metalloved., **30**, 740 (1970).

[10] J. C. S. Kools, W. Kula, D. Mauri, T. Lin, J. Appl. Phys. **85** (1999) 4466.

[11] K. Y. Kim, S. H. Jang, K. H. Shin, H. J. Kim, T. Kang, J. Appl. Phys. **89** (2001) 7612.

[12] N. Strelkov, A. Vedyaev, B. Dieny, J. Appl. Phys. **94** (2003) 3278.

[13] J. Bass, and W. P. Pratt, Jr., J. Phys.: Condens. Matter **19**, 183201 (2007).

Chapter 7 Summary

Current-perpendicular-to-plane giant magnetoresistance (CPP-GMR) devices are considered to be one of the key technologies to realize the ultrahigh density magnetic recording over Tbit/in^2. For that, the magnetoresistive output has to be improved by developing the materials. This thesis work was conducted to clarify the spin-dependent scattering characteristics of the CPP-GMR devices using $Co_2Fe(Al_{0.5}Si_{0.5})$ (CFAS). The results are summarized as follow:

1) The fabrication process of the CFAS films and the biased spin valves were established. Almost stoichiometric $Co_2FeAl_{0.5}Si_{0.5}$ films were successfully obtained on the Cr/Ag underlayer by tuning the CFAS alloy target, which enabled us to obtain the magnetization of 1100 emu/cc in the 10 nm thick film annealed at 500 °C, which is close to the Slater-Pauling value. The degree of B2 order was estimated to be up to S_{B2} ~ 0.7 after annealing at 500 °C. The L21 ordering was not found in the films annealed up to 500 °C.

2) An oscillatory antiferromagnetic interlayer coupling was found in CFAS/Ag/CFAS trilayers. The antiferromagnetic coupling appeared only in annealed trilayers at 400–500 °C with the Ag thicknesses of t_N ~2.0 nm and ~3.4 nm, namely the oscillation period was ~1.4 nm. The interlayer coupling vanished for t_N > 4 nm, so that the 5 nm thick Ag layer was chosen for the spacer layer of the spin-valves in this work.

3) Relatively large CPP-GMR outputs were obtained both in exchange biased spin-valves and pseudo spin-valves. Especially, the pseudo spin-valve with a CFAS(2.5 nm)/Ag(5 nm)/CFAS(2.5 nm) trilayer annealed at 500 °C showed ΔRA and MR ratio of 11 mΩμm^2 and 80% at 14 K and 5 mΩμm^2 and 34% at 290 K. Obtaining large CPP-GMR outputs is a critical matter for the read head application,

thus these results are promising for the application. In addition, the large dependence of the CPP-GMR output on the degree of B2 order of the CFAS films was revealed. Since the CFAS films show high degree of B2 order by annealing at higher than ~450 °C which is too high for the read head manufacturing process, materials showing high degree of order are very important for the realizations of the devices using Heusler alloys.

4) The spin-dependent scattering characteristics of the CPP-GMR in CFAS/Ag/CFAS pseudo spin-valves were analyzed by the Valet-Fert model. The bulk scattering spin asymmetry β, the interfacial scattering spin asymmetry γ, and the spin diffusion length of the CFAS film ℓ_{sf} were estimated to be β = 0.77 (0.70), γ = 0.93 (0.77), and ℓ_{sf} = 3.0 nm (2.2 nm) at 14 K (209 K), respectively. The relatively large β and the high resistivity of CFAS films of ρ_F = 62 μΩcm (71μΩcm) at 14 K (290 K) provided a large contribution of the bulk scattering to CPP-GMR per unit thickness of the magnetic layer. However, the spin diffusion length, which is much shorter than those of the conventional 3*d* magnetic alloys (*e.g.* ~5.5 nm of NiFe and ~ 12 nm of CoFe), effectively limited the contribution of the bulk scattering within a few or several nm range of the CFAS layer from the interface with the Ag spacer layer. On the other hand, the large contribution of the interfacial scattering was revealed, by which the large CPP-GMR outputs were obtained even with very thin CFAS layers. The large γ and the small interfacial resistance at CFAS/Ag of $AR_{F/N}$ ~ 0.25 mΩμm^2 may indicate a good band matching of the electronic band structure for the up spin at the CFAS/Ag interface. Thus, Ag is considered to be a relatively good spacer material for the CFAS Heusler alloys to obtain a large spin asymmetry of the interfacial scattering.

5) A presence of the spin flip at the CFAS/Ag interface was implied by measuring CPP-GMR for the samples with very thin Ag(1 nm) insertion(s) in the CFAS magnetic layer(s). The rapid increases of ΔRA in the samples with the Ag insertion(s) were observed at low temperature (below 30 K), indicating a suppression of the spin flip at the interface. This may be because the phonon scattering was frozen at low temperature, so that the spin flip scattering by the spin-orbit interaction at the CFAS/Ag interface was suppressed. The detailed mechanism of the interfacial spin flip has to be clarified, which will be important even practically to find the way to improve the large temperature dependence of

ΔRA in Heusler alloy based CPP-GMR devices.

6) The B2 intermetallic compound NiAl was first investigated for spacer layers based on the expectation that *all B2 trilayer* might provide a better band matching with B2 ordered CFAS Heusler alloy layers, and on the reported electronic structure of NiAl. Despite the short spin diffusion length of the NiAl films of ~8 nm, ΔRA using NiAl(2.5 nm) spacer layers showed a comparable value to that with the Ag spacer layer. A higher value is expected by making the NiAl spacer thinner, although the strong ferromagnetic coupling through the thin NiAl spacer layer disabled us to obtain the antiparallel magnetization state. Therefore, the band matching between CFAS and NiAl could be potentially better than that with Ag. Since the resistivity of the present NiAl films have four times higher resistivity than that in the bulk alloy, the improvement of the resistivity is considered to be a key to suppress the spin relaxation in the NiAl spacer layer, thus to obtain a larger CPP-GMR output.

This work showed the potential of the CPP-GMR devices with Heusler alloys. However, the MR output achieved so far is not high enough for the applications even with epitaxial films annealed at high temperatures. Thus, further development of the materials is required. Although a relatively large CPP-GMR was obtained in this work, the $Co_2Fe(Al_{0.5}Si_{0.5})$ films had the degree of B2 order of only 70% (S_{B2} = 0.7) even after the annealing at 500 °C. Thus, if the degree of order is improved, a higher CPP-GMR output should be achieved. New alloy compositions, some additive elements which promote the ordering, or new fabrication processes have to be tried for innovations. Moreover, the materials for the spacer layer must have a lot of rooms to be developed. A strategy to enhance CPP-GMR by the contribution of the interfacial scattering may be to obtain a combination of materials showing a large interfacial resistance as well as a large γ. Then, a large ΔRA by the interfacial scattering, which is represented as $\gamma^2 AR_{F/N}/(1-\gamma^2)$ per an interface, is obtained. Up to now, only metals and alloys have been studied for the spacer layer of CPP-GMR devices. Some other kinds of materials, *e.g.* semiconductor based conducting materials or semimetals, might provide both large resistances and large spin asymmetries at the interfaces with Heusler alloy magnetic layers.

Appendix: Perspective of CPP-GMR research

At the end of this thesis, I would like to mention the perspectives of the future CPP-GMR research which could be key technologies to realize ultrahigh density magnetic recording.

The MR output of currently achieved CPP-GMR devices with Heusler alloys including this work are still inferior to those required for read heads capable to over $Tbit/in^2$ recording density. Thus, further development of materials for both magnetic layer and nonmagnetic spacer layer are required. Moreover, reducing the annealing temperature for the chemical order of Heusler alloys is a very important point of view for the device application. Currently, the annealing temperature available in the read head fabrication is limited by two aspects; (i) the pinning force of the spin-valve, and (ii) the thermal stability of the soft magnetic shield layer. Synthetic antiferromagnetic layers (typically, composed of CoFe/Ru/CoFe) are used in read head spin-valves to obtain a high pinning force and a free magnetization rotation of the free layer. High annealing temperature induces a strong ferromagnetic coupling through the very thin Ru layer and an interdiffusion of Mn from the antiferromagnetic layer. Therefore, the typical annealing temperature in the read head manufacturing process is limited up to 300 °C. In addition, a high temperature annealing degrades the soft magnetic property of the shield (currently, permalloy), thus the reading resolution is degraded.

The other severe requirement to read heads is that the total layer structure of the read head has to fit the read gap which is the gap between two shields composed of a soft magnetic material (currently permalloy). This is because the read gap determines the reading resolution of the head. For example, a simulation carried out by Takagishi *et al*. has predicted the read gap to be 20 nm for 2 $Tbit/in^2$ and 13.5 nm for 5 $Tbit/in^2$ [1]. These values may be hard for the exchange biased spin-values to achieve because of the thicknesses of the antiferromagnetic layer (at least ~6 nm) and the pinned layer (2–3 nm) which are required for a strong pinning force. Thus, the spin-valves will come up against a limitation to be applied to read head for ultrahigh density magnetic recording regardless of the reading device (TMR or CPP-GMR). The proposed solutions are the differential spin-valve [2], the non-local spin-valve [3], and the trilayer head [4][5].

The differential spin-valve has two reference (pinned) layers (RL) and two free layers (FL) separated by a gap layer, namely shield/AF/RL/N-spacer/FL/N-gap /FL/N-spacer/RL/AF/shield, where AF and N are antiferromagnet and nonmagnetic, respectively. The pinning directions of the reference layers are opposite each other. The

sensor gives a pulse-like signal when the two free layers stride across the boundary of the recording bits with the opposite magnetization directions. The advantage of the differential head is that the reading resolution is determined by the thickness of the FL/GL/FL not by the shield-to-shield gap. Thus, making the total thickness of the device thinner is not important for differential spin-valve to increase the reading resolution. However, microfabricating films composed of many layers into the required size of the read head (strip height and element width) would be a big technical challenge.

The non-local spin valve (NLSV) (or called spin accumulation read head) has a completely different structure from that of the conventional spin-valve. In the conventional spin-valve (local spin-valve), the parts of the spin injection and the detection are common, whereas the NLSV has the detection part apart from the spin injection part. The advantages of the NLSV will be as follows; (i) the resolution is determined by the size of the detector, (ii) a good scaling since a smaller distance between the injector and the detector provides a larger sense output, (iii) the sense part is electric current non-related, thus there is no spin torque induced noise. There are still rooms to study the fundamental aspects of the NLSV Thus, it may appear as a second next generation read head.

The trilayer read head (or called dual free-layer head, scissors-type head) has a simple structure of F/N or barrier/F. The two F layers are coupled antiferromagnetically by a magnetostatic coupling (for metal spacer and tunnel barrier) or/and an interlayer exchange coupling (only the case of metal spacer). A hard bias is attached to make the magnetization angle between the free layers 90°. Thus, the magnetizations of the free layers move like blades of scissors according to the field from the recording bits. Due to the thin thickness of the trilayer, it is easy to fit the read gap, therefore very thin and small read sensors can be fabricated. Another advantage of the trilayer read head is that the noise induced by the spin torque can be cancelled by the antiferromagnetic coupling, thus a higher signal to noise ratio (SNR) can be obtained. Zhou reported a simulation of the spin torque effect in a trilayer sensor composed of a magnetic tunnel junction, where the free layers are magnetostatically coupled [5]. At the nearly antiparallel magnetization configuration, the fluctuations of the moments of the free layers resonant, thus net spin torque noise is canceled. This is very advantageous for the read head application. Although the simulation by Zhou showed that the reduction of the noise was achievable even by the magnetostatic coupling between the free layers, a stronger coupling by an interlayer exchange coupling would provide a more efficient cancelation

of the noise.

The absence of the antiferromagnetic pinning layer in the trilayer read heads may release us from the limitation of the annealing temperature. The degradation of the soft magnetic shield layer by a high annealing temperature is considered to be able to overcome by improving the materials for the shields. For example, FeTaC nanocrystalline soft magnetic material which is used as a soft underlayer for perpendicular recording media shows a good soft magnetic property and a high saturation magnetization by annealing at 500 °C. Thus, it is thought that the trilayer read head is a promising candidate for the next generation read head. Despite the encouraging simulation results of the trilayer read head by Zhou, the feasibility of the trilayer read head has not been demonstrated. In this thesis, an antiferromagnetic interlayer exchange coupling between $Co_2Fe(Al_{0.5}Si_{0.5})$ Heusler alloy layers through Ag spacer layer was observed. The stable antiferromagnetic coupling against annealing up to 500 °C may provide promising properties with a high CPP-GMR output, which may contribute to the realization of the trilayer read head.

References

[1] M. Takagishi, K. Koi, M. Yoshikawa, T. Funayama, H. Iwasaki, M. Sahashi, IEEE Trans. Magn. **38**, 2277 (2002).

[2] Ohtsuka et al., US Patent 5859753, Mao et al. US Patent 7016160

[3] F. J. Jedema, A. T. Filip, and B. J. van Wees, Nature, **410**, 345 (2001). F. J. Jedema, H. B. Heersche, A. T. Filip, J. J. A. Baselmans, and B. J. van Wees, Nature **416** 713 (2002).

[4] R. Lamberton et al., IEEE Trans. Magn. **43**, 645 (2007).

[5] Y. Zhou, J. Appl. Phys. **105**, 07B708 (2009).

[6] A. Perumal,. Y. K. Takahashi, and K. Hono, J. Appl. Phys. **105**, 07A304 (2009).

Publications

Papers and presentations related to this thesis

1) T. M. Nakatani, T. Furubayashi, S. Kasai, H. Sukegawa, Y. K. Takahashi, S. Mitani, and K. Hono,
"Bulk and interfacial scatterings in current-perpendicular-to-plane giant magnetoresistance with $Co_2Fe(Al_{0.5}Si_{0.5})$ Heusler alloy layers and Ag spacer",
Appl. Phys. Lett. **96**, 212501 (2010).

2) T. M. Nakatani, T. Furubayashi, and K. Hono,
"Interfacial resistance and spin-dependent scattering in the current-perpendicular-to-plane giant magnetoresistance using $Co_2Fe(Al_{0.5}Si_{0.5})$ Heusler alloy and Ag",
J. Appl. Phys. (2011) in press.

3) T. M. Nakatani, T. Furubayashi, S. Kasai, Y. K. Takahashi, S. Mitani, and K. Hono,
"Current-perpendicular-to-plane giant magnetoresistance in all-B2-trilayer spin-valves using $Co_2Fe(Al_{0.5}Si_{0.5})$ Heusler alloy and NiAl intermetallic compound",
J. Magn. Magn. Mater. (2010) submitted.

4) T. Taniguchi, H. Imamura, T. M. Nakatani, and K. Hono,
"Effect of the number of layers on determination of spin asymmetries in current-perpendicular-to-plane giant magnetoresistance",
Appl. Phys. Lett. **98**, 042503 (2011).

A) T. M. Nakatani, T. Furubayashi, S. Kasai, H. Sukegawa, Y. K. Takahashi, S. Mitani, and K. Hono,
"CPP spin-valves with all B2 $Co_2FeAl_{0.6}Si_{0.4}$/NiAl/$Co_2FeAl_{0.6}Si_{0.4}$ trilayer",
CC-08 (oral), 11th Joint MMM–Intermag Conference, Jan. 20, 2010, Washington DC, USA.

B) T. M. Nakatani, T. Furubayashi, S. Kasai, H. Sukegawa, Y. K. Takahashi, S. Mitani, and K. Hono,
"Bulk scattering contribution to CPP-GMR of $Co_2FeAl_{0.5}Si_{0.5}$/Ag/$Co_2FeAl_{0.5}Si_{0.5}$ trilayer",
QC-06 (poster), The 2nd International Symposium on Advanced Magnetic Materials and Applications (ISAMMA), July 13, 2010, Sendai, Japan.

C) T. M. Nakatani, T. Furubayashi, and K. Hono,
"Large interfacial scattering in CPP-GMR devices with $Co_2Fe(Al_{0.5}Si_{0.5})$ and Ag",
DF-02 (oral), 55th Annual Conference on Magnetism and Magnetic Materials (MMM), Nov. 16, 2010, Atlanta, GA, USA.

Other coauthored papers on CPP-GMR

5) K. Kodama, T. Furubayashi, H. Sukegawa, T. M. Nakatani, K. Inomata, and K. Hono,
"Current-perpendicular-to-plane giant magnetoresistance of a spin valve using Co_2MnSi Heusler alloy electrodes",
J. Appl. Phys. **105**, 07E905 (2009).

6) T. Furubayashi, K. Kodama, T. M. Nakatani, H. Sukegawa, Y. K. Takahashi, K. Inomata, and K. Hono,
"Structure and transport properties of current-perpendicular-to-plane spin valves using $Co_2FeAl_{0.5}Si_{0.5}$ and Co_2MnSi Heusler alloy electrodes",
J. Appl. Phys. **107**, 113917 (2010).

7) N. Hase, B. S. D. Ch. S. Varaprasad, T. M. Nakatani, H. Sukegawa, S. Kasai, Y. K. Takahashi, T. Furubayashi, and K. Hono,
"Current-perpendicular-to-plane spin valves with a $Co_2Mn(Ga_{0.5}Sn_{0.5})$ Heusler alloy",
J. Appl. Phys. **108**, 093916 (2010).

8) N.Hase, T. M. Nakatani, S. Kasai, Y. K. Takahashi and K. Hono,
"Enhancement of the current-perpendicular-to-plane giant magnetoresistance by insertion of $Co_{50}Fe_{50}$ layers at $Co_2MnGa_{0.5}Sn_{0.5}$/Ag interface",
J. Appl. Phys. (2011) in press.

9) H. S. Goripati, T. Furubayashi, S. V. Karthik, T. M. Nakatani, Y. K. Takahashi , and K. Hono,
"The effect of substitution of Fe with Cr on the giant magnetoresistance of current perpendicular-to-plane spin valves with Co_2FeSi Heusler alloy",
J. Appl. Phys. (2011) accepted.

謝辞

本研究は独立行政法人　物質・材料研究機構　磁性材料センターにて行われました．指導教官である，物質・材料研究機構フェロー，筑波大学大学院数理物質科学研究科教授　宝野和博先生に心から感謝いたします．先生の，さまざまな社会情勢および社会的要請に対して公的研究機関はどう取り組むべきかという，大きな視野からの研究姿勢に日々感銘を受けました．素晴らしい研究環境を与えてくださり，5 年間の大学院生活を楽しむことができました．

本論文をまとめるにあたり，筑波大学数理物質科学研究科　喜多英治教授，三谷誠司教授（物質・材料研究機構　磁性材料センター　スピントロニクスグループリーダー），および産業技術総合研究所　ナノシステム研究部門　ナノ理論グループ長　今村裕志博士には審査委員として，多くのご助言をいただきました．心より感謝いたします．また，三谷教授には常日頃より，今村博士には共同研究者として有益なご議論を賜りました．

磁性材料センター磁性材料グループの古林孝夫博士には，本研究を始めるにあたって，各実験手法のご指導を賜りました．また，実験結果に関して日常的に議論していただき，物理への理解が深まりました．深く感謝いたします．

磁性材料センター磁性材料グループの高橋有紀子博士には，スパッタ装置の導入及び立ち上げに関し全面的にご協力いただきました．その他の実験の様々な面において便宜を図っていただきました．心より感謝いたします．

磁性材料センタースピントロニクスグループの葛西伸哉博士には微細加工および伝導測定において全面的にご指導・ご協力いただきました．林将光博士にはシミュレーションのデータをご提供いただいたほか，実験計画や将来展望について相談にのっていただきました．介川裕章博士には微細加工および薄膜作製について数多くのご助言をいただきました．また 3 博士には，日頃より気さくなご議論をいただき，しばしば頼れる兄貴として相談にのっていただきました．心より感謝いたします．

磁性材料センターナノ組織解析グループの大久保忠勝博士には，TEM や SEM をはじめ，様々な実験設備の使用，および研究室での日常生活にあたって便宜を図っていただきました．深く感謝いたします．

博士論文テーマの選択にあたってご相談いただき，有益なご議論をいただいた物質・材料研究機構名誉フェローの猪俣浩一郎先生に，心より謝意を表します．

応用の観点から様々なご教授・ご意見を頂いた，(株)東芝　研究開発センターの岩崎仁志氏，高岸雅幸博士，鴻井克彦博士，山田健一郎氏に深く感謝いたします.

薄膜作製装置の導入および維持に関し，迅速かつきめ細かい対応をして下さった，株式会社エイコーエンジニアリングの技術者の皆様に感謝いたします.

スピン依存伝導の理論について有益なご議論・ご教授をいただきました，筑波大学数理物質科学研究科および産業技術総合研究所の谷口知大氏に感謝いたします.

ともに CPP-GMR の研究を行い，常にサポートしていただいた長谷直基君，Pattabiraman Sudharchan 君，小玉恒太君に感謝いたします．また，修士課程の頃から，研究面や生活面で大変お世話になった，研究室の先輩である Ammanabrolu Rajinikanth 博士と Sankar Vijay Karthik 博士に感謝いたします．その他，研究室のメンバーの皆様に感謝いたします.

スペーサー材料選択に関し，Tuscaloosa および Pittsburgh にて有益な議論していただいた，University of Alabama の Professor Oleg Mryasov および元 Seagate Research の Dr. Thomas Ambrose に心より感謝いたします.

気さくにご議論をいただいた Hitachi Global Storage Technologies の Dr. Jeffrey Childress に感謝いたします.

大学入学から博士後期課程修了までの 9 年間，様々な面でお世話になりました，大阪府立大学工学部および筑波大学数理物質科学研究科の先生方に心から感謝いたします.

物質・材料研究機構からは 4 年間 NIMS ジュニア研究員として採用していただき，素晴らしい研究環境を与えていただきました．また，本研究は平成 22 年度より，学術振興会特別研究員 DC2 研究課題「ホイスラー合金を用いた CPP-GMR 素子に対するスペーサー層材料の選択とその効果」のご支援を受けました．謝意を表します.

最後に，大学院に進む機会を与えてくれた両親，いつも応援してくれた姉と妹，そして友人に深く感謝いたします.

平成 23 年 2 月　中谷　友也